Measurement of angular distribution of γ rays from neutron-induced compound states of 118Sn with a pulsed neutron beam

古賀, 淳

出版情報：九州大学, 2020, 博士（理学）, 課程博士
バージョン：
権利関係：公表確認書・全文ファイル未提出

Doctoral Dissertation

Measurement of angular distribution of γ rays from neutron-induced compound states of ^{118}Sn with a pulsed neutron beam

Jun Koga

Department of Physics
Graduate School of Science
KYUSHU UNIVERSITY

Supervisor: Tamaki Yoshioka

Februrary 2021

Abstract

The violation of charged conjugate and parity transformation symmetry (CP-violation) beyond the Standard Model is considered to be essential to explain the asymmetry between matter and antimatter in the current universe. Under the CPT theorem, CP-violation is equal to the violation of time-reversal symmetry (T-violation). Therefore, a number of experiments have been conducted to search for T-violation, and the current strongest limit has been obtained by searching for neutron electric dipole moment (nEDM).

Neutron-induced compound nuclei are expected to be sensitive to T-violation, and it is theoretically predicted that the sensitivity is proportional to a factor $\kappa(J)$ which depends on the mixing angle ϕ of the 1/2 and 3/2 components of the total angular momentum of the neutron in a p-wave resonance. However, the ϕ has not yet been measured for most nuclei. It is predicted that the p-wave resonance shape depends on both the ϕ and the γ-ray emission angle (θ_γ) with respect to the direction of the incident neutron. The ϕ can be determined by measuring the angular dependence of the p-wave resonance shape.

This dissertation reports a measurement result of the angular dependence and an analysis result determining the ϕ and the $\kappa(J)$ for ^{117}Sn. The experiment was performed using a pulsed neutron beam and a germanium detector assembly at Japan Proton Accelerator Research Complex (J-PARC) with the time-of-flight method. The angular dependence of the 1.33 eV p-wave resonance was observed in the direct transition from the compound state of ^{118}Sn to the ground state. The asymmetry value A_{LH} was defined to evaluate the angular dependence as $A_{\mathrm{LH}} = (N_{\mathrm{L}} - N_{\mathrm{H}})/(N_{\mathrm{L}} + N_{\mathrm{H}})$, where $N_{\mathrm{L(H)}}$ is the integrated values in the lower (higher) energy region of the resonance. The result was obtained to be $A_{\mathrm{LH}} = (0.473 \pm 0.057)\cos\theta_\gamma + (0.091 \pm 0.019)$. Two results obtained by the analysis based on the theoretical formalism are

$$\phi = (10.3^{+6.4}_{-7.2})^\circ \quad \text{and} \quad |\kappa(J)| = 0.42^{+0.05}_{-0.06}$$

or

$$\phi = (-80.8^{+7.1}_{-6.4})^\circ \quad \text{and} \quad |\kappa(J)| = 2.6^{+6.8}_{-1.3}.$$

T-violation in the compound nuclear reaction will be searched by irradiating a polarized neutron beam into a polarized target and measuring a T-odd term in the neutron forward scattering amplitude. Assuming that the polarization of the neutron beam and ^{117}Sn target with a thickness of 5 cm is 85% and 20%, the measurement time to improve the current upper limit for T-violation by the nEDM search was estimated to be approximately 10 days in the case of $\phi = -80.8^\circ$.

Acknowledgments

First of all, I would like to sincerely thank my supervisor, Professor Tamaki Yoshioka. He always gave great advice and comments for this study. Without his guidance and persistent help, this dissertation would not have been possible. Moreover, his attitude as a scientist deeply influenced my life. It was one of the greatest fortunes in my life to spend my master's and doctoral programs as his student.

I also wish to express my gratitude to Professor Kiyotomo Kawagoe. He keeps encouraging and guiding me since the time of my undergraduate school. I think that I was able to grow by being given the opportunities to go overseas for the experiment and the international school. If he had not established his laboratory, I could not have started this study.

I would like to thank all the collaborators of the NOPTREX experiment and Neutron Optics and Physics. I am deeply grateful to Professor Hirohiko M. Shimizu, Professor Masaaki Kitaguchi, and Professor Katsuya Hirota. Their technical advice and comments on the experiment and analysis helped me extensively. I would like to express my appreciation to Dr. Takuya Okudaira, Dr. Tomoki Yamamoto, and Mr. Shusuke Takada. I really enjoyed the experiments in J-PARC and discussion with them. Especially, Mr. Shusuke Takada supported me from the beginning of this study, and we had a great deal of discussions on physics and we spent a lot of time together in and out the laboratory. I would like to offer my special thanks to Dr. Kenji Mishima. He supported me extensively and gave great advice on neutron experiments. Without his help, I would not have been able to publish my study on the neutron life measurement.

I owe a very important debt to the staffs of the MLF at J-PARC for providing the neutron beam and the experimental instruments. I am particularly grateful for the assistance given by Dr. Atsushi Kimura and Dr. Shoji Nakamura. They maintained the instruments at BL04, and their technical advice to analyze the measured data was crucial for my research.

Not just the collaborators, I would also like to thank the staffs of the laboratory, including Professor Junji Tojo, Dr. Hidetoshi Otono, Dr. Susumu Oda, Dr. Taikan Suehara, Dr. Dai Kobayashi, and Ms. Saori Shigematsu. I would also like to thank all those whose names I have not mentioned but who supported my study and tenure.

Last but not the least, I am deeply grateful to my family, who allowed me to study and provided financial support throughout my life.

Contents

List of Figures

List of Tables

Chapter 1

Introduction

1.1 Overview of this dissertation

It is theoretically predicted that neutron-induced compound states would be highly sensitive to the violation of time-reversal symmetry (T-violation) due to an enhancement mechanism. The sensitivity to T-violation depends on a parameter ϕ. In order to determine the ϕ value precisely, the measurement was performed at Japan Proton Accelerator Research Complex (J-PARC). This dissertation describes that the determination of the ϕ value and the possibility of a T-violation search experiment using the compound nuclear reaction of ^{117}Sn.

In Chapter 1, the history of discrete symmetry violation and the current status of the T-violation search are described. Chapter 2 describes a theoretical prediction of the enhancement mechanism for T-violation in compound nuclear reactions. The ϕ value can be determined by measuring the angular distribution of γ rays emitted from the neutron-induced compound states. In Chapter 3, the theoretical formalism of the angular distribution and the differences between a previous study and this study are described. Chapter 4 describes the experimental setup, characteristics of a neutron beam and detectors, and a data acquisition system. Measurement data and targets used in the measurements are described in Chapter 5. An analysis method is explained in Chapter 6 and the ϕ value is determined. Chapter 7 compares this study with the previous study and discusses the experimental sensitivity of T-violation and future prospects. Chapter 8 concludes this dissertation.

1.2 Discrete symmetry violation

Before the 1950s, physical law was considered invariant to a particular direction or location. The invariance of physical systems with respect to transformation leads to a conservation law, which is known as Noether's theorem. For example, invariances with respect to spatial translation and rotation give the conservation laws of linear momentum and angular momentum, respectively. In this case, linear momentum p and angular momentum L satisfy $[p, H] = 0$ and $[L, H] = 0$, where H is a Hamiltonian in the system. This idea can be applied to discrete transfor-

mations: parity (P) and time-reversal (T) transformations. Parity transformation indicates the flip in the sign of a spatial coordinate. Time-reversal transformation is the reversal of the direction of time. Invariance of the physics law to parity and time-reversal transformation also requires $[P, H] = 0$ and $[T, H] = 0$. In addition, charge conjugation (C) transformation is defined in particle physics as the change of a particle into its antiparticle. These discrete transformations were believed to have symmetries to the physical law.

In 1956, T. D. Lee and C. N. Yang proposed a possibility of P-violation in the weak interaction as a solution of the θ-τ puzzle [1]. In 1957 [2], C. S. Wu *et al.* experimented to verify this postulate by measuring the angular distribution of electrons from polarized ^{60}Co via β decay. This experiment established that electrons are likely to emit in the direction opposite to the spin of ^{60}Co. This asymmetric distribution to the spin direction is direct evidence of P-violation.

In 1964, CP-violation in the weak interaction was observed in the decay process of neutral kaon by J. H. Christenson *et al.* [3]. The two types of kaon K_1 and K_2 have different charge-conjugation and parity (CP) eigenstates. K_1 decays to two pions ($\pi^0\pi^0$ and $\pi^+\pi^-$) and K_2 decays to three pions ($\pi^0\pi^0\pi^0$ and $\pi^0\pi^+\pi^-$). Two more types of kaon K_L and K_S were also observed. They have different lifetimes: $\tau_\mathrm{L} = 5.2 \times 10^{-8}$ s and $\tau_\mathrm{S} = 8.9 \times 10^{-11}$ s. K_L and K_S were believed to be exactly K_2 and K_1, respectively. However, J. H. Christenson *et al.* discovered that K_L decays to two pions with a branching ratio of 2.2×10^{-3}. This means that K_L and K_S are the mixtures of two different CP eigenstates.

In addition, CP-violation was also observed in the decay process of B meson at Belle experiment [4] and BaBar experiment [5]. These experiments are known as the B-factories because the electrons collide with the positrons at the center-of-mass energy equal to the mass of $\Upsilon(4\mathrm{S})$ which decays to $B\bar{B}$ pairs. In the Belle experiment, B and $\bar{B}$ mesons can fly longer than the value of $c\tau$, where c is the speed of light and τ is the average lifetime of the B meson. This is because their lifetimes in the observer's rest frame are increased by the Lorentz boost factor, which is caused by the asymmetric energy collision. The difference in decay rates between B and $\bar{B}$ mesons was observed by measuring the difference of the average flight lengths between them.

1.3 CP-violation in the Standard Model

The observed CP-violation can be explained by the Standard Model (SM) of particle physics. In the SM, there are two possible sources of CP-violation. One is the complex phase of the Cabibbo-Kobayashi-Maskawa (CKM) matrix [6]. The charged current by the W boson exchange is described as

$$j^\mu = (\bar{u}, \bar{c}, \bar{t}) \frac{\gamma^\mu(1-\gamma^5)}{2} V_\mathrm{CKM} \begin{pmatrix} d \\ s \\ b \end{pmatrix}, \tag{1.1}$$

where γ^μ is the gamma matrix, $\gamma^5 = i\gamma^0\gamma^1\gamma^2\gamma^3$. V_CKM is a 3×3 unitary matrix which can be parameterized by three mixing angles and the CP-violating complex

phase and given as

$$
\begin{aligned}
V_{\rm CKM} &= \begin{pmatrix} V_{ud} & V_{us} & V_{ub} \\ V_{cd} & V_{cs} & V_{cb} \\ V_{td} & V_{ts} & V_{tb} \end{pmatrix} \\
&= \begin{pmatrix} 1 & 0 & 0 \\ 0 & c_{23} & s_{23} \\ 0 & -s_{23} & c_{23} \end{pmatrix} \begin{pmatrix} c_{13} & 0 & s_{13}e^{-i\delta} \\ 0 & 1 & 0 \\ s_{13}e^{i\delta} & 0 & c_{13} \end{pmatrix} \begin{pmatrix} c_{12} & s_{12} & 0 \\ -s_{12} & c_{12} & 0 \\ 0 & 0 & 1 \end{pmatrix} \\
&= \begin{pmatrix} c_{12}c_{13} & s_{12}c_{13} & s_{13}e^{-i\delta} \\ -s_{12}c_{23} - c_{12}c_{23}e^{i\delta} & -c_{12}c_{23} - s_{12}s_{23}s_{13}e^{i\delta} & s_{23}c_{13} \\ s_{12}c_{23} - c_{12}c_{23}s_{13}e^{i\delta} & -c_{12}c_{23} - s_{12}c_{23}s_{13}e^{i\delta} & c_{23}c_{13} \end{pmatrix}, \quad (1.2)
\end{aligned}
$$

where $s_{ij} = \sin\theta_{ij}$, $c_{ij} = \cos\theta_{ij}$, and δ is the phase responsible for CP-violating phenomena in flavor-changing processes in the SM. The values of these parameters are $s_{12} = 0.22650 \pm 0.00048$, $s_{13} = 0.00361^{+0.00011}_{-0.00009}$, $s_{23} = 0.04053^{+0.00083}_{-0.00061}$, and $\delta = 1.196^{+0.045}_{-0.043}$, respectively [7].

The other CP-violating source is the θ term in the Quantum Chromodynamics (QCD) which describes the strong interaction of colored quarks and gluons. The Lagrangian of QCD is given by

$$
\begin{aligned}
\mathcal{L}_{\rm QCD} &= \sum_q \bar{\psi}_{q,a}(i\gamma^\mu\partial_\mu\delta_{ab} - g_s\gamma^\mu t^C_{ab}\mathcal{A}^C_\mu - m_q\delta_{ab})\psi_{q,b} \\
&- \frac{1}{4}F^A_{\mu\nu}F^{A\mu\nu} + \frac{g_s^2\theta}{32\pi^2}F^A_{\mu\nu}\tilde{F}^{A\mu\nu}, \quad (1.3)
\end{aligned}
$$

where the $\psi_{q,a}$ are quark-field spinors for a quark flavor q with its mass m_q, and an index a runs from $a = 1$ to $N_c = 3$ which indicates the three colors. The $\mathcal{A}^C_\mu$ is the gluon field and an index C runs from 1 to $N_c^2 - 1 = 8$ which indicates eight types of gluons. The t^C_{ab} corresponds to eight 3×3 matrices which are defined as Gell-Mann matrices. The field tensor $F^A_{\mu\nu}$ is given by

$$
\begin{aligned}
F^A_{\mu\nu} &= \partial_\mu\mathcal{A}^A_\nu - \partial_\nu\mathcal{A}^A_\mu - g_s f_{ABC}\mathcal{A}^B_\mu\mathcal{A}^C_\mu \quad (1.4) \\
\left[t^A, t^B\right] &= if_{ABC}t^C \quad (1.5) \\
\tilde{F}^{A\mu\nu} &= \frac{1}{2}\epsilon_{\mu\nu\sigma\rho}F^{A\sigma\rho}, \quad (1.6)
\end{aligned}
$$

where the f_{ABC} are the structure constants of the SU(3) group and $\epsilon_{\mu\nu\sigma\rho}$ is the antisymmetric Levi-Civita symbol. The 3rd term of Eq. (1.3) corresponds to the CP-violating term in the QCD Lagrangian. However, the value of θ is limited to $|\theta| \lesssim 10^{-10}$ by experimental results. This indicates that CP-violation in the strong interaction is very small, and this is called the strong CP problem.

1.4 Asymmetry between matter and antimatter

In the early stages of the universe with a high-density and high-energy state, it was believed that particles and antiparticles maintained an equilibrium state by

repeating pair productions and annihilations, and the number of particles was the same as that of antiparticles. However, the matter-antimatter asymmetry indicates an imbalance between baryonic and antibaryonic matter in the currently observed universe. The asymmetry between baryons and antibaryons is evaluated using the parameter η as

$$\eta \equiv \frac{n_B - n_{\bar{B}}}{n_B + n_{\bar{B}}} = \frac{n_B - n_{\bar{B}}}{n_\gamma} \sim 10^{-9}, \tag{1.7}$$

where n_B and $n_{\bar{B}}$ are number densities of baryons and antibaryons, respectively. The n_γ is the number density of photons. On the other hand, the theoretical estimation from the SM is done as follows [8];

$$\frac{n_B - n_{\bar{B}}}{n_B + n_{\bar{B}}} \sim 10^{-18}. \tag{1.8}$$

This large discrepancy is one of the most important problems in particle physics and cosmology and implies that the SM cannot explain the current matter-dominant universe. In 1967, A. Sakharov proposed three conditions which are critical for the explanation of the matter-dominant universe. The three "Sakharov conditions" are [9]:

- Baryon number violation.
- C- and CP-violation.
- Interaction outside thermal equilibrium.

The 2nd condition suggests that there is a possibility of unknown CP-violation sources beyond the SM. This implies the existence of unknown T-violation sources under the CPT theorem [10, 11].

1.5 CP-violation in low-energy scale

Multiple experimental searches for T-violation have been conducted in the world. Figure 1.1 shows the hierarchy of scales between the CP-odd sources and three generic classes of observable electric dipole moments (EDMs). The fundamental CP-odd phase appears several EDMs through different paths in low-energy scale. This idea is based on the effective field theory (EFT).

The reason why a non-zero value of the EDM indicates the existence of T-violation is explained as follows. The Hamiltonian of interactions between a particle and an electromagnetic field can be written using a magnetic moment $\boldsymbol{\mu}$ and an EDM $\boldsymbol{d}$ as

$$H = -\boldsymbol{\mu} \cdot \boldsymbol{B} - \boldsymbol{d} \cdot \boldsymbol{E}, \tag{1.9}$$

where $\boldsymbol{B}$ and $\boldsymbol{E}$ are a magnetic field and an electric field, respectively. Under the T transformation, $\boldsymbol{B}$, $\boldsymbol{E}$, $\boldsymbol{\mu}$, and $\boldsymbol{d}$ are transformed as

$$\boldsymbol{B} \to -\boldsymbol{B}, \boldsymbol{E} \to \boldsymbol{E}, \boldsymbol{\mu} \to -\boldsymbol{\mu}, \boldsymbol{d} \to -\boldsymbol{d}. \tag{1.10}$$

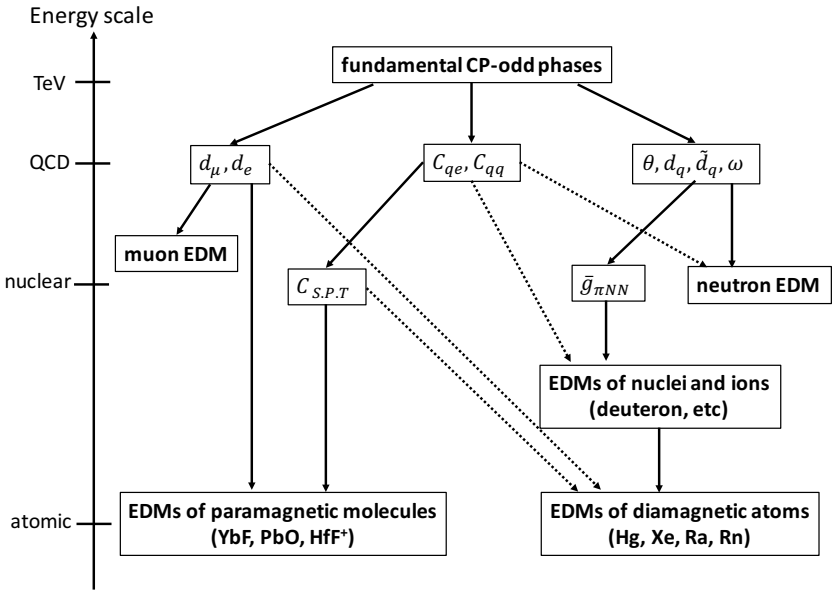

Figure 1.1: Schematic plot of the hierarchy of scales between the CP-odd sources and three generic classes of observable EDMs. The dashed lines indicate generically weaker dependencies [12].

Therefore, the Hamiltonian is transformed in the T-transformed coordinate as

$$H = -\boldsymbol{\mu} \cdot \boldsymbol{B} + \boldsymbol{d} \cdot \boldsymbol{E}. \tag{1.11}$$

If the value of d is non-zero, the Hamiltonian H will change by the T transformation. This means that a non-zero EDM value of the particle implies the existence of T-violation.

The neutron EDM (nEDM) has been studied for a long time. Because it is a simpler system than massive atoms, it is relatively easy to compare the experimental results with the theoretical calculations. In addition, nEDM search is expected to be sensitive to supersymmetric baryogenesis in the minimal supersymmetric standard model (MSSM). As an example, the nEDM search for $\mathcal{O}(10^{-27})$ $e \cdot \mathrm{cm}$ can exclude MSSM more effectively than collider experiments as shown in Fig. 1.2. However, it is hard to obtain sufficient statistics due to the short lifetime of neutrons and the difficulty in generating neutrons. Figure 1.3 shows a historical plot of the upper limit of nEDM. The current upper limit was obtained by the experiment conducted at Paul Scherrer Institute (PSI) as

$$|d_\mathrm{n}| < 1.8 \times 10^{-26}\ e \cdot \mathrm{cm}\ (90\%\ \mathrm{C.L.}). \tag{1.12}$$

The error of this experimental result is largely due to statistical errors. The development of technology to increase the number of neutrons is essential to further improve accuracy.

One of the different methods to search for T-violation employs a neutron-induced compound state. The compound nucleus model was introduced by N. Bohr

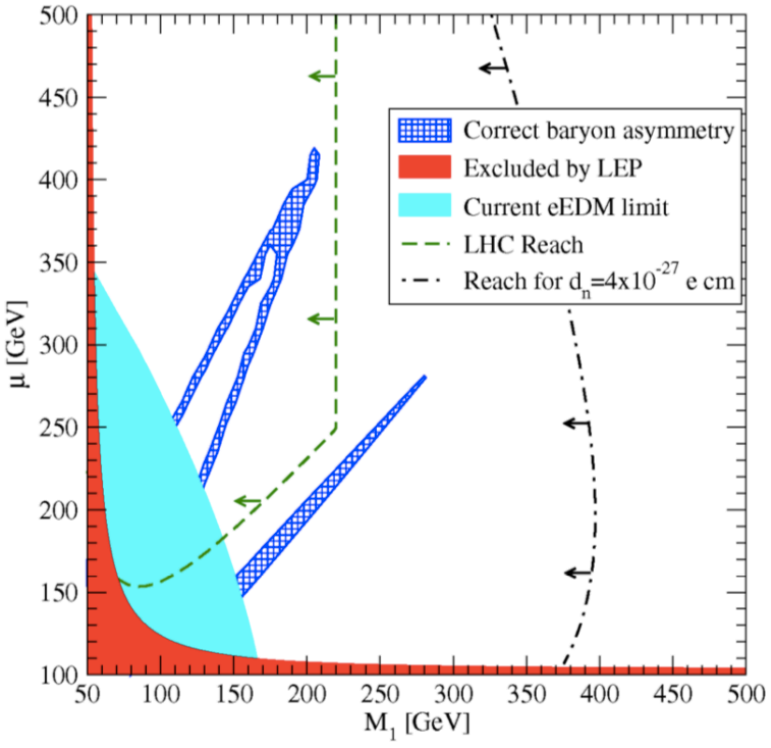

Figure 1.2: Sensitivity of EDMs and LHC to supersymmetric baryogenesis in the minimal supersymmetric standard model [13]. The horizontal axis is the gaugino mass M_1 and the vertical axis is the supersymmetric mass μ. The red region was excluded by the Large Electron-Positron Collider (LEP) experiment. The limit of electron EDM excludes the cyan region. The blue bands lead to the observed baryon asymmetry η. Large Hadron Collider (LHC) and nEDM searches will probe the region to the left of the green-dashed lines and the black-dashed lines, respectively.

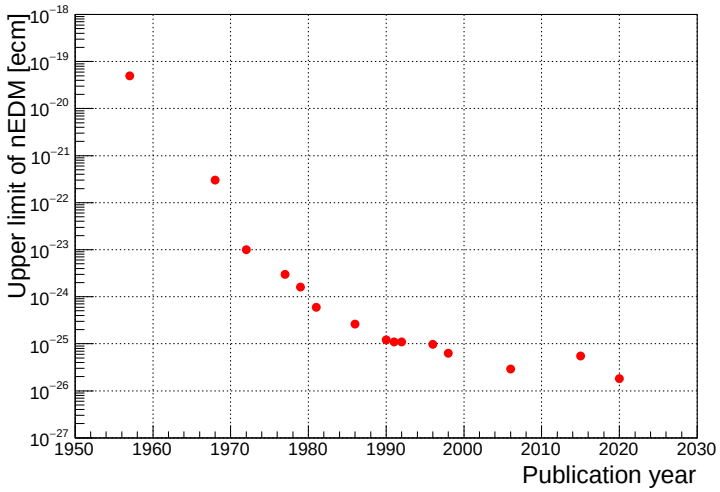

Figure 1.3: History of the upper limit of nEDM [14–28].

in 1936 [29]. When a neutron irradiates into a target nucleus, the energy of the incident neutrons is distributed to each nucleon in the nucleus, and the nucleons repeatedly collide with each other. The energy exchanged between the nucleons is small, and it takes time of approximately 10^{-16} seconds for the excess energy to be released. This time is much longer than that of approximately 10^{-22} seconds that a neutron with the energy of a few MeV takes to pass through a nucleus without interactions. Such long-excited states can be treated as a type of nucleus with a lifetime, which allows defining internal degrees of freedom such as spin.

The compound nuclear reaction is sensitive to the coupling constant of pion exchange interaction between nucleons. Therefore, experimental searches using the compound nuclear reaction are sensitive to the T-violating coupling constant $\bar{g}_{\pi NN}$ shown in Fig. 1.1. The T-violating cross section in the compound nuclear reaction ($\Delta\sigma_{\mathrm{T}}$) is theoretically estimated as follows [30];

$$\frac{\Delta\sigma_{\mathrm{T}}}{2\sigma_{\mathrm{tot}}} = \frac{-0.185\ \mathrm{b}}{2\sigma_{\mathrm{tot}}} \times \left(\bar{g}_{\pi}^{(0)} + 0.26\bar{g}_{\pi}^{(1)}\right). \tag{1.13}$$

Here, $\bar{g}_{\pi}^{(0)}$ and $\bar{g}_{\pi}^{(1)}$ are isoscalar coupling constant and isovector coupling constant with T-violation, respectively. The variable σ_{tot} indicates the total cross section in the compound nuclear reaction. On the other hand, the value of nEDM is estimated using T-violating isotensor coupling constant $\bar{g}_{\pi}^{(2)}$ as [31]

$$d_{\mathrm{n}} \simeq 0.14\left(\bar{g}_{\pi}^{(0)} - \bar{g}_{\pi}^{(2)}\right). \tag{1.14}$$

This implies that the T-violation search using compound nuclear reactions can complementarily explore the parameter space of coupling constants using a different method than nEDM as shown in Fig. 1.4.

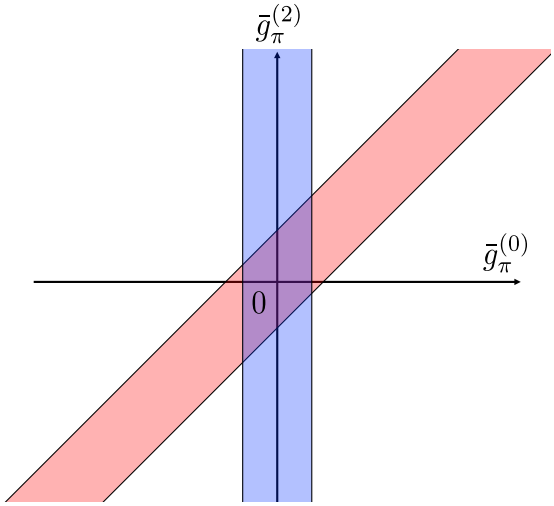

Figure 1.4: Relationship between nEDM and compound state in $\bar{g}_{\pi}^{(0)}$-$\bar{g}_{\pi}^{(2)}$ plane. The red and blue bands are based on the limits obtained from experiments on nEDM and using the compound state, respectively

Chapter 2

Discrete symmetry violation in a compound nucleus

In this chapter, enhancement mechanisms of P-violation and T-violation in the compound nuclear reactions are explained. Moreover, an experimental approach to T-violating interaction is introduced.

2.1 Parity violation

2.1.1 P-violation in proton-proton scattering

The strong interaction is a dominant process in the nucleon-nucleon interactions. The parity non-conserving (PNC) effect which is caused by the weak interaction is very small. The relative magnitude of the weak interaction to the strong interaction on the MeV scale is approximately estimated to be $\alpha_{\rm w}/\alpha_{\rm s} \sim 10^{-7}$, where $\alpha_{\rm w}$ and $\alpha_{\rm s}$ are the strength parameters for the weak and the strong interactions, respectively. Proton-proton scattering is a fundamental process in nucleon-nucleon interactions. The PNC effect in the proton-proton scattering has been observed by measuring the helicity dependence of the total cross section using a polarized proton beam and an unpolarized proton target. The magnitude of the PNC effect is described as the longitudinal asymmetry $A_{\rm L,pp}$ as

$$A_{\rm L,pp} = \frac{\sigma^{+}_{\rm pp} - \sigma^{-}_{\rm pp}}{\sigma^{+}_{\rm pp} + \sigma^{-}_{\rm pp}}, \tag{2.1}$$

where $\sigma^{+}_{\rm pp}$ and $\sigma^{-}_{\rm pp}$ are the total cross sections for positive- and negative-helicity protons on the target, respectively. The value of the longitudinal asymmetry $A_{\rm L,pp}$ is the ratio of the PNC component to the parity-conserving (PC) component. It has been measured at several incident proton energies and the results are summarized in Table 2.1.

This P-violating effect is theoretically explained as follows. The total amplitude f consists of PC part ($f_{\rm PC}$) and PNC part ($f_{\rm PNC}$) as

$$f = f_{\rm PC} + f_{\rm PNC}. \tag{2.2}$$

Table 2.1: Previous results of P-violation in p-p scattering.

Proton energy [MeV]	$A_{\mathrm{L,pp}}$	Reference
15	$-(1.7 \pm 0.8) \times 10^{-7}$	[32]
45	$-(2.3 \pm 0.89) \times 10^{-7}$	[33]
45	$-(1.3 \pm 2.3) \times 10^{-7}$	[34]
221	$(0.84 \pm 0.29 \pm 0.17) \times 10^{-7}$	[35]
800	$(2.4 \pm 1.1 \pm 0.1) \times 10^{-7}$	[36]
2×10^5	$(5 \pm 17 \pm 20) \times 10^{-6}$	[37]

The absolute square of f is to be observed in an experiment as

$$\begin{aligned} |f|^2 &= |f_{\mathrm{PC}} + f_{\mathrm{PNC}}|^2 \\ &= |f_{\mathrm{PC}}|^2 \left(1 + \frac{f_{\mathrm{PC}} f^*_{\mathrm{PNC}} + f^*_{\mathrm{PC}} f_{\mathrm{PNC}}}{|f_{\mathrm{PC}}|^2} + \frac{|f_{\mathrm{PNC}}|^2}{|f_{\mathrm{PC}}|^2}\right). \end{aligned} \tag{2.3}$$

The longitudinal asymmetry $A_{\mathrm{L,pp}}$ corresponds to the second term in Eq. (2.3) and the size of f_{PNC} to that of f_{PC} is roughly given by the ratio of PC and PNC light-meson-exchange potentials (V_{PC} and V_{PNC}):

$$\begin{aligned} A_{\mathrm{L,pp}} &\approx \frac{f_{\mathrm{PC}} f^*_{\mathrm{PNC}} + f^*_{\mathrm{PC}} f_{\mathrm{PNC}}}{|f_{\mathrm{PC}}|^2} \approx \frac{|f_{\mathrm{PNC}}|}{|f_{\mathrm{PC}}|} \\ &\sim \frac{V_{\mathrm{PNC}}}{V_{\mathrm{PC}}} \sim G_{\mathrm{F}} m_\pi^2 \sim 2 \times 10^{-7}, \end{aligned} \tag{2.4}$$

where G_{F} and m_π are the Fermi coupling constant and the pion mass, respectively. This theoretical estimation is consistent with the experimental results measured on the MeV scale. However, the order of $A_{\mathrm{L,pp}}$ on the GeV scale is larger than that on the MeV scale, as α_s is smaller due to the nature of running coupling. G. Nardulli *et al.* estimated that the order of $A_{\mathrm{L,pp}}$ is $\mathcal{O}(10^{-6})$ on the GeV scale [38, 39].

2.1.2 Enhancement of P-violation in a compound nucleus

In several neutron-induced compound nuclei, P-violation has been observed by measuring the helicity dependence of the neutron-capture cross section using a polarized neutron beam and an unpolarized target. The P-violation was evaluated as a longitudinal asymmetry A_{L} as

$$A_{\mathrm{L}} = \frac{\sigma^+_{\mathrm{cap}} - \sigma^-_{\mathrm{cap}}}{\sigma^+_{\mathrm{cap}} + \sigma^-_{\mathrm{cap}}}, \tag{2.5}$$

where σ^+_{cap} and σ^-_{cap} are the neutron-capture cross sections of the target nucleus for positive- and negative-helicity neutrons, respectively. Figure 2.1 shows the experimental results of the longitudinal asymmetry A_{L} in various nuclei. These results imply that the P-violation in nucleon-nucleon interactions is enhanced by up to 10^6 times in neutron-induced compound nuclei. This large-enhanced P-violation has been observed only in p-wave resonances located at the tail of s-wave resonances as shown in Fig. 2.2.

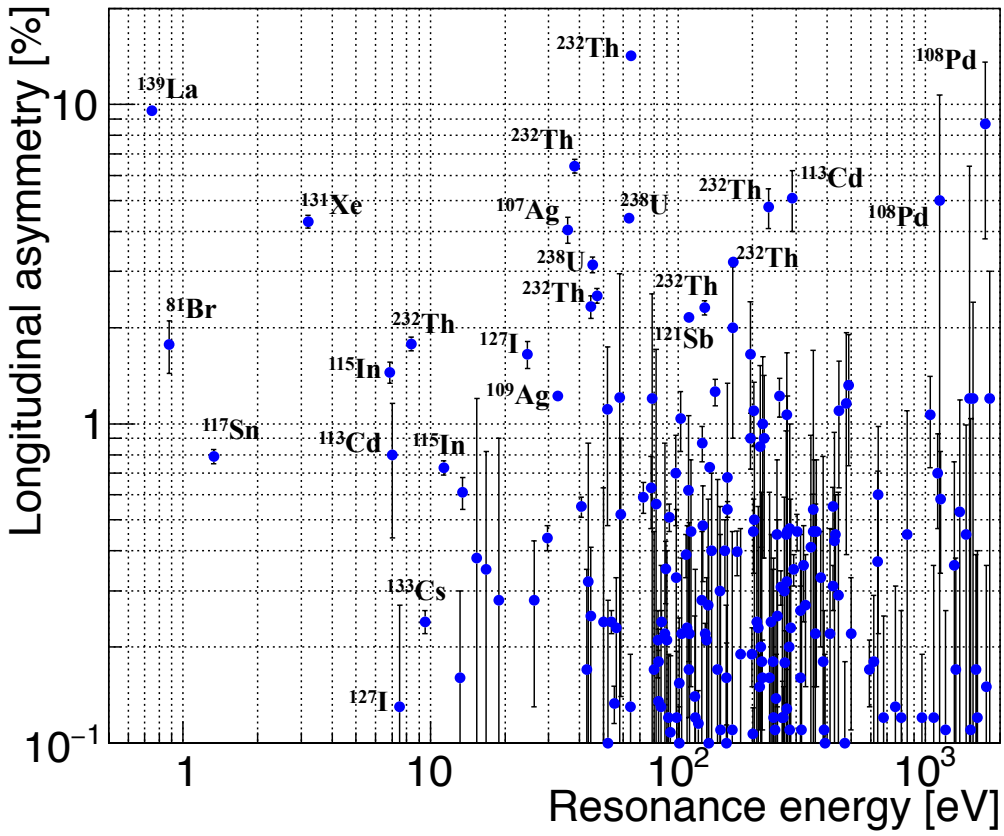

Figure 2.1: Longitudinal asymmetry in various nuclei [40].

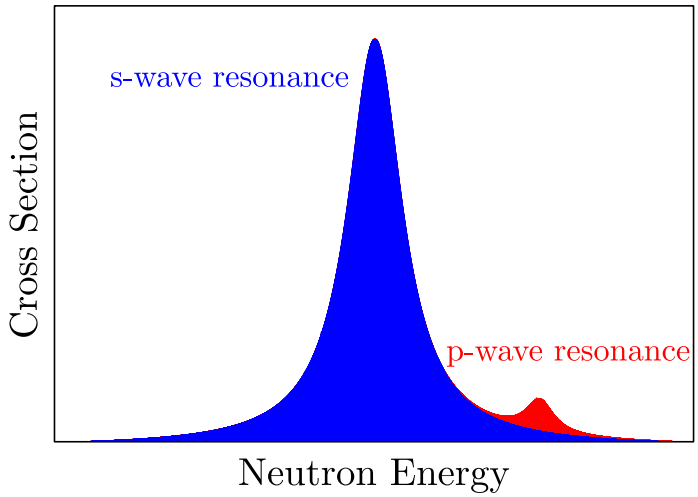

Figure 2.2: Illustration of a p-wave resonance located at the tail of an s-wave resonance. The large enhanced P-violation has been observed at such p-wave resonances.

The enhancement phenomena can be theoretically explained by interference between amplitudes of the p-wave resonance and a neighboring s-wave resonance (s-p mixing) as follows. The angular momentum of the incident neutron $\boldsymbol{j}$ is given as

$$\boldsymbol{j} = \boldsymbol{l} + \boldsymbol{s}, \tag{2.6}$$

where $\boldsymbol{l}$ is the orbital angular momentum of the incident neutrons and $\boldsymbol{s}$ is its spin. The angular momentum in a p-wave resonance is either $j = 1/2$ or $j = 3/2$, while the angular momentum in an s-wave resonance is only allowed for $j = 1/2$. The neutron width of an s-wave resonance $\Gamma^{\rm n}_{\rm s}$ and that of a p-wave resonance $\Gamma^{\rm n}_{\rm p}$ can be written as

$$\Gamma^{\rm n}_{\rm s} = \Gamma^{\rm n}_{{\rm s},j=1/2} \quad \text{and} \quad \Gamma^{\rm n}_{\rm p} = \Gamma^{\rm n}_{{\rm p},j=1/2} + \Gamma^{\rm n}_{{\rm p},j=3/2}, \tag{2.7}$$

where $\Gamma^{\rm n}_{{\rm s},j=1/2}$ is the component of $j = 1/2$ in an s-wave resonance, and $\Gamma^{\rm n}_{{\rm p},j=1/2}$ and $\Gamma^{\rm n}_{{\rm p},j=3/2}$ are the components of $j = 1/2$ and $j = 3/2$in a p-wave resonance, respectively. When the total angular momentum of the compound state $\boldsymbol{J}$ is the same in an s-wave and a p-wave resonance, the two opposite parity states of the incident neutrons, the s-wave state and $j = 1/2$ part of the p-wave state, can interfere with each other via the weak interaction. Since nucleons in the compound states have a much longer time to interfere with each other than in a direct process, the interference effect between two opposite-parity states can be much larger in the compound states in a direct process.

In the s-p mixing model, the longitudinal asymmetry $A_{\rm L}$ at the p-wave resonance can be described as

$$A_{\rm L} \simeq -\frac{2xW}{E_{\rm p} - E_{\rm s}}\sqrt{\frac{\Gamma^{\rm n}_{\rm s}}{\Gamma^{\rm n}_{\rm p}}}, \tag{2.8}$$

where $E_{\rm s}$ and $E_{\rm p}$ are the resonance energies of the s- and p-wave resonances, respectively. The individual matrix element of the weak P-violating interaction between the s- and p-wave states is denoted as W. Here, x is given as

$$x = \sqrt{\frac{\Gamma^{\rm n}_{{\rm p},j=1/2}}{\Gamma^{\rm n}_{\rm p}}}. \tag{2.9}$$

On the other hand, the ratio of the $j = 3/2$ part to the neutron width of the p-wave resonance can be written as $y = \sqrt{\Gamma^{\rm n}_{{\rm p},j=3/2}/\Gamma^{\rm n}_{\rm p}}$, and x and y satisfy

$$x^2 + y^2 = 1, \tag{2.10}$$

because of the relation of $\Gamma^{\rm n}_{\rm p} = \Gamma^{\rm n}_{{\rm p},j=1/2} + \Gamma^{\rm n}_{{\rm p},j=3/2}$. Then a mixing angle ϕ can be defined, and x and y can be written as

$$x = \cos\phi \quad \text{and} \quad y = \sin\phi. \tag{2.11}$$

Two types of enhancement mechanisms which are considered to contribute to the large magnitude of $A_{\rm L}$. One of them is "dynamical enhancement" and the other is "structural enhancement".

The "dynamical enhancement" originates from the statistical nature of the compound states. The wave functions of s- and p-wave states can be described as the sum of many single particle-hole states in the nuclear shell model calculated by the following equations:

$$|{\rm s}\rangle = \sum_i^N a_i |i\rangle \quad \text{and} \quad |{\rm p}\rangle = \sum_j^N b_j |j\rangle, \tag{2.12}$$

where $|i\rangle$ and $|j\rangle$ are the wave functions of the single particle-hole states. The magnitude of coefficients a_i and b_j are on the order of $\sim 1/\sqrt{N}$ as a result of the normalization of the wave functions $|{\rm s}\rangle$ and $|{\rm p}\rangle$. The number of states N is estimated as

$$N \sim \frac{\Delta E}{D}, \tag{2.13}$$

where ΔE is the energy required for one nucleus to excite from the ground state, and D is the average distance between compound states. The typical values of $\Delta E \sim 10^6$ eV and $D \sim 10$ eV make N to be the order of 10^5. Therefore, the size of the weak matrix element can be estimated as

$$\begin{aligned} |W| &= |\langle {\rm s}|H_{\rm PNC}|{\rm p}\rangle| \\ &= \left| \sum_{i,j}^N a_i b_j \langle i|H_{\rm PNC}|j\rangle \right| \\ &\sim \overline{\langle i|H_{\rm PNC}|j\rangle} \times \sqrt{N}. \end{aligned} \tag{2.14}$$

Thus, the factor $2W/(E_{\rm p} - E_{\rm s})$ in Eq. (2.8) can be written as

$$\frac{2W}{E_{\rm p} - E_{\rm s}} \sim \frac{|W|}{D} \sim \frac{\overline{\langle i|H_{\rm PNC}|j\rangle}}{\Delta E} \times \sqrt{N}, \tag{2.15}$$

where $\overline{\langle i|H_{\rm PNC}|j\rangle}/\Delta E$ is the magnitude of the P-violating effect in the single-particle state and its order is $\sim 10^{-7}$. Equation (2.15) shows that the P-violating effect in the compound states is enhanced compared to that in the single-particle state by $\sqrt{N} = 10^2 \sim 10^3$.

The other enhancement factor, "structural enhancement", comes from the ratio of the neutron widths of two compound states. The neutron width is proportional to a factor of the centrifugal potential, so that the neutron widths of s- and p-wave resonances are described as

$$\Gamma_{\rm s}^{\rm n} \propto kR \quad \text{and} \quad \Gamma_{\rm p}^{\rm n} \propto (kR)^3, \tag{2.16}$$

where k is the neutron momentum, and R is the radius of the nucleus. Therefore, the "structural enhancement" is given as

$$\sqrt{\frac{\Gamma_{\rm s}^{\rm n}}{\Gamma_{\rm p}^{\rm n}}} \sim \frac{1}{kR}. \tag{2.17}$$

Typical values of $k \sim 2 \times 10^{-4}$ fm and $R \sim 10$ fm makes the value of $1/kR$ to be the order of 10^3. When x is the order of 1, the longitudinal asymmetry $A_{\rm L}$ can become $\sim 10^{-1}$. However, x has not been experimentally determined yet for various nuclei.

2.2 Enhancement of T-violation in a compound nucleus

The enhancement mechanism of P-violation described in the previous section can be generalized to other discrete symmetry for the case that two states, having opposite polarities under the symmetry operation, are connected on the entrance channel into the compound states. V. P. Gudkov predicted that T-violation could be also enhanced through the similar mechanism as the enhancement of the P-violation in the compound states [41, 42]. The total angular momentum of the compound state denoted by $\boldsymbol{J}$ is given as

$$\boldsymbol{J} = \boldsymbol{l} + \boldsymbol{s} + \boldsymbol{I}, \tag{2.18}$$

where $\boldsymbol{I}$ is the target nuclear spin. The wave function of the compound state is described as $|lsI\rangle$ and is transformed by the P transformation as

$$\hat{P}|lsI\rangle \rightarrow (-1)^l |lsI\rangle. \tag{2.19}$$

Equation (2.19) indicates that the eigenvalue for the P transformation is determined by the orbital angular momentum l. This indicates that the P-violating effect is caused by interference between the two states which have different orbital angular momentum. On the other hand, the wave function $|lsI\rangle$ is transformed by the time-reversal operation as

$$\hat{T}|lsI\rangle \rightarrow (-1)^{i\pi S_y} \hat{K}|lsI\rangle, \tag{2.20}$$

where $\hat{K}$ is the complex conjugate matrix, and S_y is the y component of the channel spin $\boldsymbol{S}$ described as $\boldsymbol{S} = \boldsymbol{s} + \boldsymbol{I}$ [1]. Equation (2.20) indicates the eigenvalue for the time-reversal transformation is determined by the channel spin. The T-violating effect in the compound states is caused by interference between two states which have different channel spins. Therefore, the enhancement of T-violation can be

[1] The S_y is the imaginary part of the channel spin $\boldsymbol{S}$. This notation follows that of the Pauli matrix.

calculated by recombining angular momenta as

$$\begin{aligned} |J(l,S(sI))\rangle &= \sum_j \langle\langle J(j(ls),I)|J(l,S(sI))\rangle|J(j(ls),I)\rangle \\ &= \sum_j (-1)^{l+s+I+J}\sqrt{(2j+1)(2S+1)}\begin{Bmatrix} I & s & l \\ I & S & j \end{Bmatrix}|J(j(ls),I)\rangle. \end{aligned} \tag{2.21}$$

Here, the partial widths of the channel spin are defined as

$$x_S \equiv \sqrt{\frac{\Gamma^{\rm n}_{\rm p}(S=I-1/2)}{\Gamma^{\rm n}_{\rm p}}} \quad \text{and} \quad y_S \equiv \sqrt{\frac{\Gamma^{\rm n}_{\rm p}(S=I+1/2)}{\Gamma^{\rm n}_{\rm p}}}, \tag{2.22}$$

and they can be described as the result of the recombination as

$$\begin{pmatrix} x_S \\ y_S \end{pmatrix} = \begin{cases} \frac{1}{\sqrt{3(2I+1)}}\begin{pmatrix} -\sqrt{2I-1} & 2\sqrt{I+1} \\ 2\sqrt{I+1} & \sqrt{2I-1} \end{pmatrix}\begin{pmatrix} x \\ y \end{pmatrix} & (J=I-\frac{1}{2}) \\ \frac{1}{\sqrt{3(2I+1)}}\begin{pmatrix} -\sqrt{2I} & \sqrt{2I+3} \\ \sqrt{2I+3} & 2\sqrt{2I} \end{pmatrix}\begin{pmatrix} x \\ y \end{pmatrix} & (J=I+\frac{1}{2}). \end{cases} \tag{2.23}$$

The large-enhanced P-violation at the p-wave resonance is proportional to xW, while the magnitude of T-violation is considered to be proportional to $x_S W_{\rm T}$, where $W_{\rm T}$ is the matrix element of the T-violating interactions. The size of the T-violating matrix element $W_{\rm T}$ can be represented by converting the mixing of different channel spins into s-p mixing and the relative size of T-violating cross section $\Delta\sigma_{\rm T}$ to the P-violating cross section $\Delta\sigma_{\rm P}$ can be described as

$$\begin{aligned} \frac{\Delta\sigma_{\rm T}}{\Delta\sigma_{\rm P}} &= \frac{\langle S_y|H_{\rm TRIV}|S'_y\rangle}{\langle {\rm s}|H_{\rm PNC}|{\rm p}\rangle} \\ &= \kappa(J)\frac{\langle {\rm s}|H_{\rm TRIV}|{\rm p}\rangle}{\langle {\rm s}|H_{\rm PNC}|{\rm p}\rangle} \\ &= \kappa(J)\frac{W_{\rm T}}{W}, \end{aligned} \tag{2.24}$$

where $H_{\rm TRIV}$ is a Hamiltonian of time-reversal invariance violating (TRIV) interactions, and $\kappa(J)$ is a spin factor which can be given as a function of x and y as follows:

$$\kappa(J) = \begin{cases} (-1)^{2I}\left(1+\frac{1}{2}\sqrt{\frac{2I-1}{I+1}}\frac{y}{x}\right) & (J=I-\frac{1}{2}) \\ (-1)^{2I+1}\frac{I}{I+1}\left(1-\frac{1}{2}\sqrt{\frac{2I+3}{I}}\frac{y}{x}\right) & (J=I+\frac{1}{2}). \end{cases} \tag{2.25}$$

Here, $\kappa(J)$ can be rewritten as a function of the mixing angle ϕ using Eq. (2.11). Equation (2.24) indicates that the sensitivity of the T-violating effect in the compound states strongly depends on the value of ϕ. Figure 2.3 shows the ϕ dependencies of the absolute values of $\kappa(J)$ for ^{81}Br, ^{117}Sn, ^{131}Xe, and ^{139}La. The method to determine the value of ϕ is explained in Chapter 3.

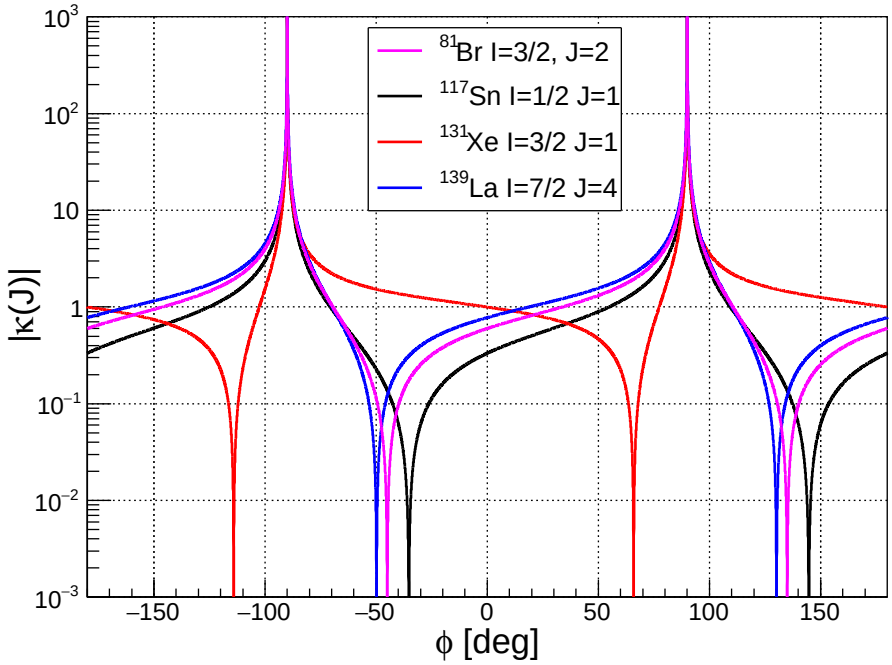

Figure 2.3: Comparison of the ϕ dependence of the absolute value of $\kappa(J)$ for several nuclei.

2.3 NOPTREX project

Neutron Optics for Time Reversal Experiment (NOPTREX) collaboration aims to realize a sensitive search for T-violation using polarized neutrons and polarized nuclear targets which possess p-wave resonances. In this section, a measurement principle and candidate nuclei for T-violation search are explained.

2.3.1 Measurement principle of the T-violation search

A search for the T-violating effect obtained by measuring the neutron transmission has the advantage that T-odd effects in the final-state interaction are expected to be negligibly small. This is because neutron propagation does not change in the process of neutrons passing through the target.

When the polarization of the target nucleus is a pure vector polarization, the forward scattering amplitude f can be written as

$$f = A' + B'(\boldsymbol{\sigma}_{\rm n} \cdot \hat{\boldsymbol{I}}) + C'(\boldsymbol{\sigma}_{\rm n} \cdot \boldsymbol{k}_{\rm n}) + D'(\boldsymbol{\sigma}_{\rm n} \cdot (\boldsymbol{k}_{\rm n} \times \hat{\boldsymbol{I}})), \tag{2.26}$$

where $\boldsymbol{\sigma}_{\rm n}$, $\boldsymbol{k}_{\rm n}$, and $\hat{\boldsymbol{I}}$ denote the spin of incident neutrons, momentum of incident neutrons, and spin of the target nucleus, respectively. In the case of the nucleus with $I = 1/2$ and $J = 1$, the neutron-energy-dependent coefficient of each term in

Eq. (2.26) is given as

$$A' = -\frac{3}{8k}\left(\frac{\Gamma_{\rm s}^{\rm n}}{E_{\rm n}-E_{\rm s}+i\Gamma_{\rm s}/2}+\frac{\Gamma_{\rm p}^{\rm n}}{E_{\rm n}-E_{\rm p}+i\Gamma_{\rm p}/2}\right)+\frac{3}{4}a_{\rm s}, \tag{2.27a}$$

$$B' = \frac{M}{4k}\left(-\frac{\Gamma_{\rm s}^{\rm n}}{E_{\rm n}-E_{\rm s}+i\Gamma_{\rm s}/2}+3\frac{x_S^2\Gamma_{\rm p}^{\rm n}}{E_{\rm n}-E_{\rm p}+i\Gamma_{\rm p}/2}\right)+\frac{M}{2}a_{\rm s}, \tag{2.27b}$$

$$C' = \frac{\sqrt{3}}{4k}\frac{\sqrt{\Gamma_{\rm s}^{\rm n}}W\sqrt{\Gamma_{\rm p}^{\rm n}}}{(E_{\rm n}-E_{\rm p}+i\Gamma_{\rm p}/2)(E_{\rm n}-E_{\rm s}+i\Gamma_{\rm s}/2)}(x_S-\sqrt{2}y_S), \tag{2.27c}$$

$$D' = -\frac{\sqrt{3}M}{4k}x_S\frac{\sqrt{\Gamma_{\rm s}^{\rm n}}W_{\rm T}\sqrt{\Gamma_{\rm p}^{\rm n}}}{(E_{\rm n}-E_{\rm p}+i\Gamma_{\rm p}/2)(E_{\rm n}-E_{\rm s}+i\Gamma_{\rm s}/2)}, \tag{2.27d}$$

where $\Gamma_{\rm s}$ and $\Gamma_{\rm p}$ are the resonance widths of s- and p-wave resonances, respectively [43]. The variable $a_{\rm s}$ is the potential scattering length[2]. The variable M is the spin projection, and it satisfies $M = \pm 1/2$. The P-odd correlation term C' and the P-odd T-odd correlation term D' can be related as

$$\frac{D'}{C'} \propto \kappa(J)\frac{W_{\rm T}}{W}. \tag{2.28}$$

Under the optical description for the behavior of the neutron spin in the polarized target, the spinors of the initial and final states denoted by U_i and U_f are related via a density matrix $\mathfrak{S}$ as

$$\begin{aligned} U_f &= \mathfrak{S}U_i, \\ \mathfrak{S} &= e^{i(n-1)kz}, \\ n &= 1+\frac{2\pi\rho}{k^2}f, \end{aligned} \tag{2.29}$$

where z is the thickness of the target, ρ is the number density of the material, and k is the neutron wave number [44]. Here, $\mathfrak{S}$ is described as

$$\mathfrak{S} = A + B(\boldsymbol{\sigma}_{\rm n}\cdot\hat{\boldsymbol{I}}) + C(\boldsymbol{\sigma}_{\rm n}\cdot\boldsymbol{k}_{\rm n}) + D(\boldsymbol{\sigma}_{\rm n}\cdot(\boldsymbol{k}_{\rm n}\times\hat{\boldsymbol{I}})), \tag{2.30}$$

where the coefficients can be written as

$$\begin{aligned} A &= e^{iZA'}\cos b, \\ B &= e^{iZA'}\frac{\sin b}{b}ZB', \\ C &= e^{iZA'}\frac{\sin b}{b}ZC', \\ D &= e^{iZA'}\frac{\sin b}{b}ZD', \\ Z &= \frac{2\pi\rho z}{k}, \\ b &= Z\sqrt{B'^2+C'^2+D'^2}. \end{aligned} \tag{2.31}$$

[2]The scattering length can be calculated using the cross sections of coherent scattering and incoherent scattering, which is described in Appendix A

The coefficient A is the spin-independent (P-even, T-even) term corresponding to the neutron capture cross section, and $|A|^2$ represents the transmission of neutrons passing through the target. The coefficient B is the spin-dependent (P-even, T-even) term corresponding to a neutron-spin rotation effect inside the polarized target, which is called the "pseudo-magnetic effect". The coefficient C is a P-violating (P-odd, T-even) term which is enhanced for various nuclei. The coefficient D is a T-violating (P-odd, T-odd) term which can be enhanced in proportion to the C term. Note that Eq. (2.30) is the formalism for the case of $I = 1/2$, and tensor terms need to be added for the case of $I > 1/2$. The non-zero value of D implies the discovery of T-violation in the compound states. However, the contribution of the tensor terms is expected to be smaller than the term described in Eq. (2.30). In this dissertation, the tensor terms do not be considered because the case of ^{117}Sn with $I = 1/2$ is discussed. Figure 2.4 shows a schematic view of the measurement principle of the D term with polarized neutrons and the polarized target. A coordinate system defines the beam axis as the z-axis, the vertical direction as the y-axis, and the direction perpendicular to them as the x-axis.

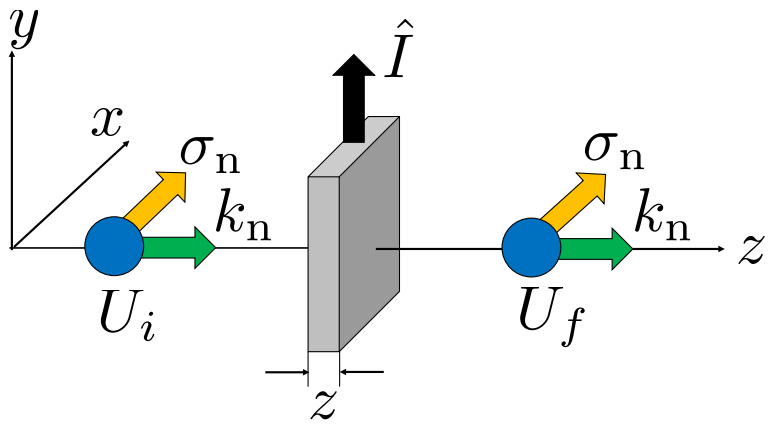

Figure 2.4: Measurement principle of D term with polarized neutrons and a polarized target.

Here, some spin-dependent observables to extract the D term are proposed. The D term can be searched with high sensitivity by measuring the analyzing power $\boldsymbol{A}$ and the polarization $\boldsymbol{P}$. They are defined as

$$\boldsymbol{A} \equiv \frac{\mathrm{Tr}(\mathfrak{S}^\dagger \boldsymbol{\sigma} \mathfrak{S})}{\mathrm{Tr}(\mathfrak{S}^\dagger \mathfrak{S})} \quad \text{and} \quad \boldsymbol{P} \equiv \frac{\mathrm{Tr}(\boldsymbol{\sigma} \mathfrak{S}^\dagger \mathfrak{S})}{\mathrm{Tr}(\mathfrak{S}^\dagger \mathfrak{S})}, \tag{2.32}$$

where $\boldsymbol{\sigma}$ is the neutron spin. When the target spin polarization is parallel to the y axis, the observables are obtained for each direction of the neutron spin polarization as follows.

$$\begin{aligned}
A_x &= 4(\mathrm{Re}A^*D + \mathrm{Im}B^*C)/|A|^2, \;\; P_x = 4(\mathrm{Re}A^*D - \mathrm{Im}B^*C)/|A|^2, \\
A_y &= 4(\mathrm{Re}A^*B + \mathrm{Im}C^*D)/|A|^2, \;\; P_y = 4(\mathrm{Re}A^*B - \mathrm{Im}C^*D)/|A|^2, \\
A_z &= 4(\mathrm{Re}A^*C + \mathrm{Im}D^*B)/|A|^2, \;\; P_z = 4(\mathrm{Re}A^*C - \mathrm{Im}D^*B)/|A|^2.
\end{aligned}$$

Figure 2.5 shows a simple illustration of the experimental setups for the measurement of the analyzing powers and polarizations. The sum of the analyzing power along the x-axis (A_x) and the polarization along x-axis (P_x) is the most sensitive observable, and it is given as

$$A_x + P_x = \frac{8\mathrm{Re}A^* D}{|A|^2}. \tag{2.33}$$

Since the value of D is proportional to $\kappa(J)$, the value of $\kappa(J)$ needs to be determined for estimating the experimental sensitivity of T-violation in the compound states.

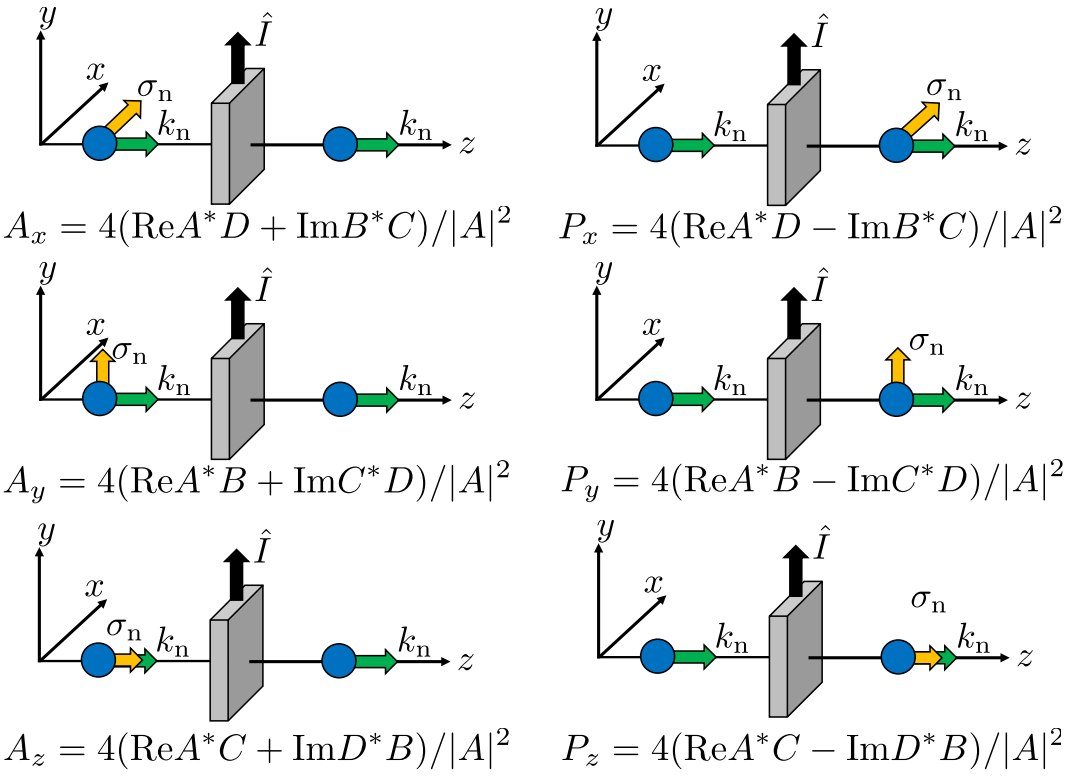

Figure 2.5: Combinations of observables proportional to the D term.

2.3.2 Candidate nuclei for the T-violation search

The experimental sensitivity of T-violation depends on nuclides. Therefore, suitable nuclei need to be selected with high sensitivity, for which the guiding principles are as follows.

1. Large longitudinal asymmetry A_L.
2. Large value of $|\kappa(J)|$.
3. Low p-wave resonance energy at which P-violation occurs.

4. Large natural abundance ratio.

5. Spin polarization is possible.

The 3rd condition is derived from the fact that the neutron beam intensity is higher at lower energies in the epithermal region. Generally, it is likely to be polarized with the smaller spin. Table 2.2 summarizes the candidate nuclei for T-violation search. The nuclei whose spin is zero are not listed in this table because they cannot be polarized. The value of $\kappa(J)$ was determined for only ^{139}La by T. Okudaira *et al.* [45]. Moreover, there is a report that polarization can be achieved using $LaAlO_3$ crystal with dynamic nuclear polarization (DNP) [46]. Thus, ^{139}La is the first candidate nucleus for T-violation search.

Table 2.2: Candidate nuclei for T-violation search. The nuclei whose P-violation was observed with over 2σ, resonance energy is less than 10 eV, and nuclear spin I is non-zero are listed.

	E_{p} [eV]	A_{L} [%]	I	Abundance [%]	Polarization method
^{139}La	0.758	9.8 ± 0.2	7/2	99.91	DNP [46]
^{81}Br	0.88	0.77 ± 0.33	3/2	49.31	-
^{117}Sn	1.327	0.79 ± 0.04	1/2	7.68	-
^{131}Xe	3.2	4.3 ± 0.2	3/2	21.2	SEOP
^{115}In	6.853	-1.45 ± 0.11	9/2	95.72	DNP [47]
^{113}Cd	7.00	-0.80 ± 0.33	3/2	12.22	-
^{133}Cs	9.50	0.24 ± 0.02	7/2	100	-

2.3.3 Properties of ^{117}Sn

The nuclide ^{117}Sn is focused as the next candidate nucleus. The nuclide ^{117}Sn is expected to be able to polarize due to its spin $I = 1/2$. The cross sections of ^{117}Sn with neutrons are described by elastic scattering and capture reaction in the epithermal neutron energy region as shown in Fig. 2.6. The resonance parameters of neutron capture are listed in Table 2.3. When a neutron is captured by ^{117}Sn, the neutron-induced compound state of ^{118}Sn has an energy of 9327 keV which corresponds to the neutron-separation energy. Subsequently, the compound state decays to the ground state by γ-ray emission. The level scheme related to $^{117}\mathrm{Sn}(\mathrm{n},\gamma)^{118}\mathrm{Sn}$ reaction is schematically shown in Fig. 2.7.

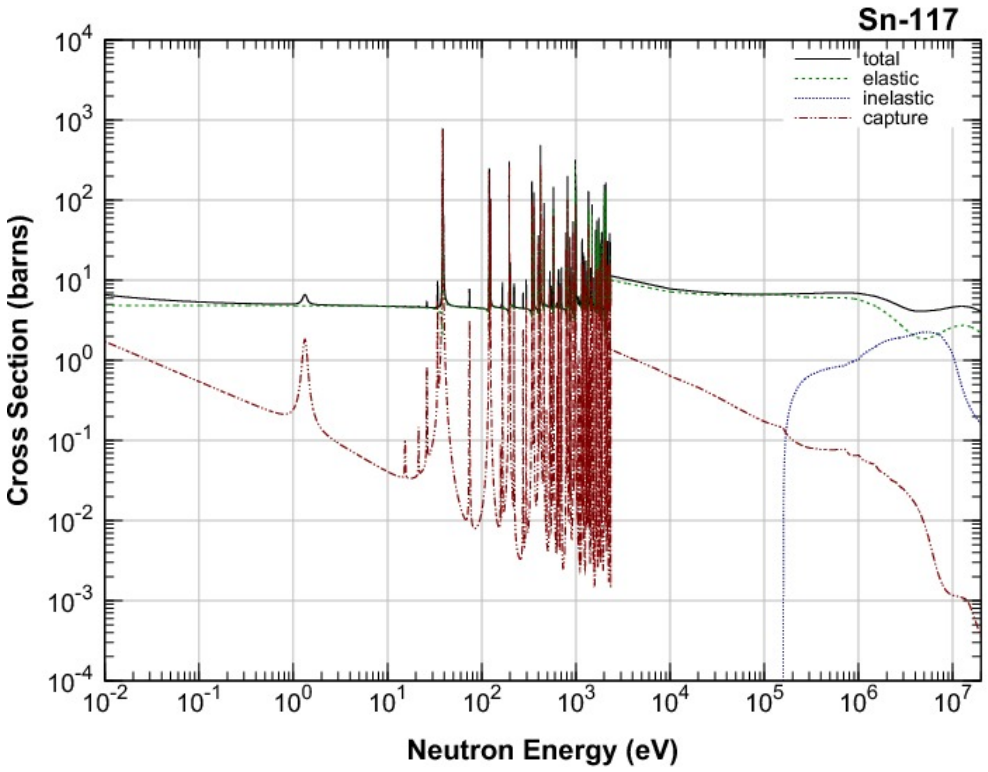

Figure 2.6: Cross sections of ^{117}Sn with neutron [48].

Table 2.3: Resonance parameters of ^{117}Sn. The values with the index (a) and (b) are taken from Refs. [49] and [50], respectively. Others are taken from Refs. [49] and [50].

E_0 [eV]	J	l	Γ^γ [meV]	$g\Gamma^{\rm n}$ [meV]	$g\Gamma^{{\rm n}l}$ [meV]
$-29.2^{(a)}$	$1^{(b)}$	0	$(91)^{(a)}$	-	$5.55^{(a)}$
1.327 ± 0.001	1	1	148 ± 10	$(1.38 \pm 0.07) \times 10^{-4}$	
15.385 ± 0.016	-	1	136 ± 18	$(0.92 \pm 0.05) \times 10^{-4}$	
21.390 ± 0.025	-	1	113 ± 16	$(2.06 \pm 0.11) \times 10^{-4}$	
26.215 ± 0.034	-	1	129 ± 8	$(2.07 \pm 0.10) \times 10^{-3}$	
34.044 ± 0.017	-	1	$119 \pm 9^{(a)}$	$(1.87 \pm 0.09) \times 10^{-2}$	
38.80 ± 0.05	1	0	$100 \pm 15^{(a)}$	3.10 ± 0.15	
74.39 ± 0.05	-	1	-	$(3.4 \pm 0.2) \times 10^{-2}$	
120.54 ± 0.06	1	0	107 ± 12	4.95 ± 0.25	

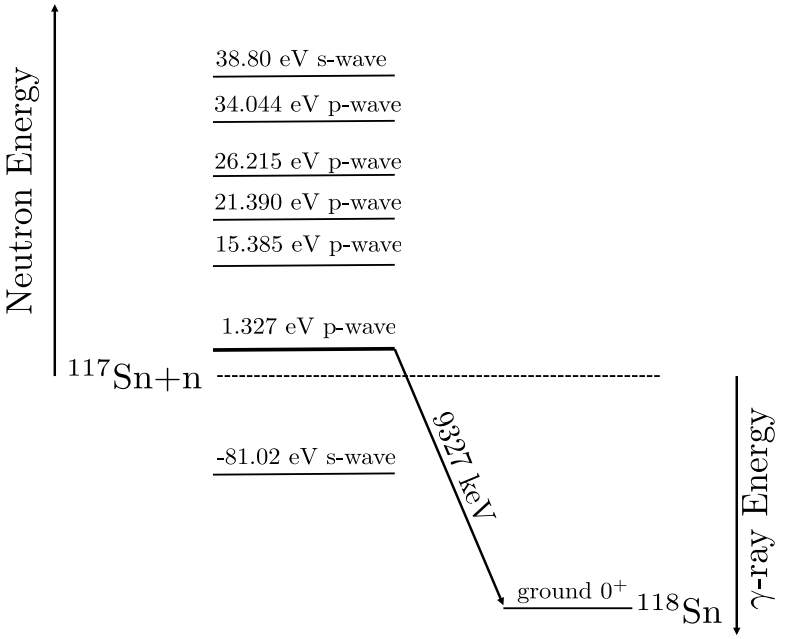

Figure 2.7: Transitions from ^{117}Sn+n to ^{118}Sn.

Chapter 3

Angular correlation in (n,γ) reaction

In this chapter, a formalism which describes the angular dependence of (n,γ) reaction based on interference between s-wave resonance amplitudes and a p-wave resonance amplitude is explained. This formalism includes the mixing angle ϕ which is the parameter to determine the $\kappa(J)$ value. In a previous study, the angular correlation was measured and the value of ϕ was determined. The difference between the previous study and this study is explained.

3.1 Formalism of cross section of (n,γ) reaction

The Feynman diagrams of the amplitudes of the (n,γ) reaction via compound states can be represented as shown in Fig. 3.1. Diagrams (1) and (2) in Fig. 3.1 correspond to the processes without P-violation. In these processes, a neutron is captured as an s-wave or a p-wave states as an entrance channel, the neutron and a nucleus form a compound state. After that, a γ ray is emitted from the compound state as an exit channel. Diagrams (3) and (4) in Fig. 3.1 correspond to the processes with P-violation. In these P-violating processes, the parity changes by the weak interaction after neutron capture. The amplitudes corresponding to these processes (f_1 to f_4) are written as

$$
\begin{aligned}
f_1 &= -\frac{1}{2k}\sum_{\mathrm{s}}\frac{\langle f,\gamma|H_{\mathrm{EM}}|\mathrm{s}\rangle\langle\mathrm{s}|H_{\mathrm{s}}|\mathrm{n}\rangle}{E_{\mathrm{n}}-E_{\mathrm{s}}+i\Gamma_{\mathrm{s}}/2},\\
f_2 &= -\frac{1}{2k}\sum_{\mathrm{p}}\frac{\langle f,\gamma|H_{\mathrm{EM}}|\mathrm{p}\rangle\langle\mathrm{p}|H_{\mathrm{s}}|\mathrm{n}\rangle}{E_{\mathrm{n}}-E_{\mathrm{p}}+i\Gamma_{\mathrm{p}}/2},\\
f_3 &= -\frac{1}{2k}\sum_{\mathrm{s,p}}\frac{\langle f,\gamma|H_{\mathrm{EM}}|\mathrm{p}\rangle\langle\mathrm{p}|H_{\mathrm{w}}|\mathrm{s}\rangle\langle\mathrm{s}|H_{\mathrm{s}}|\mathrm{n}\rangle}{(E_{\mathrm{n}}-E_{\mathrm{p}}+i\Gamma_{\mathrm{p}}/2)(E_{\mathrm{n}}-E_{\mathrm{s}}+i\Gamma_{\mathrm{s}}/2)},\\
f_4 &= -\frac{1}{2k}\sum_{\mathrm{s,p}}\frac{\langle f,\gamma|H_{\mathrm{EM}}|\mathrm{s}\rangle\langle\mathrm{s}|H_{\mathrm{w}}|\mathrm{p}\rangle\langle\mathrm{p}|H_{\mathrm{s}}|\mathrm{n}\rangle}{(E_{\mathrm{n}}-E_{\mathrm{s}}+i\Gamma_{\mathrm{s}}/2)(E_{\mathrm{n}}-E_{\mathrm{p}}+i\Gamma_{\mathrm{p}}/2)},
\end{aligned}
\tag{3.1}
$$

where H_{EM} and H_{w} are the Hamiltonians of the electromagnetic interaction and the weak interaction, respectively. H_{s} is the Hamiltonian of the residual interaction

which is responsible for the neutron capture. The wave function $|\mathrm{n}\rangle$ is the initial neutron state and the wave function $|f,\gamma\rangle$ is the final state of the nucleus and γ-quantum.

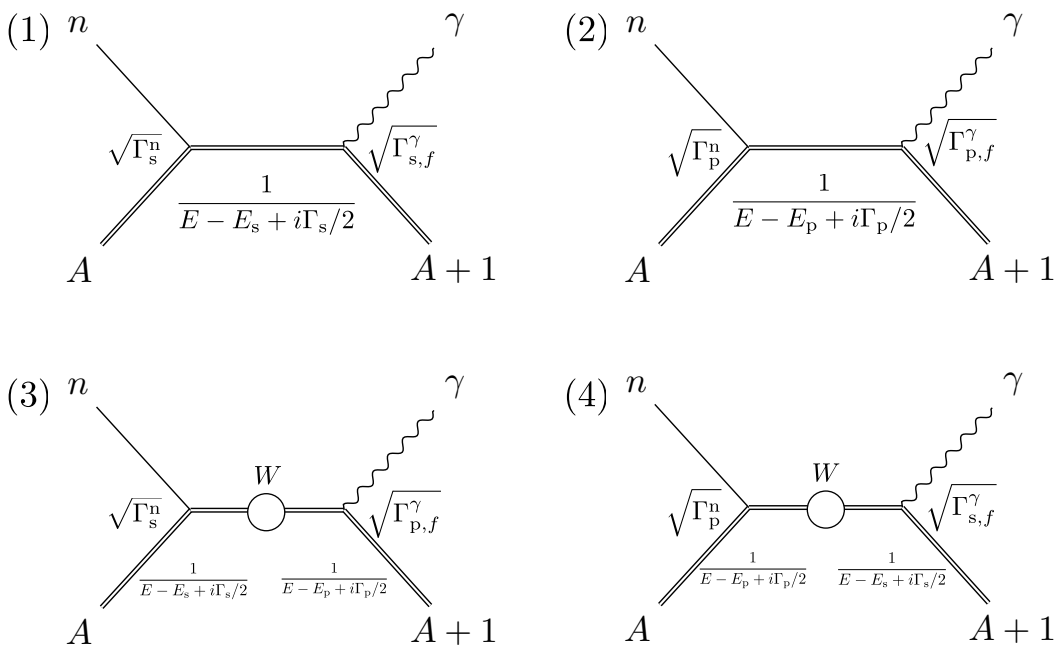

Figure 3.1: Feynman diagrams for amplitudes in (n,γ) reaction.

The amplitudes V_1 to V_4, which are invariant for three-dimensional rotations corresponding to the amplitudes f_1 to f_4, are given as

$$
\begin{aligned}
V_1(E_{\mathrm{n}},J_{\mathrm{s}}) &= -\frac{1}{2k}\sum_{\mathrm{s}}\frac{\sqrt{g_{\mathrm{s}}\Gamma^{\mathrm{n}}_{\mathrm{s}}\Gamma^{\gamma}_{\mathrm{s},f}}}{E_{\mathrm{n}}-E_{\mathrm{s}}+i\Gamma_{\mathrm{s}}/2},\\
V_2(E_{\mathrm{n}},J_{\mathrm{p}}) &= -\frac{1}{2k}\sum_{\mathrm{p}}\frac{\sqrt{g_{\mathrm{p}}\Gamma^{\mathrm{n}}_{\mathrm{p}}\Gamma^{\gamma}_{\mathrm{p},f}}}{E_{\mathrm{n}}-E_{\mathrm{p}}+i\Gamma_{\mathrm{p}}/2},\\
V_3(E_{\mathrm{n}},J_{\mathrm{s}}=J_{\mathrm{p}}) &= -\frac{1}{2k}\sum_{\mathrm{s,p}}\frac{\sqrt{g_{\mathrm{s}}\Gamma^{\mathrm{n}}_{\mathrm{s}}}W\sqrt{\Gamma^{\gamma}_{\mathrm{p},f}}}{(E_{\mathrm{n}}-E_{\mathrm{p}}+i\Gamma_{\mathrm{p}}/2)(E_{\mathrm{n}}-E_{\mathrm{s}}+i\Gamma_{\mathrm{s}}/2)},\\
V_4(E_{\mathrm{n}},J_{\mathrm{p}}=J_{\mathrm{s}}) &= -\frac{1}{2k}\sum_{\mathrm{s,p}}\frac{\sqrt{g_{\mathrm{p}}\Gamma^{\mathrm{n}}_{\mathrm{p}}}W\sqrt{\Gamma^{\gamma}_{\mathrm{s},f}}}{(E_{\mathrm{n}}-E_{\mathrm{s}}+i\Gamma_{\mathrm{s}}/2)(E_{\mathrm{n}}-E_{\mathrm{p}}+i\Gamma_{\mathrm{p}}/2)},
\end{aligned}
\tag{3.2}
$$

where k is the momentum of the neutron, E_{n} is the kinetic energy of the neutron, E_r is the resonance energy of a neutron resonance r, Γ^{n}_r is the neutron width, $\Gamma^{\gamma}_{r,f}$ is the partial γ width of the transition to a final state f, and W is the weak matrix

element. The γ width is given by the sum of the partial γ widths ($\Gamma^{\gamma}_{r,f}$) as

$$\Gamma^{\gamma}_{r} = \sum_{f} \Gamma^{\gamma}_{r,f} \,. \tag{3.3}$$

The partial γ width can be described using a transition ratio to a certain final state B_f as

$$\Gamma^{\gamma}_{r,f} = B_f \Gamma^{\gamma}_{r} \,, \text{where} \quad \textstyle\sum_f B_f = 1 \,. \tag{3.4}$$

The resonance width Γ_r can be described as the sum of the neutron width $\Gamma^{\rm n}_r$ and the γ width of its resonance Γ^{γ}_r as

$$\Gamma_r = \Gamma^{\rm n}_r + \Gamma^{\gamma}_r \,. \tag{3.5}$$

Here, the statistical factor g_r is described as

$$g_r = \frac{2J_r + 1}{2(2I+1)}, \tag{3.6}$$

where I is the nuclear spin and J_r is the total spin of the compound state of the resonance r.

When the interference between an s-wave and a p-wave amplitude is considered, the amplitudes V_1 to V_4 are given by

$$\begin{aligned}
V_1(E_{\rm n}, J_{\rm s}) &= -\frac{1}{2k} \frac{\sqrt{g_{\rm s}\Gamma^{\rm n}_{\rm s}\Gamma^{\gamma}_{{\rm s},f}}(1+\alpha)}{E_{\rm n} - E_{\rm s} + i\Gamma_{\rm s}/2}, \\
V_2(E_{\rm n}, J_{\rm p}) &= -\frac{1}{2k} \frac{\sqrt{g_{\rm p}\Gamma^{\rm n}_{\rm p}\Gamma^{\gamma}_{{\rm p},f}}}{E_{\rm n} - E_{\rm p} + i\Gamma_{\rm p}/2}, \\
V_3(E_{\rm n}, J_{\rm s} = J_{\rm p}) &= -\frac{1}{2k} \frac{\sqrt{g_{\rm s}\Gamma^{\rm n}_{\rm s}} W \sqrt{\Gamma^{\gamma}_{{\rm p},f}}(1+\beta)}{(E_{\rm n} - E_{\rm p} + i\Gamma_{\rm p}/2)(E_{\rm n} - E_{\rm s} + i\Gamma_{\rm s}/2)}, \\
V_4(E_{\rm n}, J_{\rm p} = J_{\rm s}) &= -\frac{1}{2k} \frac{\sqrt{g_{\rm p}\Gamma^{\rm n}_{\rm p}} W \sqrt{\Gamma^{\gamma}_{{\rm s},f}}(1+\gamma)}{(E_{\rm n} - E_{\rm s} + i\Gamma_{\rm s}/2)(E_{\rm n} - E_{\rm p} + i\Gamma_{\rm p}/2)},
\end{aligned} \tag{3.7}$$

where α is the contribution term of other far s-wave resonances, and β and γ are the correction terms taken into account the contributions of the other far s-wave resonances. Here, these amplitudes using the transition ratios can be described as

$$\begin{aligned}
V_{1(2)}(E_{\rm n}, J_{\rm s(p)}) &= \sqrt{B_{\rm s(p),f}}\, V'_{1(2)}(E_{\rm n}, J_{\rm s(p)}), \\
V_{3(4)}(E_{\rm n}, J_{\rm s(p)} = J_{\rm p(s)}) &= \sqrt{B_{\rm s(p),f}}\, V'_{3(4)}(E_{\rm n}, J_{\rm s(p)}),
\end{aligned} \tag{3.8}$$

where

$$
\begin{aligned}
V_1'(E_\mathrm{n}, J_\mathrm{s}) &= -\frac{1}{2k}\frac{\sqrt{g_\mathrm{s}\Gamma_\mathrm{s}^\mathrm{n}\Gamma_\mathrm{s}^\gamma}(1+\alpha)}{E_\mathrm{n}-E_\mathrm{s}+i\Gamma_\mathrm{s}/2}, \\
V_2'(E_\mathrm{n}, J_\mathrm{p}) &= -\frac{1}{2k}\frac{\sqrt{g_\mathrm{p}\Gamma_\mathrm{p}^\mathrm{n}\Gamma_\mathrm{p}^\gamma}}{E_\mathrm{n}-E_\mathrm{p}+i\Gamma_\mathrm{p}/2}, \\
V_3'(E_\mathrm{n}, J_\mathrm{s}=J_\mathrm{p}) &= -\frac{1}{2k}\frac{\sqrt{g_\mathrm{s}\Gamma_\mathrm{s}^\mathrm{n}}W\sqrt{\Gamma_\mathrm{p}^\gamma}(1+\beta)}{(E_\mathrm{n}-E_\mathrm{p}+i\Gamma_\mathrm{p}/2)(E_\mathrm{n}-E_\mathrm{s}+i\Gamma_\mathrm{s}/2)}, \\
V_4'(E_\mathrm{n}, J_\mathrm{p}=J_\mathrm{s}) &= -\frac{1}{2k}\frac{\sqrt{g_\mathrm{p}\Gamma_\mathrm{p}^\mathrm{n}}W\sqrt{\Gamma_\mathrm{s}^\gamma}(1+\gamma)}{(E_\mathrm{n}-E_\mathrm{s}+i\Gamma_\mathrm{s}/2)(E_\mathrm{n}-E_\mathrm{p}+i\Gamma_\mathrm{p}/2)}.
\end{aligned} \tag{3.9}
$$

The differential cross section of (n,γ) reaction for polarized and unpolarized neutrons can be written as

$$
\begin{aligned}
\frac{d\sigma}{d\Omega} &= \frac{1}{2}\Bigg[a_0 + a_1\boldsymbol{k}_\mathrm{n}\cdot\boldsymbol{k}_\gamma + a_2\boldsymbol{\sigma}_\mathrm{n}\cdot(\boldsymbol{k}_\mathrm{n}\times\boldsymbol{k}_\gamma) + a_3\left((\boldsymbol{k}_\mathrm{n}\cdot\boldsymbol{k}_\gamma)^2-\frac{1}{3}\right) \\
&+ a_4(\boldsymbol{k}_\mathrm{n}\cdot\boldsymbol{k}_\gamma)(\boldsymbol{\sigma}_\mathrm{n}\cdot(\boldsymbol{k}_\mathrm{n}\times\boldsymbol{k}_\gamma)) + a_5(\boldsymbol{\sigma}_\gamma\cdot\boldsymbol{k}_\gamma)(\boldsymbol{\sigma}_\mathrm{n}\cdot\boldsymbol{k}_\gamma) \\
&+ a_6(\boldsymbol{\sigma}_\gamma\cdot\boldsymbol{k}_\gamma)(\boldsymbol{\sigma}_\mathrm{n}\cdot\boldsymbol{k}_\mathrm{n}) + a_7(\boldsymbol{\sigma}_\gamma\cdot\boldsymbol{k}_\gamma)\left((\boldsymbol{\sigma}_\mathrm{n}\cdot\boldsymbol{k}_\gamma)(\boldsymbol{k}_\gamma\cdot\boldsymbol{k}_\mathrm{n})-\frac{1}{3}(\boldsymbol{\sigma}_\mathrm{n}\cdot\boldsymbol{k}_\mathrm{n})\right) \\
&+ a_8(\boldsymbol{\sigma}_\gamma\cdot\boldsymbol{k}_\gamma)\left((\boldsymbol{\sigma}_\mathrm{n}\cdot\boldsymbol{k}_\mathrm{n})(\boldsymbol{k}_\mathrm{n}\cdot\boldsymbol{k}_\gamma)-\frac{1}{3}(\boldsymbol{\sigma}_\mathrm{n}\cdot\boldsymbol{k}_\gamma)\right) \\
&+ a_9\boldsymbol{\sigma}_\mathrm{n}\cdot\boldsymbol{k}_\gamma + a_{10}\boldsymbol{\sigma}_\mathrm{n}\cdot\boldsymbol{k}_\mathrm{n} + a_{11}\left((\boldsymbol{\sigma}_\mathrm{n}\cdot\boldsymbol{k}_\gamma)(\boldsymbol{k}_\gamma\cdot\boldsymbol{k}_\mathrm{n})-\frac{1}{3}(\boldsymbol{\sigma}_\mathrm{n}\cdot\boldsymbol{k}_\mathrm{n})\right) \\
&+ a_{12}(\boldsymbol{\sigma}_\mathrm{n}\cdot\boldsymbol{k}_\mathrm{n})\left((\boldsymbol{k}_\mathrm{n}\cdot\boldsymbol{k}_\gamma)-\frac{1}{3}(\boldsymbol{\sigma}_\mathrm{n}\cdot\boldsymbol{k}_\gamma)\right) \\
&+ a_{13}\boldsymbol{\sigma}_\gamma\cdot\boldsymbol{k}_\gamma + a_{14}(\boldsymbol{\sigma}_\gamma\cdot\boldsymbol{k}_\gamma)(\boldsymbol{k}_\mathrm{n}\cdot\boldsymbol{k}_\gamma) \\
&+ a_{15}(\boldsymbol{\sigma}_\gamma\cdot\boldsymbol{k}_\gamma)\boldsymbol{\sigma}_\mathrm{n}\cdot(\boldsymbol{k}_\mathrm{n}\times\boldsymbol{k}_\gamma) + a_{16}(\boldsymbol{\sigma}_\gamma\cdot\boldsymbol{k}_\gamma)\left((\boldsymbol{k}_\mathrm{n}\cdot\boldsymbol{k}_\gamma)^2-\frac{1}{3}\right) \\
&+ a_{17}(\boldsymbol{\sigma}_\gamma\cdot\boldsymbol{k}_\gamma)(\boldsymbol{k}_\mathrm{n}\cdot\boldsymbol{k}_\gamma)(\boldsymbol{k}_\mathrm{n}\cdot(\boldsymbol{k}_\mathrm{n}\times\boldsymbol{k}_\gamma))\ \Bigg]
\end{aligned} \tag{3.10}
$$

where $\boldsymbol{k}_\mathrm{n}$, $\boldsymbol{k}_\gamma$, $\boldsymbol{\sigma}_\mathrm{n}$, and $\boldsymbol{\sigma}_\gamma$ are unit vectors parallel to the incident neutron momentum, the emitted γ-ray momentum, the incident neutron spin, and the emitted γ-ray spin, respectively Expressions for the coefficients a_0 to a_{17} described by the products of amplitudes V_1 to V_4 are given in Appendix B.

3.2 Angular correlation of cross section for unpolarized neutrons

When γ-ray polarization is not measured, the observable differential cross section for unpolarized neutrons is written as

$$\begin{aligned}\frac{d\sigma}{d\Omega} &= \frac{1}{2}\left(a_0 + a_1 \boldsymbol{k}_{\rm n}\cdot\boldsymbol{k}_\gamma + a_3\left((\boldsymbol{k}_{\rm n}\cdot\boldsymbol{k}_\gamma)^2 - \frac{1}{3}\right)\right)\\ &= \frac{1}{2}\left(a_0 + a_1\cos\theta_\gamma + a_3\left(\cos^2\theta_\gamma - \frac{1}{3}\right)\right),\end{aligned} \tag{3.11}$$

where θ_γ is the polar angle of the emitted γ-ray direction with respect to the incident neutron momentum. The expressions of the coefficients a_0, a_1, and a_3 are written as

$$a_0 = \sum_{J_{\rm s}} |V_1(E_{\rm n}, J_{\rm s})|^2 + \sum_{J_{\rm p}} |V_2(E_{\rm n}, J_{\rm p})|^2, \tag{3.12a}$$

$$a_1 = 2{\rm Re}\sum_{J_{\rm s},J_{\rm p},j} V_1(E_{\rm n}, J_{\rm s})V_2^*(E_{\rm n}, J_{\rm p})P(J_{\rm s}J_{\rm p}\frac{1}{2}j1IF)z_j, \tag{3.12b}$$

$$a_3 = 3\sqrt{10}{\rm Re}\sum_{J_{\rm p},j,J'_{\rm p},j'} V_2(E_{\rm n}, J_{\rm p})V_2^*(E_{\rm n}, J'_{\rm p})P(J_{\rm p}J'_{\rm p}jj'2IF)\begin{Bmatrix}2 & 1 & 1\\ 0 & \frac{1}{2} & \frac{1}{2}\\ 2 & j & j'\end{Bmatrix} z_j z'_j, \tag{3.12c}$$

where

$$\begin{aligned}P(JJ'jj'kIF) &= (-1)^{J+J'+j'+I+F}\frac{3}{2}\sqrt{(2J+1)(2J'+1)(2j+1)(2j'+1)}\\ &\times \begin{Bmatrix}k & j & j'\\ I & J' & J\end{Bmatrix}\begin{Bmatrix}k & 1 & 1\\ F & J & J'\end{Bmatrix},\end{aligned} \tag{3.13}$$

where J, j, I, and F are the spin of the compound state, the total angular momentum of the neutron, the spin of target nuclei, and the spin of a final state, respectively. The ratios of partial neutron widths to a neutron width of a p-wave resonance are defined in Eq. (2.11) and are given as

$$z_j = \begin{cases} x = \cos\phi & (j = \frac{1}{2})\\ y = \sin\phi & (j = \frac{3}{2}).\end{cases} \tag{3.14}$$

The mixing angle ϕ can be extracted from the coefficients a_1 and a_3 in the angular correlation terms because these are both functions of x and y. The coefficients a_1 and a_3 are written as

$$\begin{aligned}a_1 &= a_{1x}x + a_{1y}y\\ a_3 &= a_{3xy}xy + a_{3yy}y^2\end{aligned} \tag{3.15}$$

where

$$
\begin{aligned}
a_{1x} &= 2\,\mathrm{Re}\sum_{J_\mathrm{s},J_\mathrm{p}} V_1(E_\mathrm{n},J_\mathrm{s})V_2^*(E_\mathrm{n},J_\mathrm{p})P(J_\mathrm{s}J_\mathrm{p}\frac{1}{2}\frac{1}{2}1IF),\\
a_{1y} &= 2\,\mathrm{Re}\sum_{J_\mathrm{s},J_\mathrm{p}} V_1(E_\mathrm{n},J_\mathrm{s})V_2^*(E_\mathrm{n},J_\mathrm{p})P(J_\mathrm{s}J_\mathrm{p}\frac{1}{2}\frac{3}{2}1IF),\\
a_{3xy} &= 3\sqrt{10}\,\mathrm{Re}\sum_{J_\mathrm{p},J_{\mathrm{p}'}} V_2(E_\mathrm{n},J_\mathrm{p})V_2^*(E_\mathrm{n},J'_\mathrm{p})P(J_\mathrm{p}J'_\mathrm{p}\frac{1}{2}\frac{3}{2}2IF)\begin{Bmatrix}2 & 1 & 1\\ 0 & \frac{1}{2} & \frac{1}{2}\\ 2 & \frac{1}{2} & \frac{3}{2}\end{Bmatrix},\\
a_{3yy} &= 3\sqrt{10}\,\mathrm{Re}\sum_{J_\mathrm{p},J_{\mathrm{p}'}} V_2(E_\mathrm{n},J_\mathrm{p})V_2^*(E_\mathrm{n},J'_\mathrm{p})P(J_\mathrm{p}J'_\mathrm{p}\frac{3}{2}\frac{3}{2}2IF)\begin{Bmatrix}2 & 1 & 1\\ 0 & \frac{1}{2} & \frac{1}{2}\\ 2 & \frac{3}{2} & \frac{3}{2}\end{Bmatrix}.
\end{aligned}
\tag{3.16}
$$

The coefficient a_{3xx} is not written in the above formula because the value of P coefficient is zero. These terms can be calculated when the values of I, J, and F are known.

In the case that an s-wave and a p-wave resonance of ^{117}Sn with $J = 1$ and $F = 0$ are considered, the coefficients a_0, a_1, and a_3 terms can be written as

$$
\begin{aligned}
a_0 &= |V_1(E_\mathrm{n})|^2 + |V_2(E_\mathrm{n})|^2\\
&= B_{\mathrm{s},f}|V'_1(E_\mathrm{n})|^2 + B_{\mathrm{p},f}|V'_2(E_\mathrm{n})|^2\\
&= B_{\mathrm{s},f}\ a'_{0,\mathrm{s}} + B_{\mathrm{p},f}\ a'_{0,\mathrm{p}}, &\text{(3.17a)}\\
a_1 &= \mathrm{Re}(V_1(E_\mathrm{n})V_2^*(E_\mathrm{n}))(-2x+\sqrt{2}y)\\
&= \sqrt{B_{\mathrm{s},f}B_{\mathrm{p},f}}\ \mathrm{Re}(V'_1(E_\mathrm{n})V'^*_2(E_\mathrm{n}))(-2x+\sqrt{2}y)\\
&= \sqrt{B_{\mathrm{s},f}B_{\mathrm{p},f}}\ a'_1, &\text{(3.17b)}\\
a_3 &= -3|V_2(E_\mathrm{n})|^2\left(\frac{xy}{\sqrt{2}}+\frac{y^2}{4}\right)\\
&= -3B_{\mathrm{p},f}|V'_2(E_\mathrm{n})|^2\left(\frac{xy}{\sqrt{2}}+\frac{y^2}{4}\right)\\
&= B_{\mathrm{p},f}\ a'_3, &\text{(3.17c)}
\end{aligned}
$$

where $a'_{0,\mathrm{s}}$ and $a'_{0,\mathrm{p}}$ are the angular-independent differential cross sections calculated by the amplitudes without transition ratios for an s-wave and a p-wave resonance. The coefficients a'_1 and a'_3 are for the angular correlation terms calculated by the amplitudes without transition ratios. Figure 3.2 shows the neutron energy dependence of each term calculated by Eqs. (3.17a), (3.17b), and (3.17c). These calculation results indicate that the a_1 terms and the a_3 terms are odd and even functions centered on the p-wave resonance energy E_p, respectively.

The observable differential cross section for unpolarized neutrons depends on both the polar angle θ_γ and the mixing angle ϕ. Figure 3.3 shows the calculation results of observable differential cross section around the p-wave resonance in various cases. These calculation results indicate that the mixing angle ϕ can

be determined by measuring the shape of the p-wave resonance with a certain transition at several polar angles.

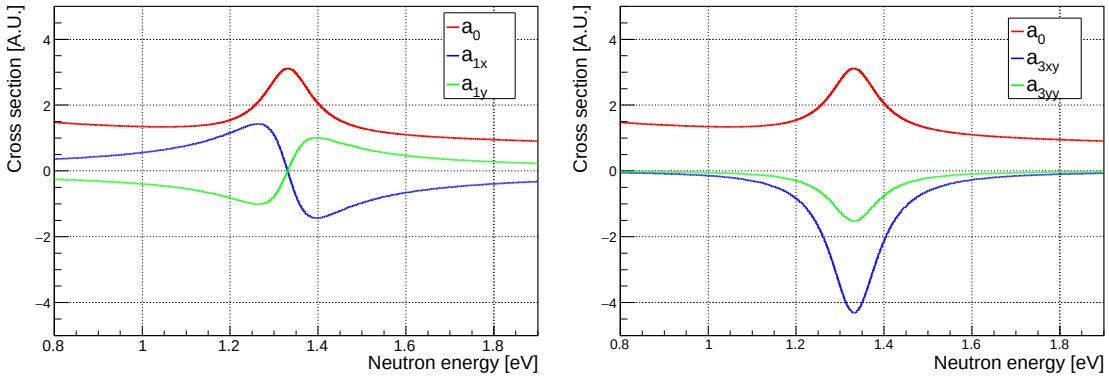

Figure 3.2: Neutron energy dependencies of angular-correlated terms in (n,γ) reaction.

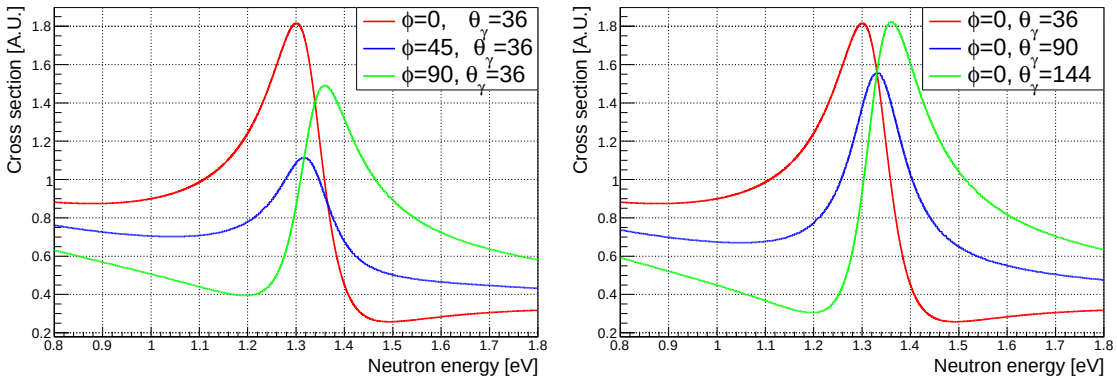

Figure 3.3: Variables ϕ and θ_γ dependencies of the p-wave resonance.

To evaluate the angular dependence of the peak shape of the p-wave resonance, the asymmetry A_{LH} is defined as

$$A_{\mathrm{LH}} \equiv \frac{I_{\mathrm{L}} - I_{\mathrm{H}}}{I_{\mathrm{L}} + I_{\mathrm{H}}}, \tag{3.18}$$

where I_{L} and I_{H} are the integrated values in lower- and higher-energy regions,

respectively. They are defined as

$$
\begin{aligned}
I_{\mathrm{L}} &\equiv \int_{E_{\mathrm{p}}-2\Gamma_{\mathrm{p}}}^{E_{\mathrm{p}}} dE_{\mathrm{n}} \frac{d\sigma}{d\Omega} \\
&= \frac{1}{2}\int_{E_{\mathrm{p}}-2\Gamma_{\mathrm{p}}}^{E_{\mathrm{p}}} dE_{\mathrm{n}} \left(a_0 + a_1 \cos\theta_\gamma + a_3 \left(\cos^2\theta_\gamma - \frac{1}{3} \right) \right) \\
&= I_{\mathrm{L},a_0} + I_{\mathrm{L},a_1} \cos\theta_\gamma + I_{\mathrm{L},a_3} \left(\cos^2\theta_\gamma - \frac{1}{3} \right), \qquad (3.19a) \\
I_{\mathrm{H}} &\equiv \int_{E_{\mathrm{p}}}^{E_{\mathrm{p}}+2\Gamma_{\mathrm{p}}} dE_{\mathrm{n}} \frac{d\sigma}{d\Omega} \\
&= \frac{1}{2}\int_{E_{\mathrm{p}}}^{E_{\mathrm{p}}+2\Gamma_{\mathrm{p}}} dE_{\mathrm{n}} \left(a_0 + a_1 \cos\theta_\gamma + a_3 \left(\cos^2\theta_\gamma - \frac{1}{3} \right) \right) \\
&= I_{\mathrm{H},a_0} + I_{\mathrm{H},a_1} \cos\theta_\gamma + I_{\mathrm{H},a_3} \left(\cos^2\theta_\gamma - \frac{1}{3} \right), \qquad (3.19b)
\end{aligned}
$$

where

$$
I_{\mathrm{L},a_i} = \frac{1}{2}\int_{E_{\mathrm{p}}-2\Gamma_{\mathrm{p}}}^{E_{\mathrm{p}}} a_i \, dE_{\mathrm{n}}, \qquad (3.20a)
$$

$$
I_{\mathrm{H},a_i} = \frac{1}{2}\int_{E_{\mathrm{p}}}^{E_{\mathrm{p}}+2\Gamma_{\mathrm{p}}} a_i \, dE_{\mathrm{n}}. \qquad (3.20b)
$$

Here, the sum and the difference between I_{L,a_i} and I_{H,a_i} are described as I_{LH,a_i} and $\Delta I_{\mathrm{LH},a_i}$, respectively. Then, the asymmetry A_{LH} can be described using a relative transition ratio $B_{\mathrm{sp},f} = B_{\mathrm{s},f}/B_{\mathrm{p},f}$ as

$$
\begin{aligned}
A_{\mathrm{LH}} &= \frac{\Delta I_{\mathrm{LH},a_0} + \Delta I_{\mathrm{LH},a_1}\cos\theta_\gamma + \Delta I_{\mathrm{LH},a_3}\left(\cos^2\theta_\gamma - \frac{1}{3}\right)}{I_{\mathrm{LH},a_0} + I_{\mathrm{LH},a_1}\cos\theta_\gamma + I_{\mathrm{LH},a_3}\left(\cos^2\theta_\gamma - \frac{1}{3}\right)} \\
&= \frac{\Delta I_{\mathrm{LH},a_{0,\mathrm{s}}} + \Delta I_{\mathrm{LH},a_1}\cos\theta_\gamma}{I_{\mathrm{LH},a_0} + I_{\mathrm{LH},a_3}\left(\cos^2\theta_\gamma - \frac{1}{3}\right)} \\
&= \frac{B_{\mathrm{s},f}\Delta I_{\mathrm{LH},a'_{0,\mathrm{s}}} + \sqrt{B_{\mathrm{s},f}B_{\mathrm{p},f}}\Delta I_{\mathrm{LH},a'_1}\cos\theta_\gamma}{B_{\mathrm{s},f} I_{\mathrm{LH},a'_{0,\mathrm{s}}} + B_{\mathrm{p},f} I_{\mathrm{LH},a'_{0,\mathrm{p}}} + B_{\mathrm{p},f} I_{\mathrm{LH},a'_3}\left(\cos^2\theta_\gamma - \frac{1}{3}\right)} \\
&= \frac{B_{\mathrm{sp},f}\Delta I_{\mathrm{LH},a'_{0,\mathrm{s}}} + \sqrt{B_{\mathrm{sp},f}}\Delta I_{\mathrm{LH},a'_1}\cos\theta_\gamma}{B_{\mathrm{sp},f} I_{\mathrm{LH},a'_{0,\mathrm{s}}} + I_{\mathrm{LH},a'_{0,\mathrm{p}}} + I_{\mathrm{LH},a'_3}\left(\cos^2\theta_\gamma - \frac{1}{3}\right)}. \qquad (3.21)
\end{aligned}
$$

When the a_3 term is small enough compared to the a_0 term, Eq. (3.21) can be written as

$$
A_{\mathrm{LH}} = \frac{B_{\mathrm{sp},f}\Delta I_{\mathrm{LH},a'_{0,\mathrm{s}}} + \sqrt{B_{\mathrm{sp},f}}\Delta I_{\mathrm{LH},a'_1}\cos\theta_\gamma}{B_{\mathrm{sp},f} I_{\mathrm{LH},a'_{0,\mathrm{s}}} + I_{\mathrm{LH},a'_{0,\mathrm{p}}}} \ . \qquad (3.22)
$$

Thus, the relative branching ratio $B_{\mathrm{sp},f}$ need to be measured to calculate the theoretical asymmetry value. When the a_3 term is large, the differential cross section around the p-wave resonance has angular dependence as shown in Fig. 3.4.

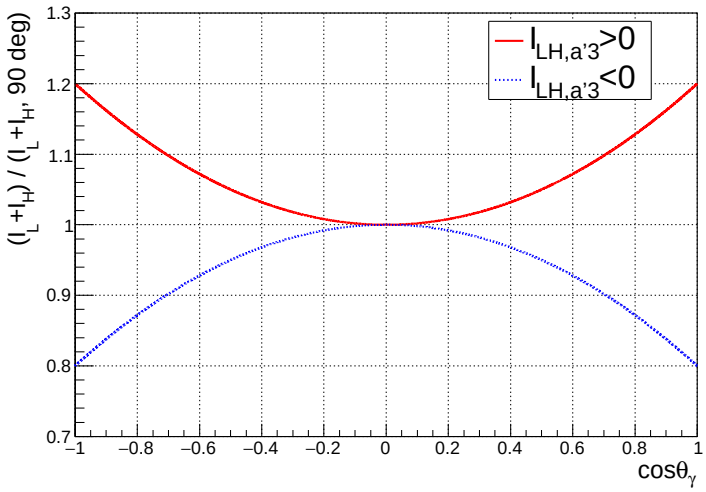

Figure 3.4: Angular dependence of differential cross section caused by the a_3 term. This is normalized to be unity at $\cos\theta_\gamma = 90°$.

3.3 Previous study for determining the ϕ value

In 1985, the angular correlation terms in (n,γ) reactions were measured using polarized and unpolarized neutron beams by V. P. Alfimenkov *et al.* [51,52]. They assumed the differential cross section as

$$\sigma(\theta,\xi,E_\mathrm{n}) = a_0 + a_1\cos\theta + a_2 f_\mathrm{n}\sin\theta\cos\xi + a_3\left(\cos^2\theta - \frac{1}{3}\right), \tag{3.23}$$

where f_n is the polarization of the neutron beam, θ is the angle between the directions of the neutron beam and γ rays, and ξ is the angle between the directions of neutron polarization and the γ-ray emission. The angular-indepndent term a_0 can be written as $a_0 = (\sigma_\mathrm{s}(E_\mathrm{n}) + \sigma_\mathrm{p}(E_\mathrm{n}))/4\pi$, where $\sigma_{\mathrm{s(p)}}(E_\mathrm{n})$ is the cross section of s(p)-wave capture integrated with the solid angle for the single transition of 9327 keV γ-ray emission. Three types of asymmetries, left-right asymmetry $\epsilon^{L.R.}$, forward-backward asymmetry $\epsilon^{F.B.}$, and angular asymmetry ϵ^{a} were measured and can be described as

$$\begin{aligned}\epsilon^{L.R.}(E_\mathrm{n}) &= \frac{\sigma(90°,0°,E_\mathrm{n}) - \sigma(90°,180°,E_\mathrm{n})}{\sigma(90°,0°,E_\mathrm{n}) + \sigma(90°,180°,E_\mathrm{n})} \\ &= f_\mathrm{n}\frac{a_2}{a_0 - a_3/3},\end{aligned} \tag{3.24}$$

$$\begin{aligned}\epsilon^{F.B.}(E_\mathrm{n},\theta=45°) &= \frac{\sigma(\theta=45°,E_\mathrm{n}) - \sigma(\theta=135°,E_\mathrm{n})}{\sigma(\theta=45°,E_\mathrm{n}) + \sigma(\theta=135°,E_\mathrm{n})} \\ &= \frac{1}{\sqrt{2}}\frac{a_1}{a_0 + a_3/6},\end{aligned} \tag{3.25}$$

$$\begin{aligned}\epsilon^a(\theta = 45^\circ) &= \frac{2(\sigma(90^\circ, E_\mathrm{p}) - \sigma_\mathrm{s}(E_\mathrm{p})/4\pi))}{\sigma(\theta = 45^\circ, E_\mathrm{p}) + \sigma(\theta = 135^\circ, E_\mathrm{p}) - \sigma_\mathrm{s}(E_\mathrm{p})/2\pi} \\ &= \frac{a_0(E_\mathrm{p}) - a_3/3 - \sigma_\mathrm{s}(E_\mathrm{p})/4\pi}{a_0(E_\mathrm{p}) + a_3/6 - \sigma_\mathrm{s}(E_\mathrm{p})/4\pi}. \end{aligned} \tag{3.26}$$

All asymmetries were measured using the time-of-flight (TOF) method at the IBR-30 pulsed reactor. The TOF method is explained in the following section. The γ-ray detectors were NaI(Tl) crystals with a diameter of 200 mm and thickness of 200 mm. The threshold of registration of γ rays was set at 8.5 MeV to suppress γ rays from other transitions except for 9.3 MeV. The background events were measured when the neutron beam was blocked by a boron filter. The target was a metallic tin with enrichment of 90% of ^{117}Sn isotope. The weight of the target was between 80 and 400 g, and its area is 20-60 cm^2. In the measurement of $\epsilon^{L.R.}$, the neutron beam was polarized by passing through a polarized proton target. However, they did not measure the polarization of the neutron beam, and they assumed $f_\mathrm{n} = 1$. Figure 3.5 shows solutions of the mixing angle ϕ which were obtained from the intersection points of the unit circle and three asymmetries. There is no common solution that three lines intersect at a single point on the unit circle. They insist that there may be a common solution at $x \simeq 0.2$ if the sign of the a_1 term is opposite.

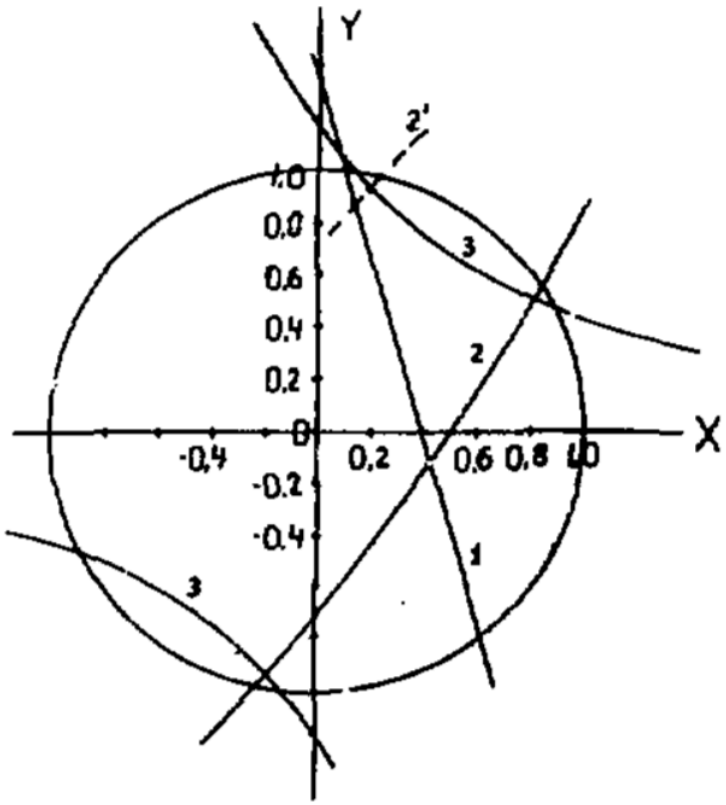

Figure 3.5: Previous result by Alfimenkov *et al.* [52]. Line 1, 2, and 3 correspond to the left-right asymmetry $\epsilon^{\mathrm{L.R.}}$, the forward-backward asymmetry $\epsilon^{F.B.}$, and the angular asymmetry ϵ^a, respectively.

There are some obscure points in this previous study. First, the result of $\epsilon^{L.R.}$ can be changed by measuring the polarization of the neutron beam. The resonance width can be wider than the true width due to the Doppler broadening effect and energy resolution of the neutron beam, which is described in Chapter 6. These effects must be considered in the analysis because they can sufficiently change the value of asymmetries. In this study, the energy resolution of the neutron beam was not taken into account, while the Doppler broadening effect is not mentioned. Moreover, the error of each line in Fig. 3.5 is not drawn.

The measurement in this study was performed with a pulsed neutron beam. The γ-ray detectors were germanium crystals with the energy resolution much better than that of NaI crystals. The number of γ-ray detection angles is larger than that in the previous study, so that the angular dependence of the p-wave resonance can be studied further in detail. The Doppler broadening effect and energy resolution of neutron beam were considered in this study. Therefore, it is considered that the result of this study is more reliable compared to the previous study. Table 3.1 summarizes the difference between this study and the previous study.

Table 3.1: Comparison with previous study.

	Previous study	This study
Experimental facility	Reactor (IBR-30)	J-PARC MLF
Neutron flight length	35 m or 58 m	21.5 m
Nuclear target	90% ^{117}Sn	$^{\mathrm{nat}}$Sn
γ-ray detector	NaI crystals	Ge crystals
Number of γ-ray detection angle	3 angles	7 angles
Doppler broadening effect	Not mentioned	Concerned
Energy resolution of neutron beam	Not concerned	Concerned

Chapter 4

Experimental setup

In this chapter, a facility and an experimental setup established to measure the angular dependence of γ rays from neutron-induced compound states are explained. A high-intensity neutron beam and γ-ray detectors with a high energy resolution are required for this measurement.

4.1 J-PARC facility

Japan Proton Accelerator Research Complex (J-PARC) is a high-intensity proton accelerator facility in Tokai Village, Ibaraki Prefecture, Japan. This joint project between the High Energy Accelerator Research Organization (KEK) and the Japan Atomic Energy Agency (JAEA) aims to promote a wide variety of experiments using various secondary beams including neutrons, muons, neutrinos, and kaons. Figure 4.1 shows a bird's-eye view of J-PARC. The pulsed proton beam is accelerated to 400 MeV by a linear accelerator (LINAC). It is transported to Rapid Cycle Synchrotron (RCS), and further reaccelerated to 3 GeV. A part of the proton beam bunches with a repetition rate of 25 Hz is transported to Main Ring (MR), and the remaining are injected into the targets at Materials and Life science experimental Facility (MLF).

The neutrons are generated in a liquid mercury target, which is located at the center of MLF, through the nuclear spallation process caused by injecting a 3 GeV proton beam. The high-energy neutrons are cooled in a liquid-hydrogen moderator at 20 K and 1.5 MPa by colliding with hydrogen molecules, and guided to 23 neutron beam ports in MLF as shown in Fig. 4.2. The neutron beam energy ranges mainly from cold to epithermal energies. The three types of moderators are: coupled, decoupled, and poisoned. The characteristics of these moderators are summarized in Table 4.1. The coupled moderator provides the most intense neutron beam among the three types, and this type was used for the experiment in this study.

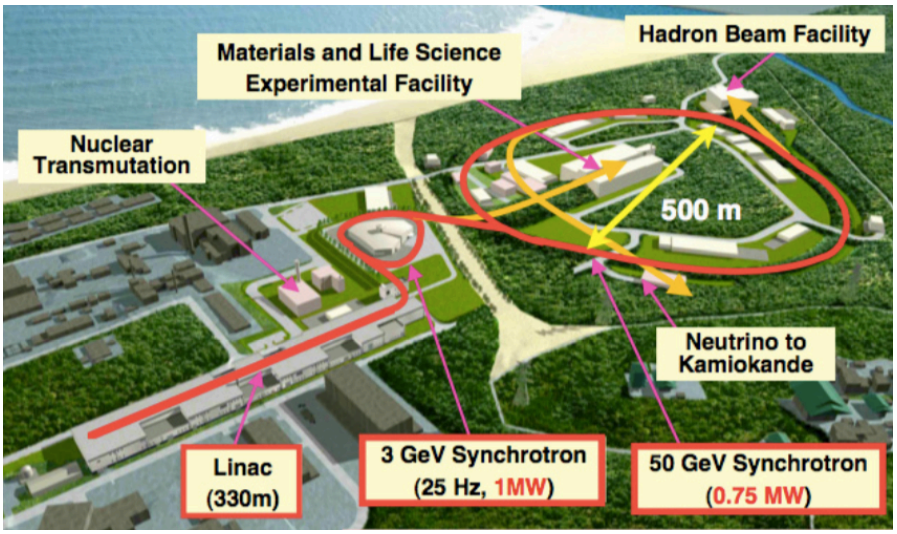

Figure 4.1: Bird's eye view of J-PARC [53].

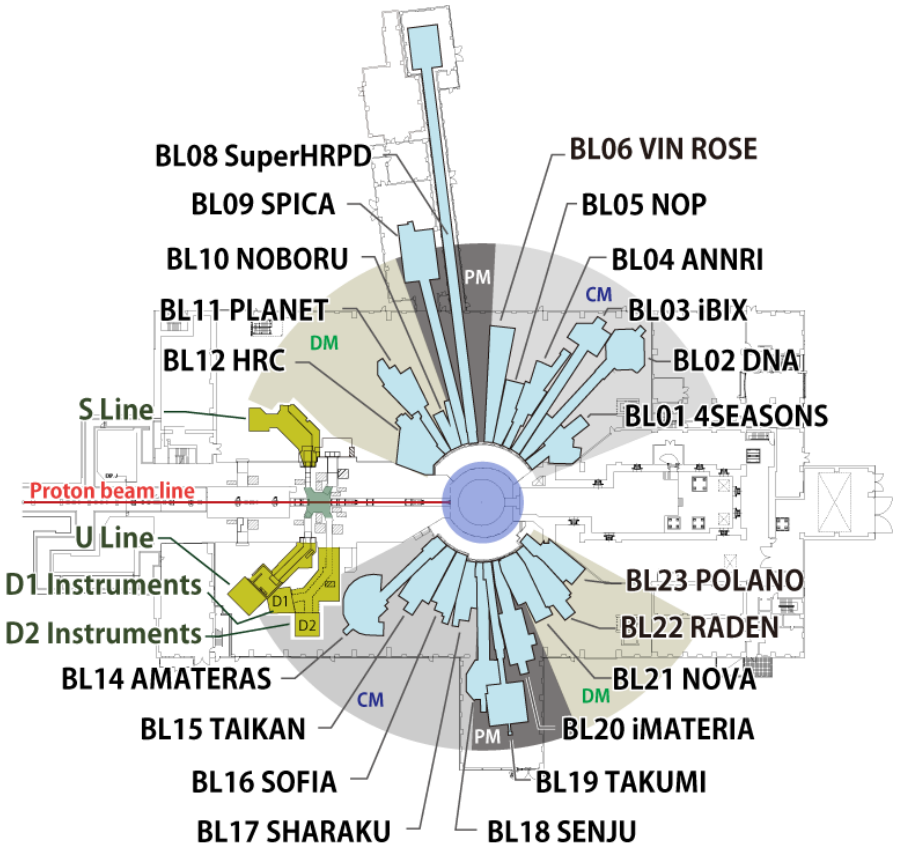

Figure 4.2: Beamlines in MLF [54].

Table 4.1: Characteristics of moderators in MLF [55].

Moderator type	Number of beam ports	Time-integrated thermal neutron flux [n/s · cm^2]	Peak neutron flux at 10 meV [n/eV · s · cm^2]	Pulse width in FWHM at 10 meV [μs]
Coupled	11	4.6×10^8	6.0×10^{12}	92
Decoupled	6	0.95×10^8	3.0×10^{12}	33
Poisoned (Thicker side)	3	0.65×10^8	2.4×10^{12}	22
Poisoned (Thinner side)	3	0.38×10^8	1.4×10^{12}	12

4.2 Beamline 04 ANNRI

4.2.1 Beamline setup

A schematic view of Accurate Neutron-Nucleus Reaction measurement Instrument (ANNRI) installed in beamline 04 (BL04) of MLF is shown in Fig. 4.3. The z-axis is defined as the neutron beam direction, the y-axis is the vertical upward axis, and the x-axis is perpendicular to them.

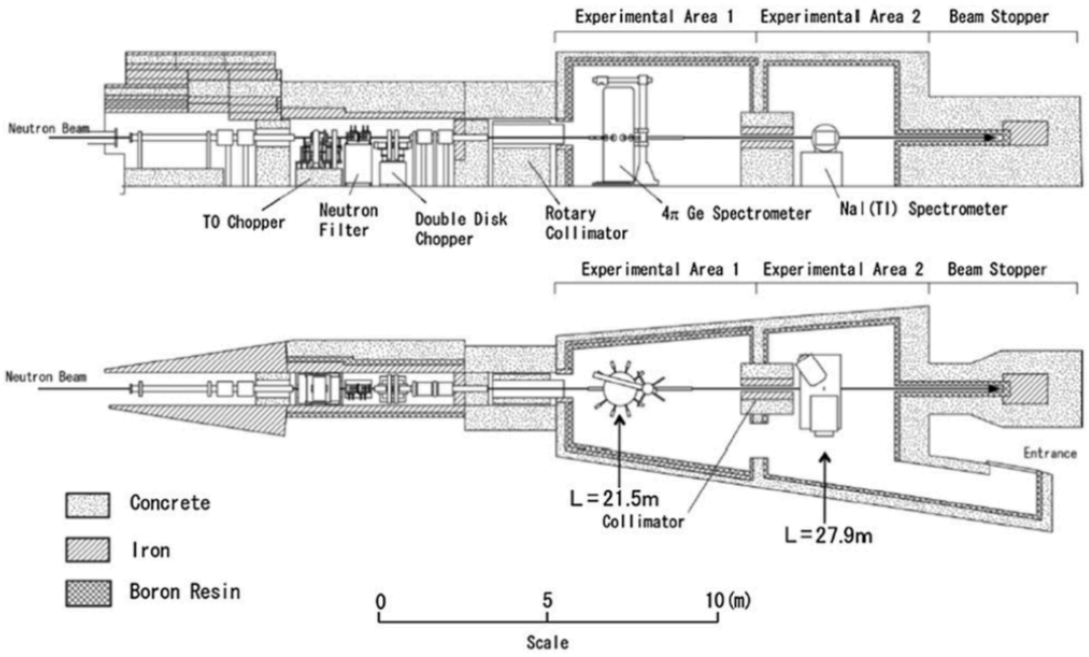

Figure 4.3: Side view (upper) and top view (bottom) of ANNRI installed at the beamline 04 [56].

The neutron beam from the moderator passes through a T_0 chopper, neutron filters, double disk chopper, and a rotary collimator, typically used for the adjustment of the experimental conditions. The neutron beam is stopped by a beam

stopper made of iron. The materials of the neutron filters can be selected from manganese, cobalt, aluminum, silver, indium, lead, and cadmium. Particularly, there are six lead filters: two with thicknesses of 12.5 mm and 25 mm, and four with a thickness of 50 mm each. The total thickness can be adjusted by selecting these lead filters. These neutron filters are used to suppress the neutron flux in uninterested energy regions because the energy dependence of the neutron absorption cross section is different in each nucleus. The lead filters can also play a role to suppress the γ-ray background from the upstream. In our measurements, only the lead filters with a thickness of 37.5 mm in total were used. The double disk chopper consists of two semicircular plates whose surfaces are coated by 95 wt% ^{10}B-enriched boron carbide. These two plates rotate synchronously with the proton injection at 25 Hz, so that the neutron beam in any energy region is shielded by adjusting a relative phase between the two plates. The double disk chopper is used mainly to suppress the slow neutrons (less than 3 meV) to avoid the frame overlap that these slow neutrons from a given pulse overlap with fast neutrons from the subsequent pulses. The collimators consist of an upper-stream and a down-stream collimator, and are used for the adjustment of the intensity and the size of the neutron beam. The down-stream collimator is called a rotary collimator, and its hole size can be selected from four sizes of 6 mm, 7 mm, 15 mm, and 22 mm. A germanium detector assembly is installed at ANNRI which is described in Sec. 4.3. The nuclear target is placed at the center of the detector assembly and the distance from the moderator surface to the target is 21.5 m.

4.2.2 Energy resolution of the neutron beam

The information of neutron energy needs to analyze the angular dependence of the p-wave resonance shape. The neutron energy can be calculated from the TOF method which uses the detection time of γ rays. The emission time of prompt γ rays from neutron capture is about 10^{-14} s. This is sufficiently short and negligible compared to the flight time of neutrons from the moderator surface to the target. The neutron energy in measured data ($E_{\rm n}^{\rm m}$) was therefore calculated as

$$E_{\rm n}^{\rm m} = \frac{1}{2} m_{\rm n} \left(\frac{L}{t^{\rm m}} \right)^2 , \tag{4.1}$$

where $m_{\rm n}$, L, and $t^{\rm m}$ are the neutron mass, the flight length of neutrons from the moderator surface to the target, and the flight time of neutrons which travel the length L, respectively. The energy resolution due to the time structure of the pulsed neutron beam must be considered in analysis of the experimental data. There are two factors that cause time structures of the pulsed neutron beam. One is the moderation process of neutrons, and the other is the time structure of the incident proton beam. In thermal and cold energy regions, the time structure can be negligible. However, it cannot be ignored in the epithermal region which is used for the measurement of neutron resonances.

Some functions describing the pulse structure of neutron beams were proposed. Typically, Ikeda-Carpenter function [57], Cole-Windsor function [58], Gunsing

function [59], and Gauss function [60, 61] are used. The pulse structure of the neutron beam at BL04 has already been studied by K. Kino *et al.* [62]. They adopted the Ikeda-Carpenter function ψ which can be described as a function of neutron energy $E_{\rm n}$ and the arrival time of neutrons from the primary proton beam injection t using the following equations:

$$\psi(E_{\rm n}, t) = \frac{\alpha C}{2}\left\{(1-R)(\alpha t)^2 e^{-\alpha t} + 2R\frac{\alpha^2\beta}{(\alpha-\beta)^3} \times \left[e^{-\beta t} - e^{-\alpha t}\left(1 + (\alpha-\beta)t + \frac{1}{2}(\alpha-\beta)^2 t^2\right)\right]\right\}, \tag{4.2}$$

where parameters α, β, and R depend on $E_{\rm n}$, and C is an $E_{\rm n}$-independent scaling factor for normalization. Time was modified as $t - t_0$, where t_0 is the flight time of neutrons after emission from the moderator. Therefore, the time difference $t - t_0$ means the moderation and storage time inside the moderator. A simulation of the neutron source using a Monte-Carlo simulation was performed to obtain the time structure of the neutron beam. Figure 4.4 shows the examples of the simulated time structure of the neutron beam and the fitting results via Eq. (4.2). The neutron energy dependences of the fitting parameters t_0, α, β, and R in the Ikeda-Carpenter function were obtained by applying polynomial functions as shown in Fig. 4.5. The fitting results are as follows;

$$\begin{aligned}
\log_{10} t_0 &= 0.124 - 0.475y + (2.42\times10^{-3})y^2 + (1.59\times10^{-3})y^3 \\
\log_{10} \alpha &= \begin{cases} -0.0719 + 0.478y + (1.59\times10^{-3})y^2 - (2.65\times10^{-3})y^3 & (y < 8.0, y \geq -1.5) \\ 6.51 + 8.98y + 3.45y^2 + 4.66y^3 & (y < -1.5) \end{cases} \\
\log_{10} \beta &= \begin{cases} -1.05 + 0.581y - 0.0406y^2 + (3.57\times10^{-3})y^3 & (y < 8.0, y \geq -1.5) \\ 1.81 + 4.17y + 2.27y^2 + 3.24y^3 & (y < -1.5) \end{cases} \\
\log_{10} R &= \begin{cases} -1.05 - 0.0911y + 0.0959y^2 - 0.0108y^3 & (y < 8.0, y \geq -0.8) \\ -4.39 - 8.25y - 6.61y^2 - 2.38y^3 - 0.311y^4 & (y < -0.8) \end{cases} \\
y &= \log_{10} E_{\rm n}.
\end{aligned}$$

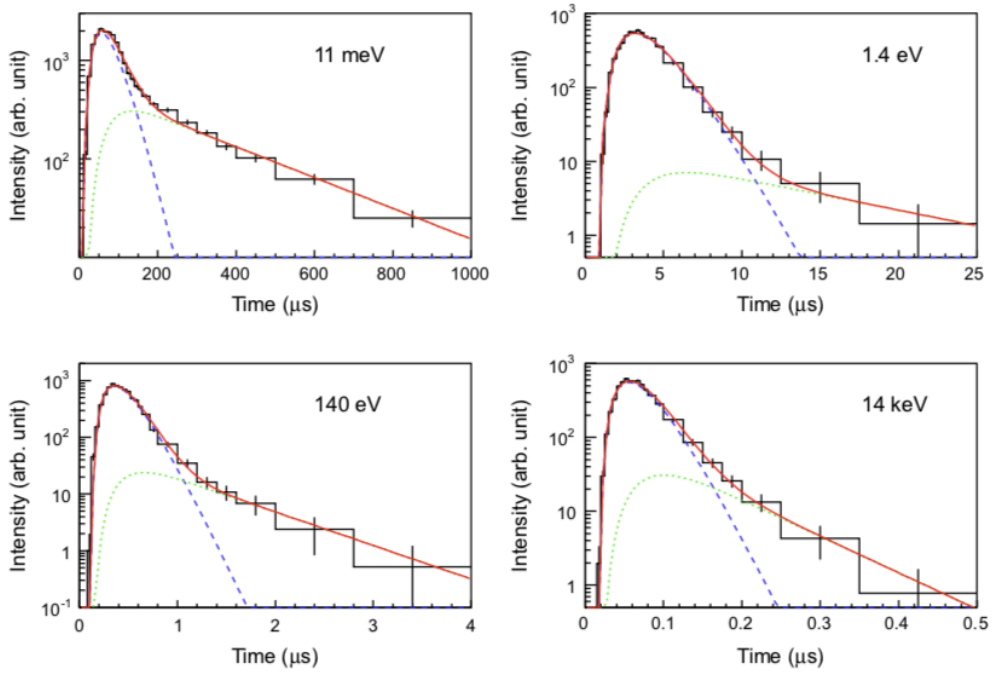

Figure 4.4: Examples of the simulated time structure of the neutron beam and fitting results [62].

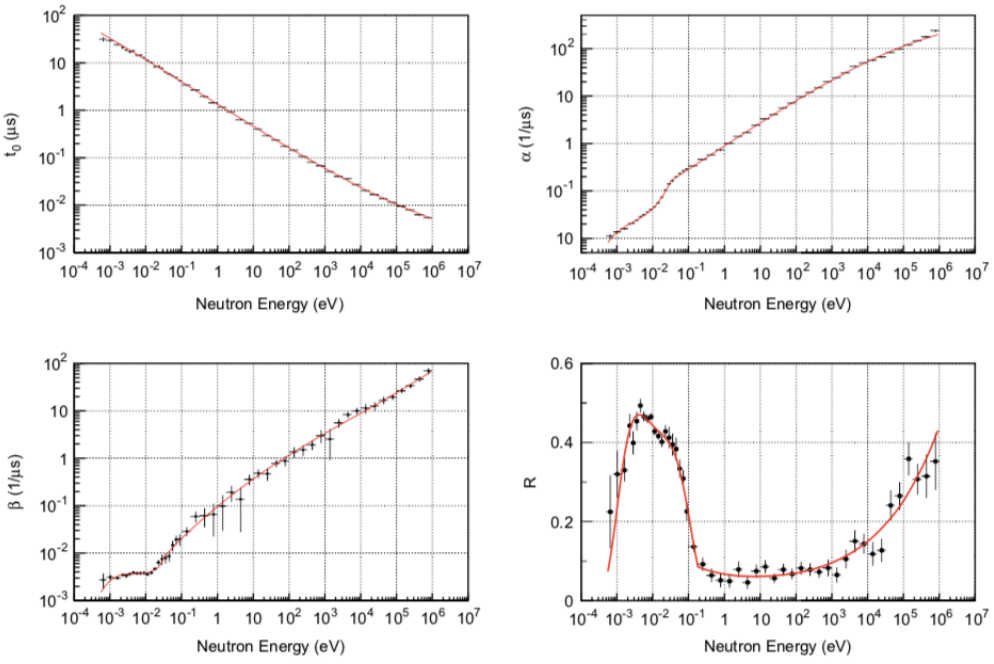

Figure 4.5: Energy dependence of parameters in Ikeda-Carpenter function [62].

There are two types of the time structures of the incident proton beam at J-PARC. One is a single-bunch mode in which the pulsed protons consist of a bunch of about 100 ns. The other is a double-bunch mode in which the time

interval between the two proton bunches is about 600 ns. The proton beam is normally delivered in the double-bunch mode. The measurements in this study were performed with both the single- and double-bunch modes. Figure 4.6 shows the two-dimensional energy-time plots of the time and energy of neutrons for both modes. In the double-bunch mode, the time structure splits into two peaks above about 10 eV. This phenomenon makes the energy resolution worse.

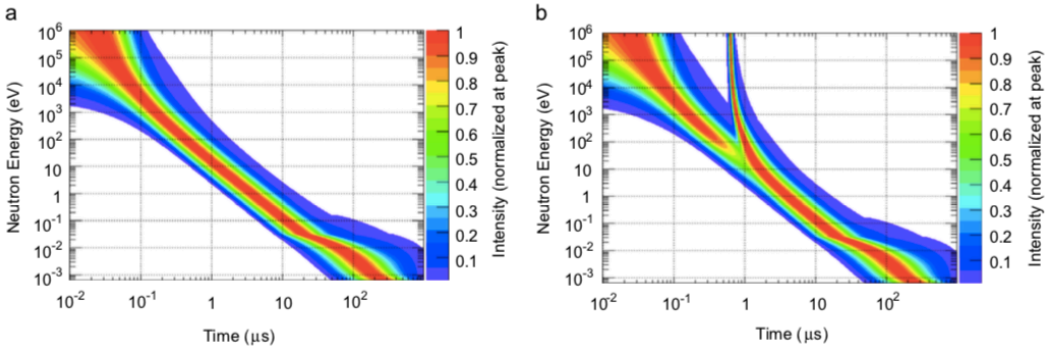

Figure 4.6: Two-dimensional plots of the time and energy of neutrons at the moderator surface. Left (a) and right (b) are for the single- and double-bunch modes, respectively [62].

The neutron energy resolution at the target position was calculated using the width of the time structure. In the case where the time structure splits into two peaks, the time width was defined as the time between the leading edge of the first peak and the trailing edge of the second peak. Figure 4.7 shows the energy resolutions of the neutron beam for both modes and the effect of the double bunch can be seen above about 5 eV as a function of neutron energy.

The time structures of the neutron beam were measured in the thermal neutron energy region using a mica sample with dimensions of 50×50 mm^2 and a thickness of 5 mm. Mica is a silicate mineral and has a layered crystal structure with an interval of 10.4 Å. The time structure of the neutron beam was obtained by measuring Bragg's peaks. When the neutron beam goes through a crystal, the neutrons which adhere to Bragg's law are scattered. Since scattered neutrons have that monochromatic energy, the diffraction peaks in the TOF spectra reflect the time structure of the neutron beam. In the epithermal energy region, the time structure was obtained from the resonances of the neutron capture reaction for ^{181}Ta. A ^{181}Ta foil with an area of 100×100 mm^2 and a thickness of 0.1 or 0.01 mm was used. The time structure of the neutron beam can be extracted from the measured TOF spectra for well-known neutron capture resonances. Figure 4.8 shows the neutron energy dependence of the FWHM of the time structure for the single-bunch mode in simulation and measurements. The simulation reproduces the measurements.

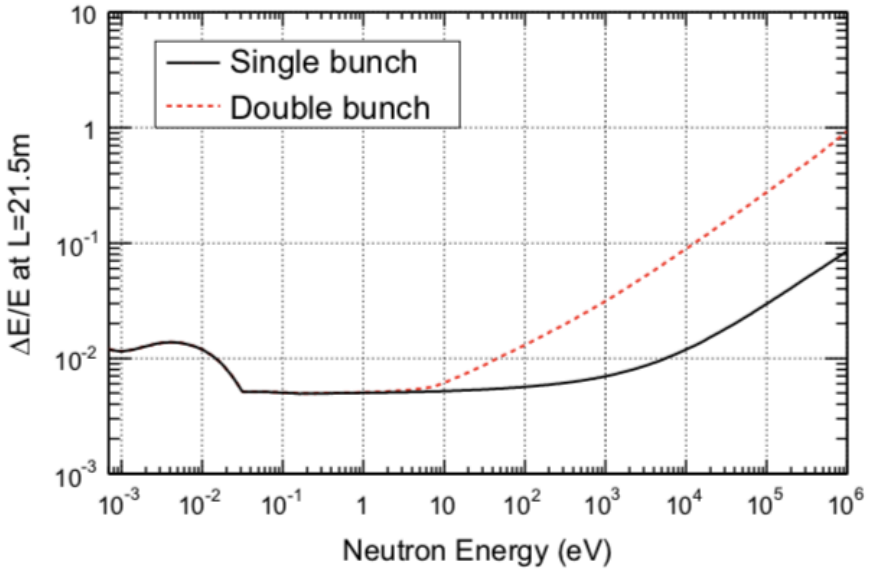

Figure 4.7: Energy resolution of the neutron beam at ANNRI based on simulation [62].

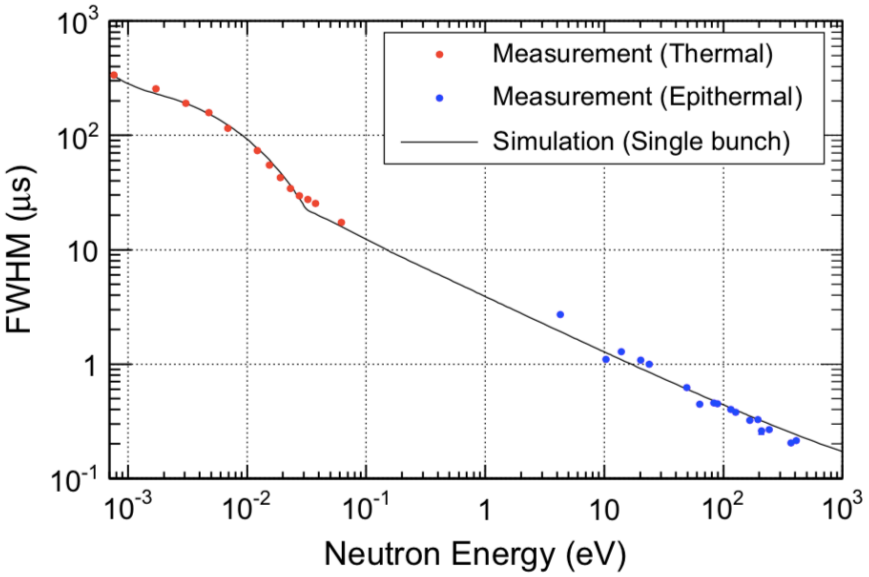

Figure 4.8: Comparison of energy resolution between simulation and measurements for single-bunch mode [62].

4.3 Germanium detector assembly

In this section, the geometry of a germanium detector assembly used in this study is explained. In addition, a response function is calculated using a Monte-Carlo simulation, which is also explained.

4.3.1 Geometry of germanium detector assembly

The germanium spectrometer at ANNRI is a γ-ray detector assembly which has a high resolution and a large solid angle. It was originally developed to measure neutron-absorption cross sections of minor actinides and long-lived-fission products with the TOF method. The configuration of the germanium detector assembly is shown in Fig. 4.9. The polar and azimuthal angles in the spherical coordinates are denoted as θ and φ, respectively.

The assembly consists of two types of detector units; cluster-type and coaxial-type. The shapes of cluster-type and coaxial-type crystals are shown in Fig. 4.10. The front-end of the cluster-type crystal has a hexagonal shape, and the back-end has a hole for the insertion of the electrode. The cluster-type unit has seven germanium crystals as shown in Fig. 4.11. The central crystal is directed toward the center of the target position, while the surrounding six crystals are directed farther beyond the target position. Therefore, they have different solid angles of $0.010 \times 4\pi$ sr (central) and $0.0091 \times 4\pi$ sr (one of the surrounding six crystals), respectively. There are two cluster-type detector units which are located above and below the target. The central detector of the upper (lower) cluster-type unit is denoted by d1 (d8), and the other surrounding six detectors are denoted by d2–d7 (d9–d14). The germanium crystals are protected by neutron shields against damages stemmed from scattered neutrons. Neutron shield-1 and shield-3 are plates made by sintering LiH powder with a thickness of 22.3 mm and 17.3 mm, respectively. Neutron shield-2 is a plate made by sintering LiF powder with a thickness of 5 mm. The side and back of the cluster-type units are surrounded by bismuth germanate (BGO) scintillators which can veto Compton scattering events and cosmic rays.

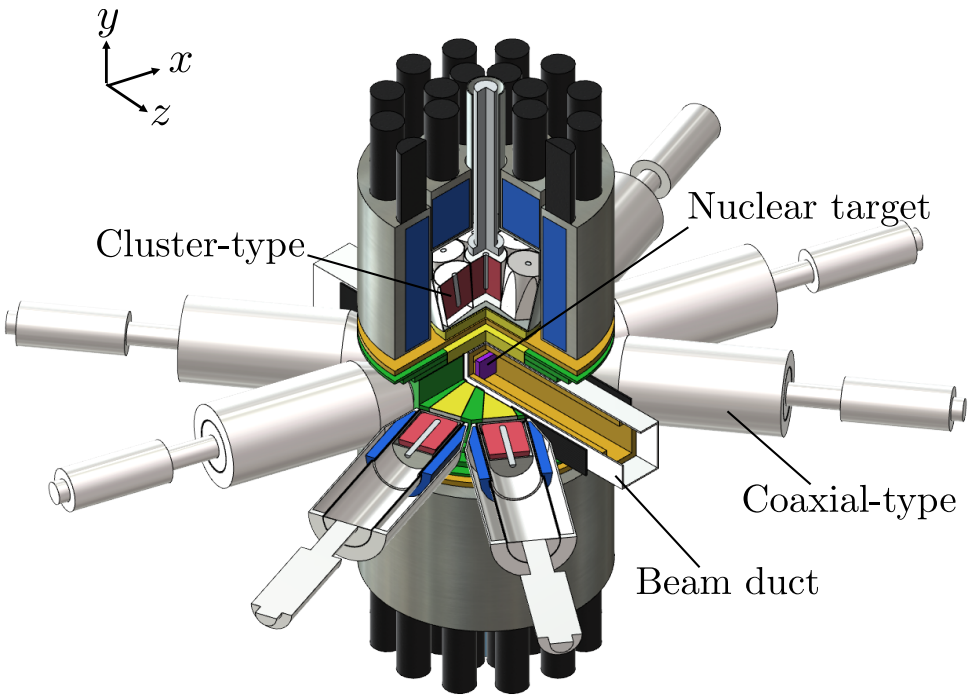

Figure 4.9: Configuration of the germanium detector assembly.

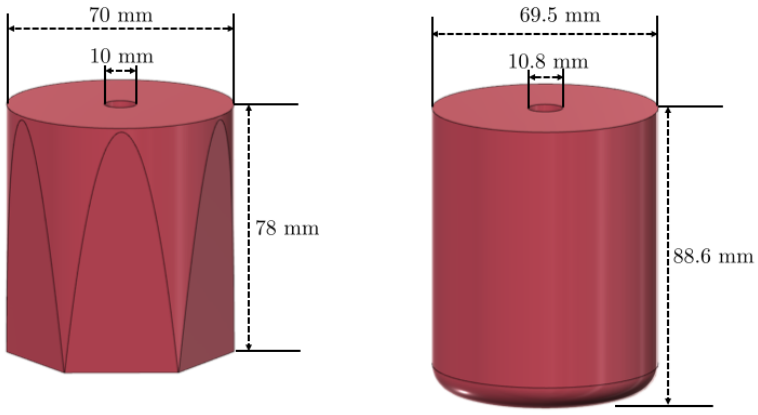

Figure 4.10: Crystal shapes of cluster-type (left) and coaxial-type detector (right).

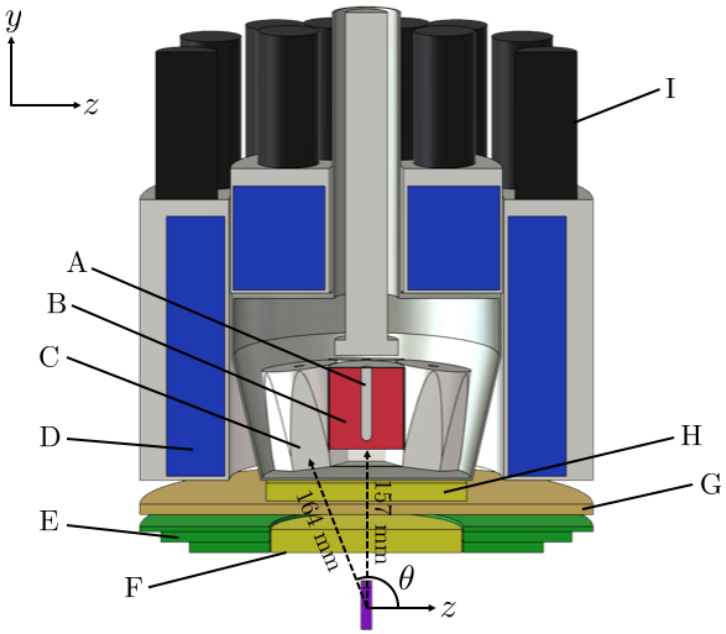

Figure 4.11: Cut view of the upper cluster-type detector unit. (A) Electrode, (B) Germanium crystal, (C) Aluminum case, (D) BGO crystal, (E) γ-ray shield (Pb collimator), (F) Neutron shield-1 (22.3 mm LiH), (G) Neutron shield-2 (5 mm LiF), (H) Neutron shield-3 (17.3 mm LiH), and (I) Photomultiplier tube for BGO crystal.

Eight coaxial-type detectors are assembled as shown in Fig. 4.12. The detectors are denoted by d15 - d22. The front-end of the coaxial-type crystal is a circular, and its edge is rounded as shown in Fig. 4.10. This rounded shape prevents the crystal from destroying and improves the uniformity of the electric field in the crystal. The back-end has a hole for the insertion of the electrode. Notably, the germanium crystal of d16 is smaller than that of the other crystals of coaxial-type detectors. All coaxial-type crystals are directed toward the center of the target position. Therefore, except for d16, they all have the same solid angle of $0.0072 \times 4\pi$ sr. The solid angle of d16 is $0.0048 \times 4\pi$ sr. Each coaxial-type crystal is surrounded by a BGO scintillator as shown in Fig. 4.13. A conical-shape γ-ray collimator made by lead is located between each coaxial-type detector and the target position. These collimator holes are filled with LiF powder which is encapsulated in aluminum cases for shielding the scattered neutrons. Table 4.2 summarizes the setting angle of each germanium detector. The germanium crystals were kept at a temperature of 77 K during the measurements. The cluster-type and coaxial-type detectors are cooled by liquid nitrogen and refrigerators X-COOLER II of ORTEC, respectively. In the measurements, d17 and d20 were not used because they did not cool sufficiently.

The beam duct consists of two layers. The outer layer is made from 3 mm-thick aluminum with cross-sectional dimensions of 86 mm $\times$ 96 mm. The inner layer is made from 10.5 mm-thick LiF plates as a shield for the scattered neutrons. The nuclear target can be placed inside the beam duct and can be drawn out from the beam duct using an automatic target changer.

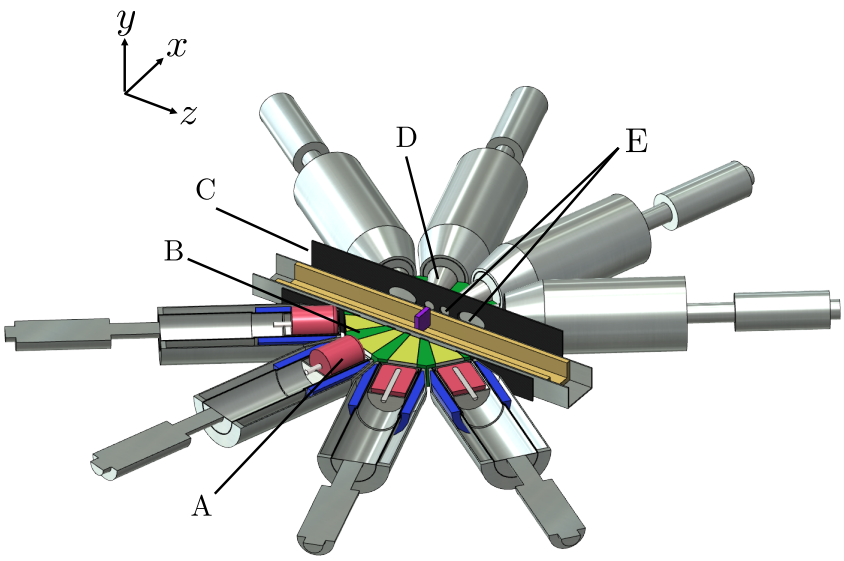

Figure 4.12: Schematic view of the coaxial-type detector unit. (A) Ge crystal, (B) Pb collimator, (C) Carbon board, (D) Neutron shield (LiH powder), and (E) Holes of collimator.

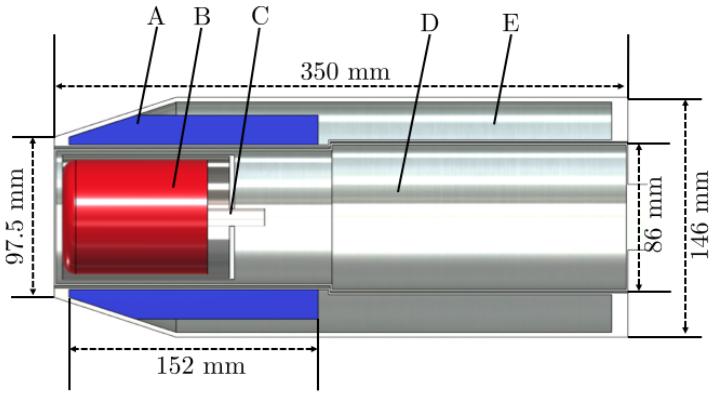

Figure 4.13: Schematic of a coaxial detector. (A) BGO crystal, (B) Germanium crystal, (C) Electrode, (D) and (E) Aluminum cases.

Table 4.2: Setting angle of each germanium detector. Variables θ and φ are the angles at the center of the front-end of each detector.

detector ID	θ [deg]	φ [deg]
d1	90.0	90.0
d2	90.0	66.3
d3	70.9	78.2
d4	70.9	101.8
d5	90.0	113.7
d6	109.1	101.8
d7	109.1	78.2
d8	90.0	270.0
d9	90.0	293.7
d10	70.9	281.8
d11	70.9	258.2
d12	90.0	246.3
d13	109.1	258.2
d14	109.1	281.8
d15	144.0	180.0
d16	108.0	180.0
d17	72.0	180.0
d18	36.0	180.0
d19	36.0	0.0
d20	72.0	0.0
d21	108.0	0.0
d22	144.0	0.0

4.3.2 Simulation of germanium detectors

The pulse heights of output signals from the germanium detectors are not completely true γ-ray energies. In some cases, γ rays cannot deposit their energies into the germanium crystals because of the escape of photons due to the Compton scattering and trapping by lattice defects. Therefore, the observed energies of γ rays shift to lower values.

The geometry of the germanium detector assembly was implemented by a simulation toolkit of GEANT4 [63], and this simulation enabled us to calculate the response function of each germanium detector by emitting γ rays from the target position. The experimental data of γ-ray spectra from radioactive sources of ^{137}Cs and ^{152}Eu placed at the target position were obtained in each detector. Figure 4.14 shows the measured spectra (black dots) and the simulated spectra (red-shaded histogram) for d8 and d22 detectors. It was verified that this simulation can reproduce the γ-ray spectrum for the low-energy region.

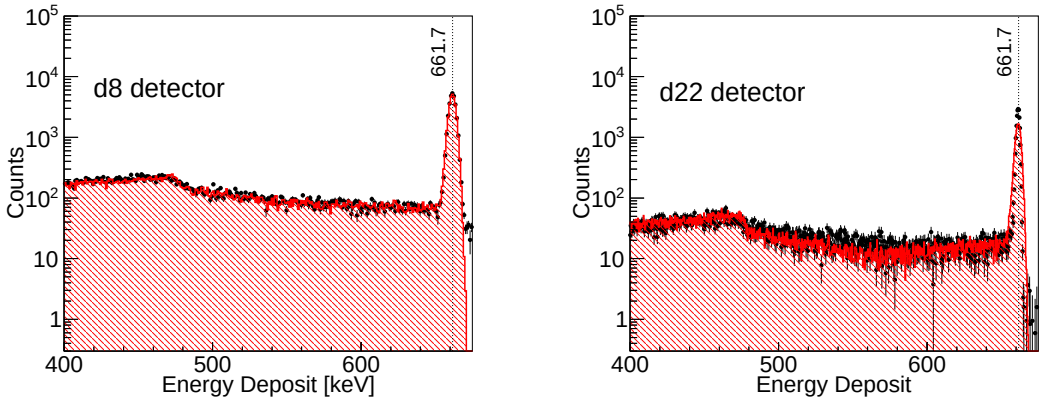

Figure 4.14: Comparison of γ-ray energy spectrum between simulation (red-shaded histogram) and measurement (black dots) with a radioactive source ^{137}Cs [64].

The prompt γ rays from (n,γ) reactions have γ-ray energies of approximately 5 – 9 MeV. Therefore, γ rays from $^{14}N(n,\gamma)$ reactions with energies of up to 11 MeV were used to verify the reproducibility of this simulation in the high-energy region. The γ-ray energy spectrum of $^{14}N(n,\gamma)$ reactions was obtained by using a melamine ($C_3H_6N_6$) target. Figure 4.15 shows comparisons of the spectra measured with the melamine target and the simulated spectra for d8 and d22 detectors. These spectra were reproduced by summing up the simulated spectra of monochromatic γ-ray energy which were scaled to confirm the intensity of the measured spectrum. Here, the background γ rays from $Li(n,\gamma)$, $F(n,\gamma)$, $Al(n,\gamma)$, $Fe(n,\gamma)$, and $Ni(n,\gamma)$ reactions existed, and these were also taken into account. It was verified that this simulation can also reproduce the measured spectrum for the high-energy region. The results show that this simulation reproduces the characteristics of the cluster-type and coaxial-type detectors sufficiently well.

Figure 4.16 shows the distribution of the γ-ray detection angle in full-absorption

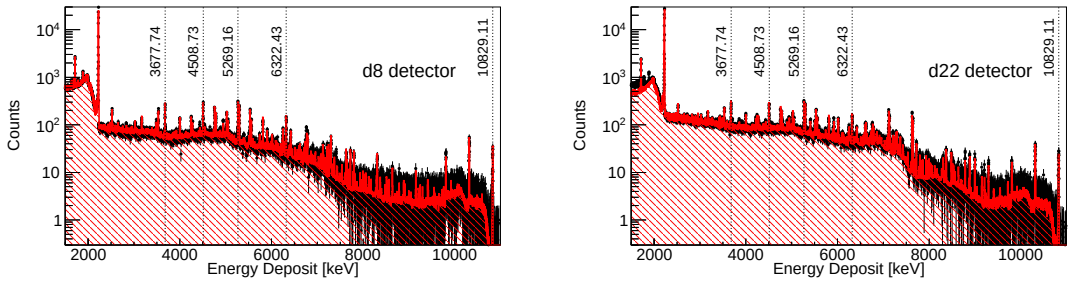

Figure 4.15: Comparison of γ-ray energy spectrum between simulation (red-shaded histogram) and measurement (black dots) with a melamine target [64].

events, which was calculated by the simulation. The dip structures of the peaks are caused by the hole on the back germanium crystal where the electrode is inserted. The dotted lines represent the polar angle of the detector center described in Table 4.2. In the left figure of Fig. 4.16, deviations can be seen between the dotted lines for $\theta = 70.9°$ and $\theta = 109.1°$ and at the center of each front-face. The origin of these deviations is that the d2 - d7 (d9 - d14) detectors are directed farther beyond the target position. This effect is more visible as the γ-ray energy becomes higher. This must be corrected in the analysis of the angular distribution of γ rays. In the right figure of Fig. 4.16, there are no such deviations because the surface of each detector is directed toward the center of the target position.

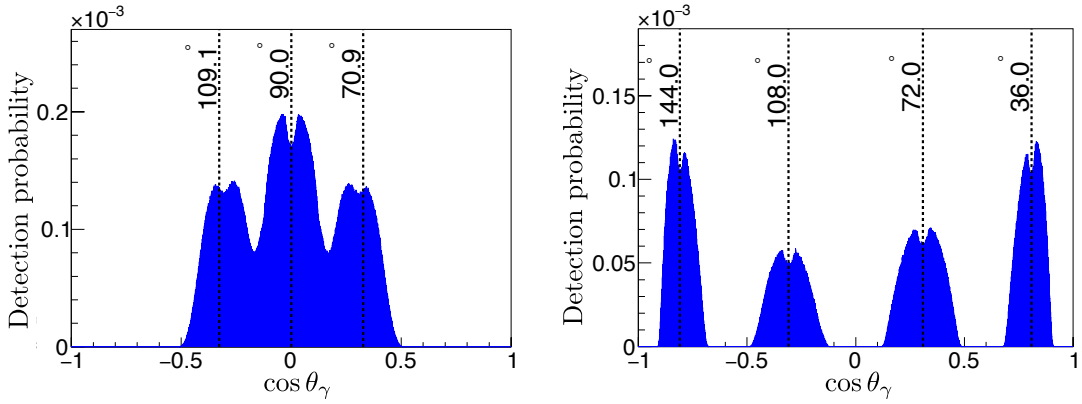

Figure 4.16: Distribution of γ-ray detection angle [64].

4.4 Data acquisition system

The output signals are processed using four CAEN V1724 modules [65]. These four modules are operated synchronizing each other. The output signal from each germanium detector is firstly amplified by the preamplifier, and the information of the pulse height and the timing of its signal is extracted by changing the signal

shape by CAEN V1724 modules as shown in Fig. 4.17. The signal fed into CAEN V1724 is divided into two branches: one is for the timing and triggering, and the other is for the pulse height. Figure 4.18 shows the simplified signal scheme on signal processing. In the branch of timing and triggering, the signal is converted into a bipolar signal with a trigger and timing filter. A signal over a threshold triggers a measurement of the timing of zero-crossing. In the measurements, the threshold corresponds to about 100 keV. The information of the trigger timing is fed to the counter. This counter measures a time interval between the reset signal and the trigger timing using an internal clock with a frequency of 10 ns. This time interval is recorded as a detection time of a γ ray.

In the branch of the pulse height, the signal is converted into a trapezoidal signal, and the pulse height of its signal is determined from the averaged value of the height of its trapezoid from a baseline in its flat-top region. The CAEN V1724 module has a sampling rate of 100 MS/s and a resolution of 14 bit which corresponds to about 137 μV due to the maximum input voltage of 2.5 V peak-to-peak.

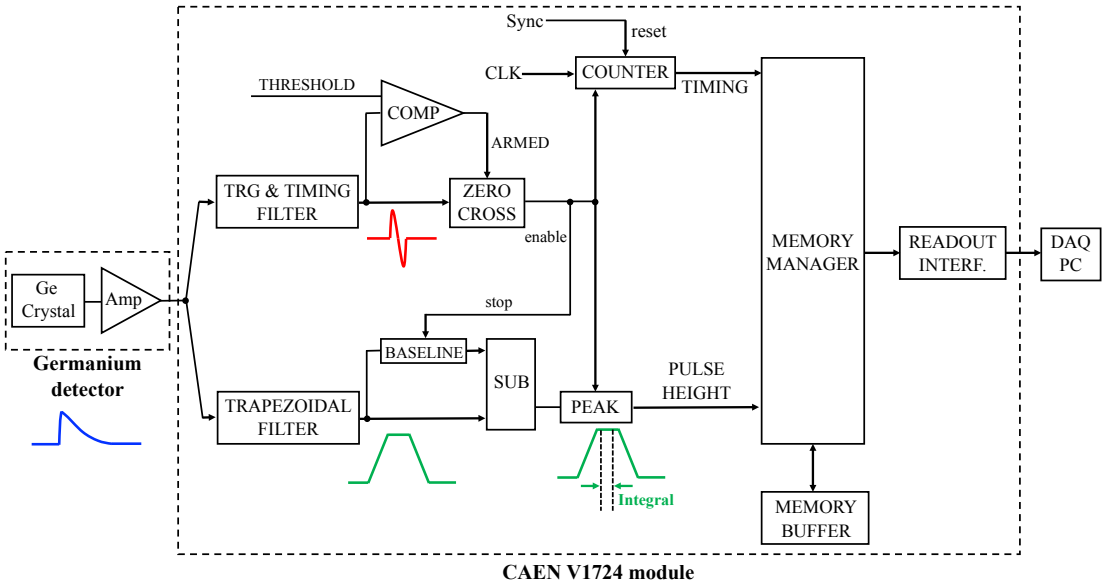

Figure 4.17: Block diagram of V1724 module. A signal from the germanium detector is divided into two branches: one is for the timing and triggering, and the other is for the pulse height. [66].

When the time interval between two signals is small due to the high counting rate, their pulse heights cannot be determined because of the overlapping of their flat-top regions. When the flat-top region is no longer flat due to the overlapping, the pulse height of its signal are recorded as zero. The CAEN V1724 module has four patterns to process signals as shown in Fig. 4.19, which depends on the time interval between the two signals. The four patterns for the i-th signal with its pulse height as E_i and the time information as T_i are classified using t_0, t_1, and t_2

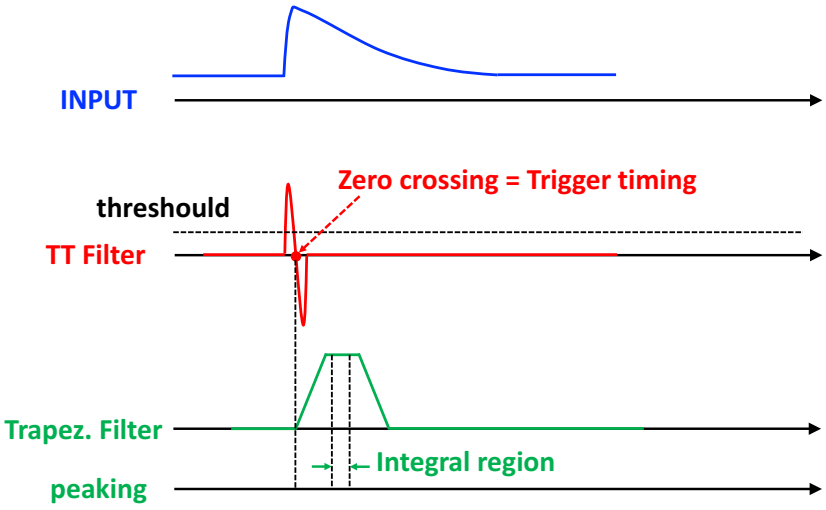

Figure 4.18: Simplified signal scheme on signal processing. The input signal is converted to a bipolar and a trapezoidal signal [66].

as follows.

- Pattern 1 ($T_{i+1} - T_i > t_0$)
  Since the time interval between two signals is sufficiently large, their trapezoidal signals do not overlap with each other. Therefore, their pulse heights E_i and E_{i+1} can be determined correctly. Their time information T_i and T_{i+1} can also be recorded correctly.

- Pattern 2 ($t_1 < T_{i+1} - T_i < t_0$)
  The second trapezoid starts on the trailing edge of the first one. The first pulse height of E_i can be recorded correctly. The second pulse height E_{i+1} cannot be recorded correctly because the flat-top region of the second trapezoid is not flat. In such cases, E_{i+1} is recorded as zero. On the other hand, T_i and T_{i+1} can be recorded correctly.

- Pattern 3 ($t_2 < T_{i+1} - T_i < t_1$)
  The second trapezoid starts on the leading edge of the first one. Both pulse heights E_i and E_{i+1} are recorded as zero because the flat regions of two trapezoids overlap with each other. Their time information can be recorded correctly because their trigger timing can be distinguished.

- Pattern 4 ($T_{i+1} - T_i < t_2$)
  The two input pulses pile-up in the input rise time. In this case, their two signals are regarded as one. The pulse height E_i is recoded as the sum value of two pulse heights, and the time information T_i is recorded as the trigger timing of the first signal.

In the measurements, the values of t_0, t_1, and t_2 are 3.17 μs, 2.47 μs, and 0.42 μs, respectively. These values were confirmed to be independent of their pulse heights. The CAEN V1724 transfers the stored data to the computer when 1024 events data are accumulated in the local buffer. When the speed of accumulating the data in the local buffer exceeds the speed at which to write are recorded to the computer, whose counting rate is around 300 kcount/s, there is a possibility that CAEN V1724 modules stop. If the accelerator is stopped for a long time, the timing can be reset in each 10.7374 seconds because the data recording range of the time information is 32 bit.

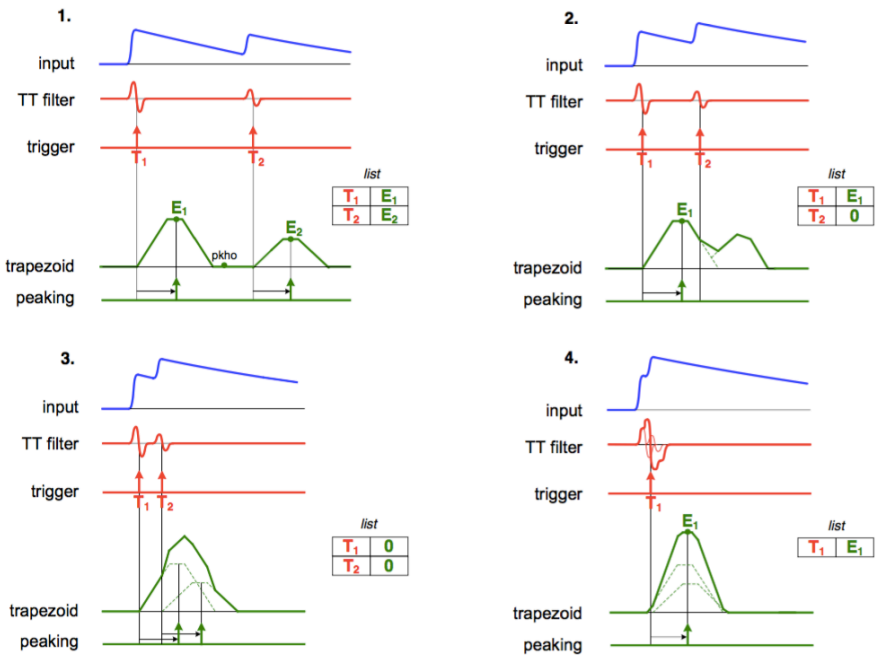

Figure 4.19: Effect of trapezoid overlapping in the four main cases. (1) The two trapezoids are well separated (top left). (2) The second trapezoid starts on the falling edge of the first one (top right). (3) The second trapezoid starts on the rising edge on the first one (bottom left). (4) The two input pulses pile-up in the input rise time (bottom right) [66].

Chapter 5

Measurements

In this chapter, the details of the measurements and targets used for the experiment are described.

5.1 Experimental condition

In this study, three measurements were conducted to determine the mixing angle ϕ and the $\kappa(J)$ value of ^{117}Sn. The measurement of the angular dependence of the differential cross section at the p-wave resonance is the main purpose for this study, while resonance parameters and relative transition ratios of the 9327 keV γ-ray emission for each resonance are input parameters for the calculation of the Flambaum formalism. Table 5.1 summarizes the experimental condition and the target used for each measurement. In addition to these measurements, an experiment was conducted to obtain neutron-energy dependence of the beam intensity, which is described in Sec. 5.3. The properties of the targets are described in Sec. 5.2.

Table 5.1: Summary of experimental condition.

	May 2017	June 2018	April 2019
Purpose	Angular dependence	Relative transition ratios	Resonance parameters
Target (size)	^{nat}Sn ($40\times40\times4$ mm^3)	^{nat}Sn ($40\times40\times1$ mm^3)	^{117}Sn 87% enriched ($\phi5$ mm$\times6$ mm)
Self-filter (size)	-	^{nat}Sn ($40\times40\times10$ mm^3)	-
Collimator size [mm]	22	15	22
Proton beam power [kW]	150	525	525
Measurement time [h]	65	100	6

5.2 Nuclear targets

In this study, three targets were used: tin with natural abundance, ^{117}Sn-enriched tin, and boron targets. These targets were sealed by polytetrafluoroethylene with a thickness of 10 μm due to the regulation at MLF.

5.2.1 Tin target with natural abundance

The $^{\mathrm{nat}}$Sn targets were used in this experiment to measure the angular dependence of differential cross section at the p-wave resonance as well as the relative transition ratio of each resonance. The targets in these measurements did not have to be an enriched target because events of the single transition from the compound state to the ground state of ^{118}Sn can be selected by gating with γ-ray peaks. These targets were purchased from The Nilaco Corporation, and the chemical purity was 99.9%. Table 5.2 shows the properties of Tin isotopes.

Table 5.2: Properties of tin isotopes [67].

Mass number	Abundance [%]	Cross section [barn]	Number of energy state
115	0.34 ± 0.1	30 ± 7	395
116	14.54 ± 0.09	0.14 ± 0.03	9
117	7.68 ± 0.07	1.32 ± 0.18	19
118	24.22 ± 0.09	0.23 ± 0.05	9
119	8.59 ± 0.04	2.2 ± 0.5	9
120	32.58 ± 0.09	0.14 ± 0.03	10
122	4.63 ± 0.03	0.139 ± 0.015	9
124	5.79 ± 0.05	0.134 ± 0.005	25

5.2.2 ^{117}Sn-enriched tin target

A ^{117}Sn-enriched tin target was used to measure the resonance parameters in ^{117}Sn(n, γ) reaction. The composition of this target is described in Table 5.3. The enriched target was used for this measurement to suppress γ rays from other isotopes and elements because all transitions were used to determine the resonance parameters. Especially, when the resonance parameters of the negative s-wave resonance are determined, prompt γ rays from capture reactions by other nuclei become irreducible background events because most nuclei have no resonance at less than 1.0 eV.

5.2.3 Boron carbide target

The boron carbide target was used to measure the energy dependence of the neutron beam intensity by detecting γ rays from ^{10}B(n, $\alpha\gamma$)^{7}Li reactions. The chemical formula is B_4C, and boron carbide powder made from 95% enriched ^{10}B and carbon powder was pressed into a tablet with dimensions of ϕ5.08 mm $\times$ 0.59 mm. The

Table 5.3: Composition of ^{117}Sn-enriched tin target.

Isotope	Fraction [%]	Element	Contamination [ppm]
^{112}Sn	< 0.01	Fe	40
^{114}Sn	< 0.01	Al	50
^{115}Sn	0.2	Si	60
^{116}Sn	9.3	Cr	30
^{117}Sn	87	Ni	< 10
^{118}Sn	3	Cu	100
^{119}Sn	0.4	Pb	20
^{120}Sn	< 0.05	Sb	100
^{122}Sn	< 0.01	Ga	< 10
^{124}Sn	< 0.01	In	< 10
		Zn	120
		Mg	< 10

γ rays from $^{10}\mathrm{B}(\mathrm{n}, \alpha\gamma)^{7}\mathrm{Li}$ reactions are used to measure the energy dependence of the neutron beam intensity because its cross section is very large (3837 barns for thermal neutrons as shown in Fig. 5.1), and it is easy to separate background γ rays from other nuclei because the γ-ray energy emitted in this reaction is only 477.6 keV. Moreover, there is no resonance in the epithermal region ($\mathcal{O}(1)$ eV) in $^{10}\mathrm{B}(\mathrm{n}, \alpha\gamma)^{7}\mathrm{Li}$ reaction. Therefore, the number of lost events does not increase only in certain energy regions.

5.3 Collected data

5.3.1 Measurement of spectrum for ^{117}Sn(n, γ) reactions

Angular dependence

The measurement of the angular dependence of the p-wave resonance was performed using the $^{\mathrm{nat}}$Sn target for 65 hours with the collimator size of 22 mm. Figure 5.2 shows the TOF spectrum obtained by detecting γ rays from $^{\mathrm{nat}}\mathrm{Sn}(\mathrm{n}, \gamma)$ reactions. The blue-open histogram shows all the events without event selection for all detectors. The red-hatched histogram depicts the events whose pulse heights were recorded as zero for all detectors. The peaks around 1360 μs are the 1.33 eV p-wave resonance by $^{117}\mathrm{Sn}(\mathrm{n}, \gamma)$ reaction and the 1.45 eV s-wave resonance by $^{115}\mathrm{In}(\mathrm{n}, \gamma)$ reaction. According to the JENDL database [48], the cross section of the 1.33 eV p-wave resonance is about 1.8 barn, while that of the 1.45 eV s-wave resonance is approximately 2.9×10^4 barn. Thus, their count rates become comparable if the target is contaminated by 0.01% of ^{115}In. The s-wave resonance caused by $^{115}\mathrm{In}(\mathrm{n}, \gamma)$ reaction is eliminated by gating with events of γ rays via $^{117}\mathrm{Sn}(\mathrm{n}, \gamma)$ reactions, which are described in Sec. 6.2. The peak at 630 μs is the 6.2 eV p-wave resonance by $^{119}\mathrm{Sn}(\mathrm{n}, \gamma)$ reaction. The amount of events with their pulse heights as zero around the p-wave resonance is approximately 2% for all events, which implies that the amount of lost events is estimated to be about 0.3% around the

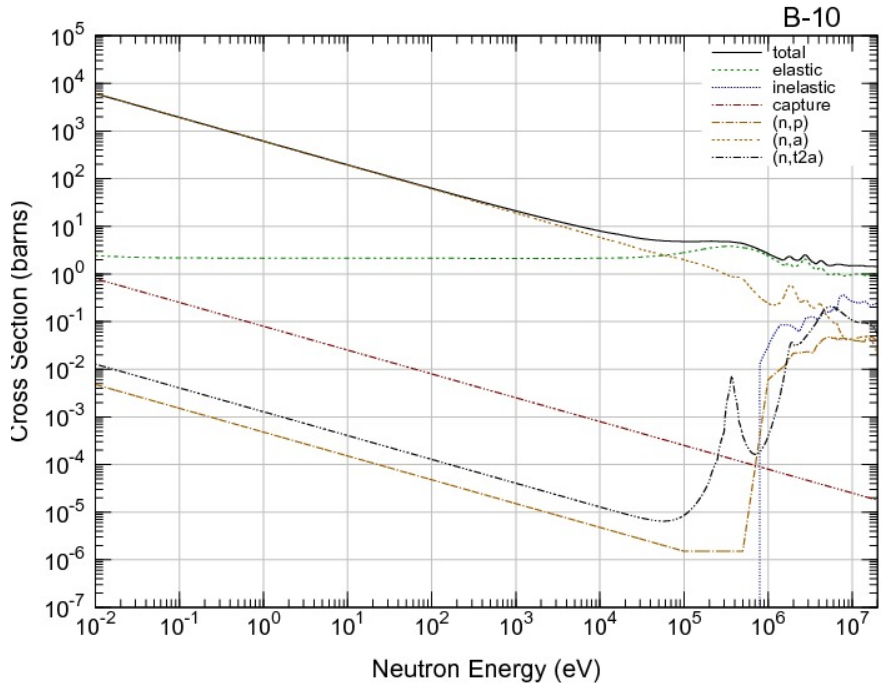

Figure 5.1: Cross sections of ^{10}B [48]. There is no resonance around epithermal energy region in $^{10}\mathrm{B}(\mathrm{n},\alpha\gamma)^{7}\mathrm{Li}$ reaction.

p-wave resonance. Therefore, the contribution by lost events is negligible because the number of lost events is estimated to be smaller than the statistical error.

Figure 5.3 shows the spectrum of the energy deposit of γ rays in all germanium detectors (blue-open histogram) and the spectrum gated with a TOF range corresponding to 1.0 – 1.6 eV (red-hatched histogram). The γ-transition in the nucleus ^{118}Sn with the energy of 9327 keV and its single- and double-escape peaks can be observed clearly in both spectra, which indicates that the compound state in the p-wave resonance decays to the ground state of ^{118}Sn.

Relative transition ratios

The measurement of relative transition ratios was performed using the $^{\mathrm{nat}}$Sn target and the $^{\mathrm{nat}}$Sn self-filter for 100 hours with the collimator size of 15 mm. In order to determine the relative transition ratios of the 9327 keV γ-ray emission for both the s-wave and the p-wave resonances, sufficient statistics is required for both resonances. However, the cross section of the s-wave resonance is much larger than that of the p-wave resonance. Because the data acquisition rate was limited by the s-wave resonance, the statistics of γ rays from the p-wave resonance might not be enough. To resolve this problem, the measurement with the self-filter upstream from the target position was conducted. This measurement method enabled to reduce the neutron flux in an energy region around the s-wave resonance because neutrons with energies around the s-wave resonance were captured by the self-filter. On the other hand, most of the neutrons with energies around the p-wave resonance were not captured by the self-filter because of the small cross section.

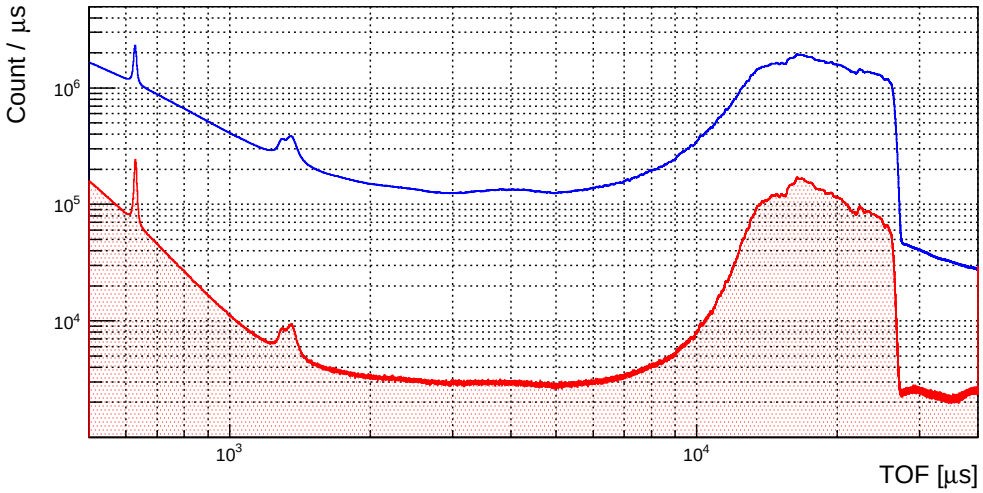

Figure 5.2: TOF spectrum of γ rays from the $^{\mathrm{nat}}\mathrm{Sn}(\mathrm{n},\gamma)$ reactions. The blue-open histogram shows all the data, while the red-hatched histogram depicts spectrum in which the pulse heights were recorded as zero. The small peaks around 1350 μs are the p-wave resonance of ^{117}Sn and the s-wave resonance of ^{115}In.

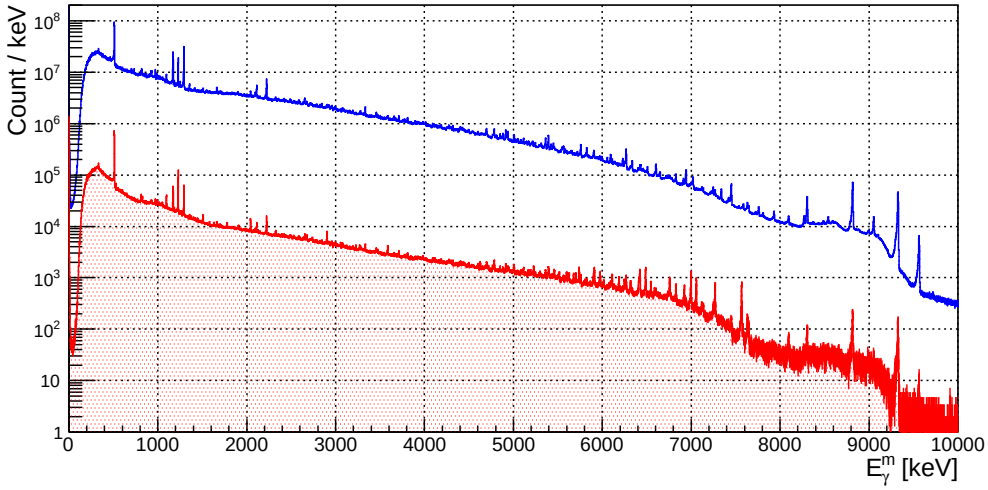

Figure 5.3: Pulse height spectrum of γ rays from the $^{\mathrm{nat}}\mathrm{Sn}(\mathrm{n},\gamma)$ reactions. The blue-open spectrum is all the data, while the red-hatched spectrum is gated with a TOF range corresponding to 1.0 – 1.6 eV.

Figure 5.4 shows the TOF spectrum measured with the self-filter. The large peaks at 235 μs and at 250 μs are the 45.7 eV s-wave resonance by ^{124}Sn(n, γ) reaction and the 38.8 eV s-wave resonance by ^{117}Sn(n, γ) reaction, respectively. The ratios of events with their pulse heights as zero were 0.31% around the p-wave resonance and 23% around the 38.8 eV s-wave resonance, respectively. This implies the amounts of lost events around the p-wave and the s-wave resonance are estimated to be approximately 0.03% and 3%, respectively. They are negligible compared to the statistical error.

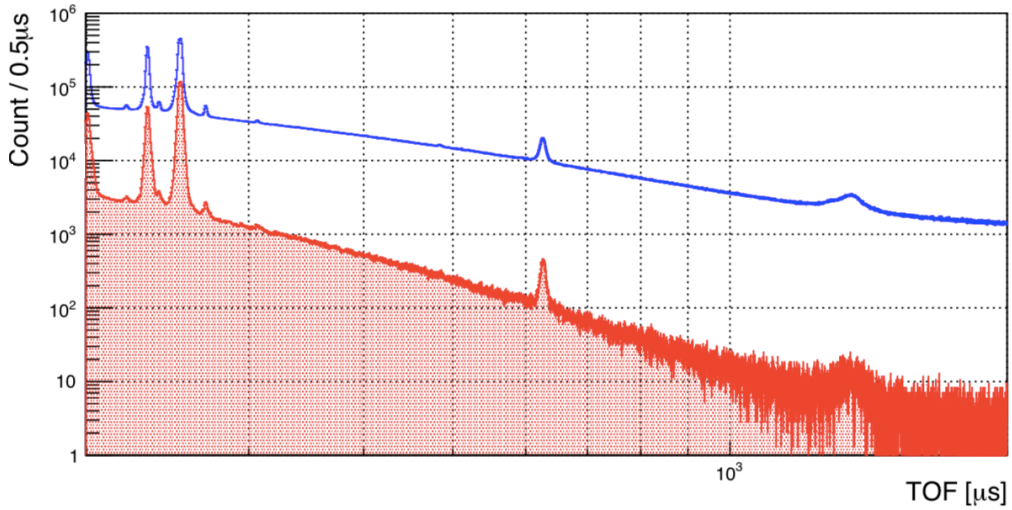

Figure 5.4: TOF spectrum of γ rays from the ^{nat}Sn(n, γ) reactions with the self filter. The blue-open histogram shows all the data, while the red-hatched histogram depicts the spectrum in which the pulse heights were recorded as zero.

Resonance parameters

The measurement of resonance parameters was performed using the ^{117}Sn-enriched tin target for 6 hours with a collimator size of 22 mm in diameter. The resonance parameters can be determined from events corresponding to all transitions from the compound state. Thus, prompt γ rays with a wide range from low to high energy are used in the analysis. However, the measured spectrum includes background events. The background events are caused by cosmic rays and γ rays emitted from the materials which consist of the detector assembly. The background spectrum was measured for 2 hours without the target and a collimator size of 22 mm. Figure 5.5 shows the TOF spectrum measured with and without the ^{117}Sn-enriched tin target. Resonances caused by isotopes are smaller than those in the spectrum measured with the ^{nat}Sn target (See Fig. 5.4).

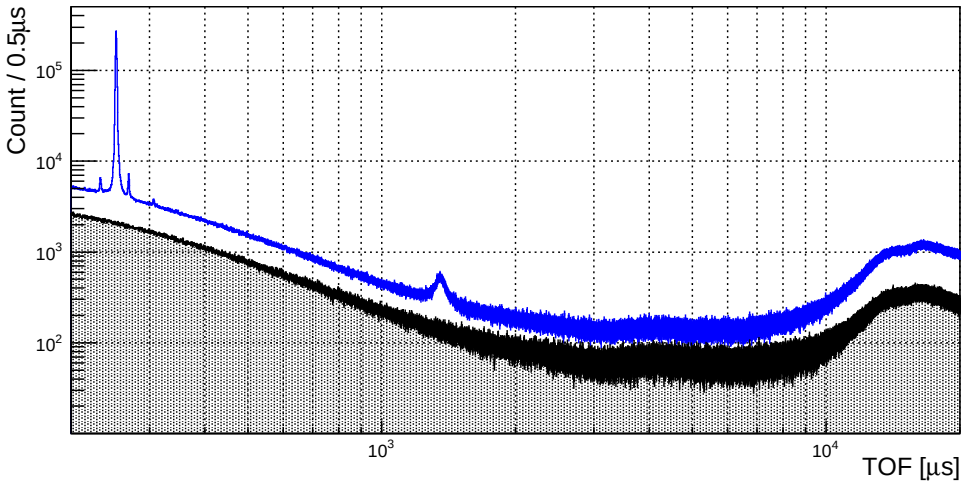

Figure 5.5: TOF spectra measured with and without ^{117}Sn-enriched target. The blue-open spectrum was measured with the target. The black-hatched spectrum was measured without the target.

5.3.2 Measurement of the beam intensity spectrum

The neutron-energy dependence of the beam intensity was obtained by measuring γ rays from $^{10}\mathrm{B}(\mathrm{n},\alpha\gamma)^{7}\mathrm{Li}$ reactions with the boron carbide target placed at the center of the germanium detector assembly. The measurement was performed for 2.4 hours with the collimator size of 22 mm in diameter. Figure 5.6 shows a γ-ray energy spectrum. The peak at 477.6 keV is a full absorption peak from $^{10}\mathrm{B}(\mathrm{n},\alpha\gamma)^{7}\mathrm{Li}$ reactions.

The number of detected γ rays with an energy of 477.6 keV, $N_\gamma(E_\mathrm{n})$, is described as

$$\begin{aligned} N_\gamma(E_\mathrm{n}) &= I(E_\mathrm{n})TS\epsilon(E_\gamma)(1-\exp(-\rho t\sigma(E_\mathrm{n}))) \\ &\approx I(E_\mathrm{n})TS\epsilon(E_\gamma)\rho t\sigma(E_\mathrm{n}), \end{aligned} \tag{5.1}$$

where $I(E_\mathrm{n})$ is the beam intensity, T is the measurement time, S is the area ratio of the target size to the beam size, $\epsilon(E_\gamma)$ is the detection efficiency of the germanium detector assembly for the 477.6 keV γ rays, ρ is the number density of ^{10}B in the target, t is the thickness of the target, and $\sigma(E_\mathrm{n})$ is the cross section of $^{10}\mathrm{B}(\mathrm{n},\alpha\gamma)^{7}\mathrm{Li}$ reaction.

The neutron-energy-dependent beam intensity was obtained by dividing $N_\gamma(E_\mathrm{n})$ by $\sigma(E_\mathrm{n})$. The values of $\sigma(E_\mathrm{n})$ are referred from JENDL-4.0 [48]. In the epithermal energy region, the beam intensity increases for lower neutron energies as shown in Fig. 5.7.

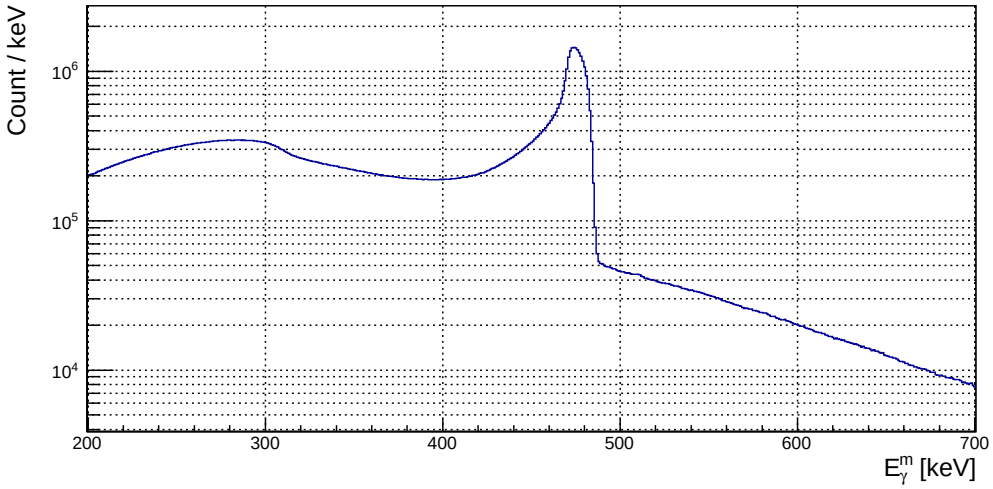

Figure 5.6: Spectrum of γ-ray energy with the boron carbide target. The peak at 477 keV is a full absorption peak from $^{10}\mathrm{B}(\mathrm{n}, \alpha\gamma)^7\mathrm{Li}$ reactions.

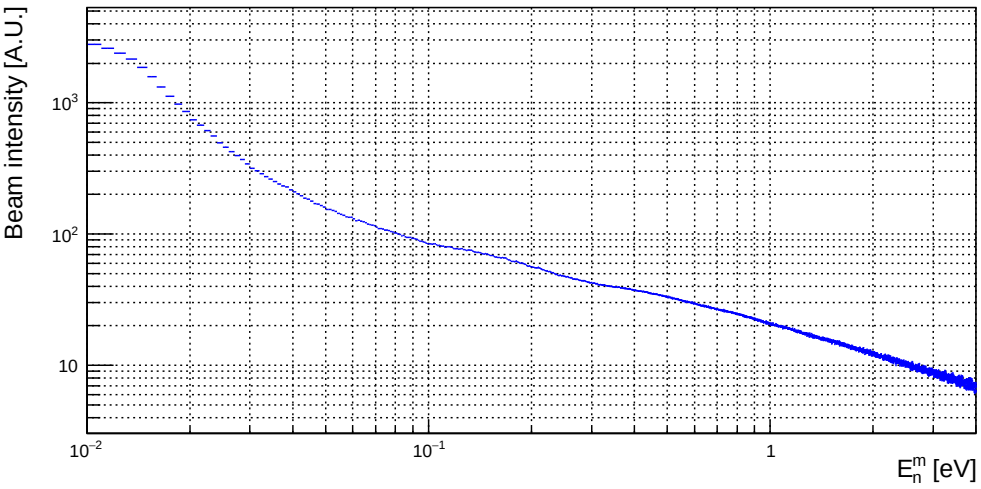

Figure 5.7: Energy dependence of the neutron beam intensity.

Chapter 6

Analysis

In this chapter, the analysis method to obtain the angular dependence of the p-wave resonance shape is explained. The resonance parameters and the relative transition ratio for each resonance of $^{117}\mathrm{Sn}(\mathrm{n},\gamma)$ reaction are determined. Finally, the values of the mixing angle ϕ and $\kappa(J)$ are determined.

6.1 Overview of analysis

Three measurements were performed to determine the mixing angle ϕ and the $\kappa(J)$ value of ^{117}Sn. Firstly, the collected data are independently analyzed. For each data, the following procedures are conducted: the definition of signal regions (Section 6.2), and correction and normalization of neutron-energy spectrum (Section 6.3). This correction and normalization include the subtraction of background events, correction of pile-up events, and normalization of the neutron beam intensity. The resonance parameters and the relative transition ratio for each resonance are determined by fitting using the Breit-Wigner function convoluted some effects (Sections 6.4 and 6.5). These results are used to calculate the angular dependence of the p-wave resonance shape based on theoretical formalism described in Chapter 3. On the other hand, from the obtained data, the angular dependence of the p-wave resonance shape is evaluated quantitatively (Section 6.6), and its systematic errors are estimated (Section 6.7). Finally, the mixing angle ϕ and the $\kappa(J)$ value are determined using the experimental result and the calculation result from theoretical formalism (Section 6.8). Figure 6.1 shows the analysis flow chart.

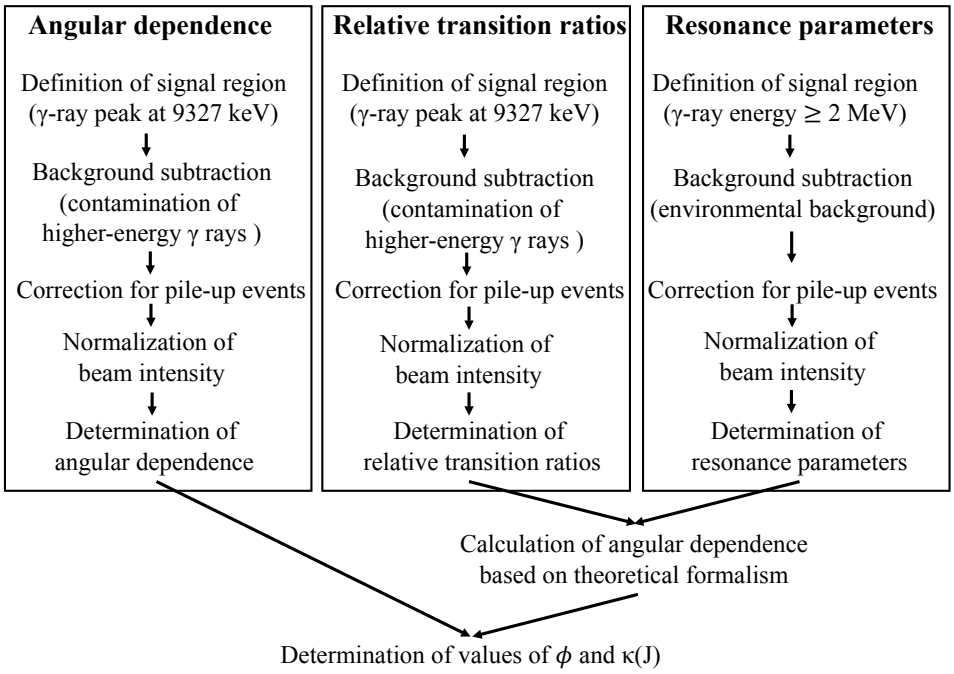

Figure 6.1: Analysis flow chart. Firstly, three collected data are independently analyzed. For each data, the neutron-energy spectrum is corrected and normalized. The calculated value of the angular dependence of the p-wave resonance shape is obtained using the theoretical formalism. The experimental value of the angular dependence is obtained from data. The mixing angle ϕ and the $\kappa(J)$ value are determined using the experimental result and the calculation result of the angular dependence of the p-wave resonance shape.

6.2 Definition of signal regions

The Flambaum formalism insists that the γ rays emitted from the compound states can lead to the angular dependence of the shape of a p-wave resonance, and the behavior of the angular dependence is different for the spin of the final state. The observed events include γ rays emitted from excited states except for the compound states. Therefore, signal regions should be defined using γ-ray peaks caused by the compound states. The 9327 keV γ-ray peak was adopted as the signal region because γ rays in this peak are obtained via the transitions from the compound state of ^{118}Sn to the ground state. Its single- and double-escape peaks were added as the signal regions because their events have the same angular dependence.

The ranges of the signal regions are defined as the full width at quarter maximum (FWQM). This is the range in which the height h' excluding the background events at a given energy satisfies the following equation;

$$h' \geq \frac{1}{4}\left(h_{\mathrm{pk}} - h_{\mathrm{bg}}\right). \tag{6.1}$$

Here, $h_{\rm pk}$ and $h_{\rm bg}$ are the heights of peak and background, respectively. Figure 6.2 shows an illustration of FWQM. The horizontal axis is γ-ray energy, and the vertical axis is the number of events. The range between the green-vertical lines is defined as a signal region which satisfies the condition of Eq. (6.1). The signal regions for the d8 detector are shown in Fig. 6.3. The three green bands represents the signal regions for full-absorption, its single-escape, and double-escape peaks.

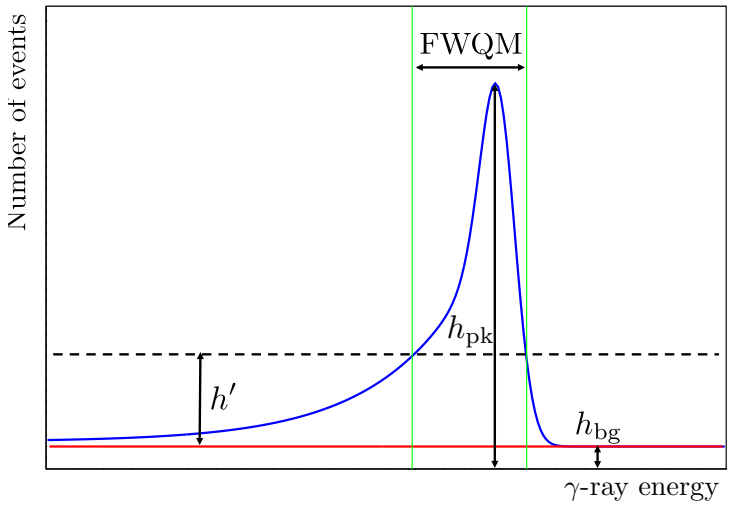

Figure 6.2: Definition of signal region for γ-ray peaks. The horizontal axis is γ-ray energy and the vertical axis is the number of events. The range between the green-vertical lines is defined as a signal region which satisfies the condition of Eq. (6.1).

Figure 6.4 shows the neutron-energy spectrum gated the signal regions for all detectors. In Section 5.3.1, it is mentioned that the 1.46 eV s-wave resonance by ^{115}In(n, γ) reactions was observed. This s-wave resonance was eliminated by gating with the signal regions because the highest γ-ray energy emitted by ^{115}In(n, γ) reaction is 6561 keV.

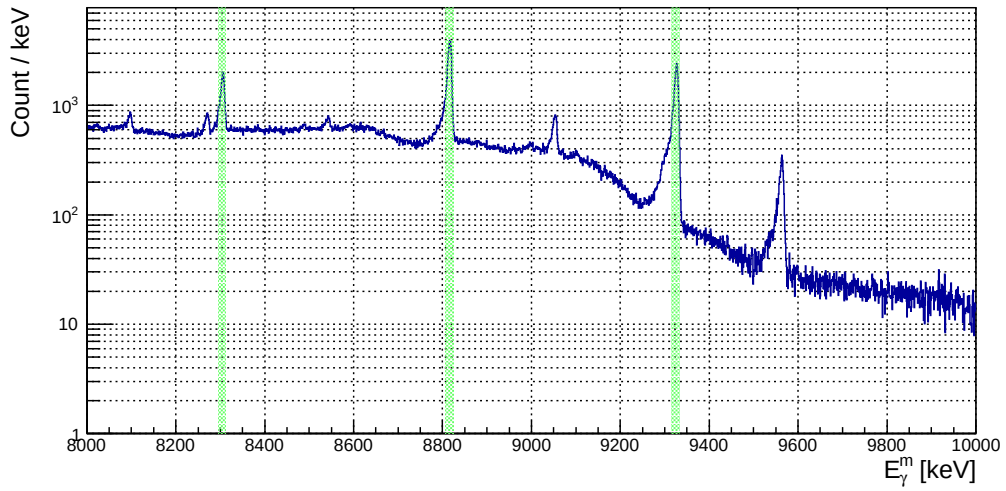

Figure 6.3: Signal regions for γ-ray peaks in measurement data. The three green bands represent the signal regions for full-absorption, its single-escape, and double-escape peaks.

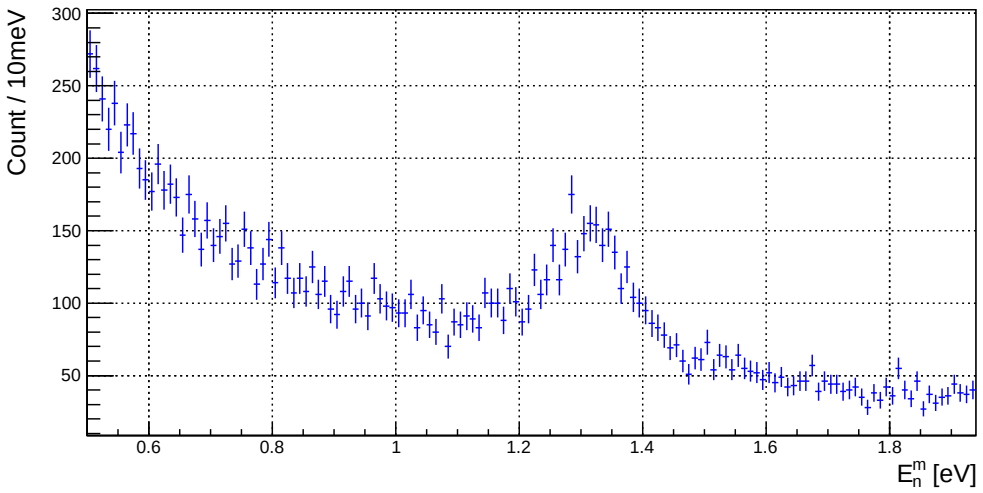

Figure 6.4: Neutron-energy spectrum gated with the signal regions for all detectors. The 1.46 eV s-wave resonance from the ^{115}In(n, γ) reactions was eliminated.

6.3 Spectrum correction and normalization

The obtained neutron-energy spectrum includes the background events and the energy dependence of beam intensity. The spectrum should be corrected to exclude these effects. In this section, the correction methods and their results are explained.

6.3.1 Background subtraction

The neutron-energy spectrum of signal events was obtained by subtracting the spectrum of background sources. There are two kinds of background sources. One is caused by the Compton scattering of γ rays with 9563 keV which were emitted by $^{115}\mathrm{Sn}(\mathrm{n},\gamma)$ reactions. The amount of these background events contaminating in the signal regions was estimated using the GEANT4 simulation. In this simulation, the spectrum by γ rays with the monochromatic energy of 9563 keV was obtained by emitting isotopically γ rays with this energy from the target position. The amount of contamination in the signal regions was obtained by scaling the simulated spectrum so that the intensity of the full-absorption peak of 9563 keV matched between data and simulation. The blue-open spectrum in Fig. 6.5 shows the collected γ-ray energy spectrum without event selection. The red-hatched spectrum in Fig. 6.5 shows the simulated spectrum after scaling.

The other background source is caused by simultaneous detections of multi γ rays. Some of the energies obtained by such events are greater than 10 MeV. This background spectrum is continuous because γ rays with various energies are simultaneously detected in random combinations. This background spectrum was obtained by subtracting the two simulated spectra by monochromatic energies of 9563 keV and 9327 keV from the measured spectrum. The black-striped spectrum in Fig. 6.5 shows this continuous background spectrum.

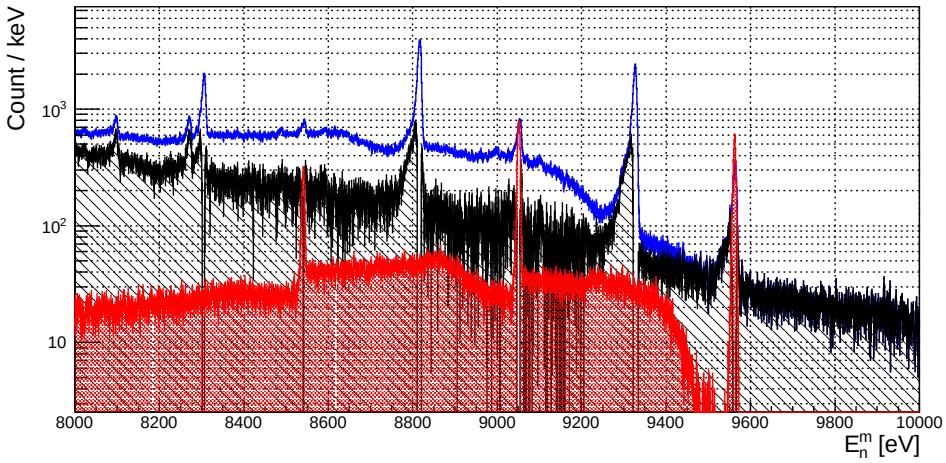

Figure 6.5: Spectrum of γ-ray energy of each background component. The blue-open spectrum is the γ-ray energy spectrum without event selection. The red-hatched spectrum shows the background events stemmed from the 9563 keV γ rays. The black-striped spectrum shows the background events stemmed from simultaneous detections of multi γ rays.

The amount of these background events can be estimated by counting the number of events contaminating the signal regions for the red-hatched and black-striped spectra in Fig. 6.5. The neutron-energy spectra of these background events were obtained by gating the ranges of the full-absorption peak of 9563 keV and greater than 9600 keV. Figure 6.6 shows the neutron energy spectra before and

after background subtraction. The average amount of background events in all detectors was estimated to be approximately 13% for all obtained events.

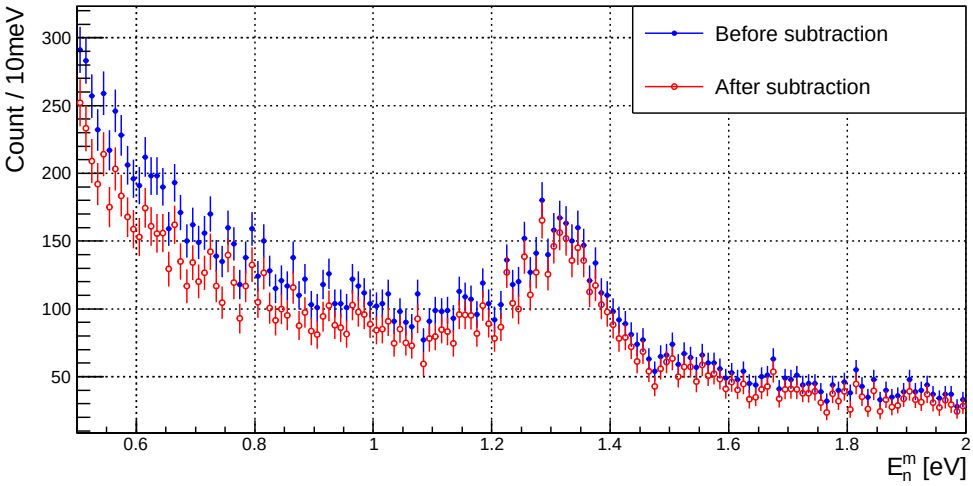

Figure 6.6: Comparison of neutron-energy spectrum before and after subtraction. The blue and red spectra represented by closed and open circles are before and after subtraction, respectively.

6.3.2 Pile-up events correction

As mentioned in Chapter 4, the DAQ system records the pulse heights as zero or regards two signals as one signal when the time difference between signals is too short. In the measurements, the number of lost events by being regarded as one signal can be ignored because it is smaller than the statistical error. Some of the γ rays with 9327 keV were recorded with their pulse heights as zero. The neutron-energy spectrum gated with the signal regions loses these events, so the number of events needs to be corrected. The ratio of the number of events with pulse heights of zero to that of total events is denoted by R. The number of events whose energies were observed as 9327 keV ($N_{9327\mathrm{keV}}$) can be written using the actual number of signal events (N_{true}) as

$$N_{9327\mathrm{keV}} = N_{\mathrm{true}}(1 - R). \tag{6.2}$$

The correction ratio $1/(1-R)$ can be obtained using the number of total events N_{tot} and the number of events with non-zero pulse height N_{nonzero} as

$$\frac{N_{\mathrm{tot}}}{N_{\mathrm{nonzero}}} = \frac{N_{\mathrm{tot}}}{N_{\mathrm{tot}}(1-R)} = \frac{1}{1-R}. \tag{6.3}$$

Figure 6.7 shows the correction ratio around the p-wave resonance. The vertical axis is the correction ratio $1/(1-R)$. The amount of correction is about 2% at the vicinity of the p-wave resonance.

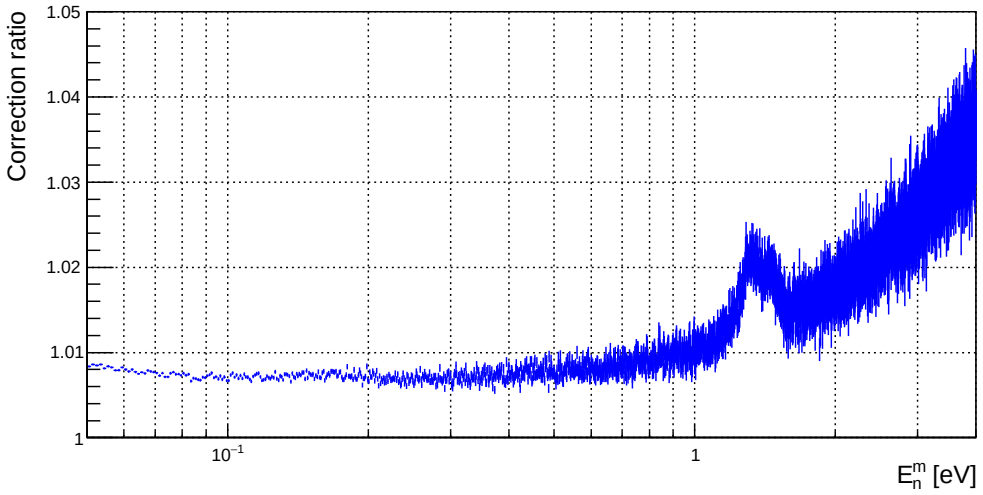

Figure 6.7: Correction ratio of pile-up events for neutron-energy spectrum. The vertical axis is the correction ratio $1/(1-R)$. The amount of correction is about 2% at the vicinity of the p-wave resonance.

Figure 6.8 shows the spectra before and after pile-up events correction. It is confirmed that the number of events hardly change before and after the correction around the p-wave resonance.

6.3.3 Normalization of energy dependence of neutron beam intensity

The measured spectrum includes the energy dependence of neutron beam intensity, which is described as Eq. (5.1). The energy dependence of neutron beam intensity can be canceled out in all neutron energy regions by dividing the spectrum measured with Sn target by the beam intensity spectrum as shown in Fig. 5.7. Figure 6.9 shows the neutron energy spectra before and after the beam intensity normalization. The number of events in the low-energy region (less than 1 eV) after normalization is smaller than that before normalization. This is because the neutron beam intensity at BL04 increases for lower neutron energies.

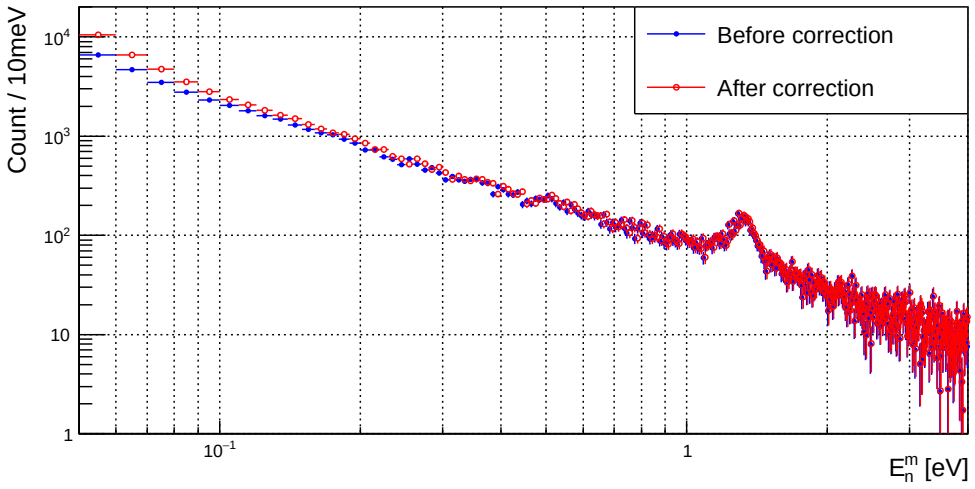

Figure 6.8: Comparison of neutron energy-spectrum between before and after pile-up events correction. The blue and red spectra represented by closed and open circles are before and after correction, respectively. It is confirmed that the number of events hardly changes before and after the correction around the p-wave resonance.

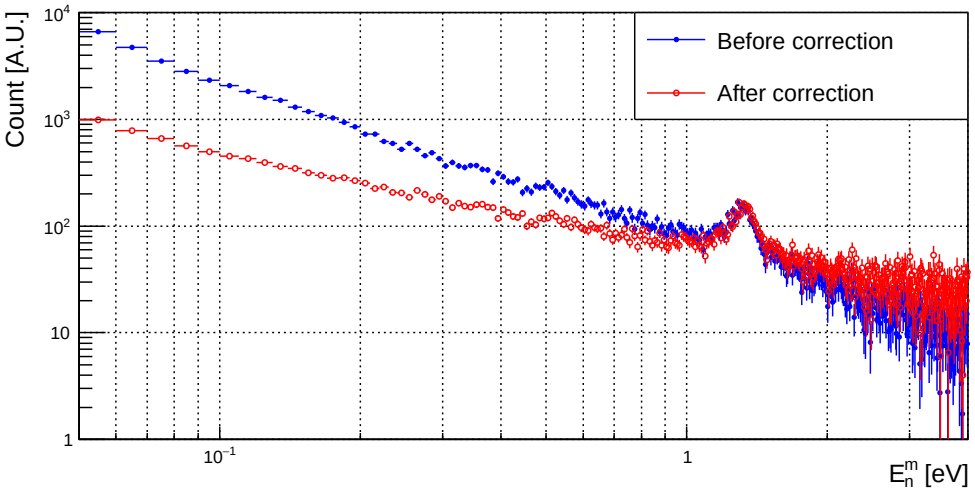

Figure 6.9: Comparison of neutron-energy spectrum between before and after the beam intensity normalization. The blue and red spectra represented by closed and open circles are before and after normalization, respectively. The number of events in the low-energy region (less than 1 eV) after normalization is smaller than that before normalization.

6.4 Determination of resonance parameters

The resonance parameters of each resonance can be determined by fitting the spectrum measured with the ^{117}Sn-enriched target by the Breit-Wigner function. Some effects to be considered are the Doppler broadening effect, the energy resolution of the pulsed neutron beam, and the self-shielding effect, which cannot be removed using the corrections described in the previous sections. Therefore, the fitting function must include these effects. In this section, these effects and the method to introduce them into the fitting function are explained.

6.4.1 Doppler broadening effect

The cross sections of ^{117}Sn with neutrons are described using the center-of-mass energy $E_{\rm cm}$ between a neutron and a target nucleus. When the target nucleus vibrates thermally with a velocity of u, the $E_{\rm cm}$ can be written as

$$E_{\rm cm} = \frac{1}{2} m_{\rm n}(v \pm u)^2 \approx E_{\rm n} \pm u\sqrt{2m_{\rm n}E_{\rm n}}. \tag{6.4}$$

This implies that the energy range which causes neutron capture can be wide depending on the velocity of the thermal vibration of the target nuclei. The increase of observed resonance width is called the Doppler broadening effect. The calculation of the cross section taken into account the Doppler broadening effect is explained as follows.

Here, an ideal gas model is used [68, 69]. The Doppler-broadened cross section $\bar{\sigma}$ with energy E and temperature T can be described using an energy transfer function $S(E, E_{\rm cm})$ and the original cross section σ as

$$\bar{\sigma}(E) = \int dE_{\rm cm} S(E, E_{\rm cm})\sigma(E_{\rm cm}). \tag{6.5}$$

The velocity of nuclei of the ideal gas follows the Maxwell-Boltzmann distribution, so that the $S(E, E_{\rm cm})$ is given as [70]

$$S(E, E_{\rm cm}) = \frac{1}{\Delta\sqrt{\pi}} \exp\left[-\left(\frac{E_{\rm cm} - E}{\Delta}\right)^2\right], \tag{6.6}$$

$$\Delta \equiv \sqrt{\frac{4Ek_{\rm B}T}{M/m_{\rm n}}}, \tag{6.7}$$

where $k_{\rm B}$ is the Boltzmann constant and M is the mass of the target nucleus. Variable Δ is called the Doppler width. For $E \gg \Delta$, the $\bar{\sigma}(E)$ is approximated as follows [71].

$$\bar{\sigma}(E) = \frac{1}{\Delta\sqrt{\pi}} \int dE_{\rm cm} \exp\left[-\left(\frac{E_{\rm cm} - E}{\Delta}\right)^2\right] \sqrt{\frac{E_{\rm cm}}{E}}\sigma(E_{\rm cm}). \tag{6.8}$$

Figure 6.10 shows an example of a calculation result of the Doppler broadening effect using Eq. (6.8) for the cross section of the p-wave resonance of ^{117}Sn. It is confirmed that the resonance width depends on temperature, while the center energy of the resonance is considered to be independent of the temperature.

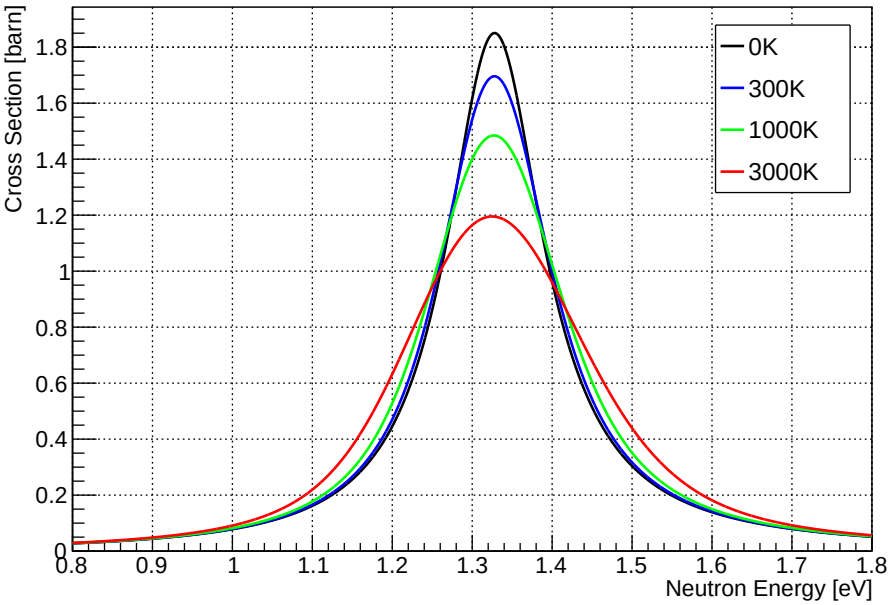

Figure 6.10: Doppler broadening effect. The observed resonance width becomes broader depending on the temperature.

6.4.2 Convolution of neutron energy resolution

As already explained, the neutron energies were calculated from the TOF values. However, the TOF value recorded by the DAQ system was not the true flight time of neutrons from the moderator surface to the target position. The time it takes for neutrons to pass through the moderator must be considered. This time is different for each neutron even if the energy after passing the moderator is the same. This is because the path that each neutron takes inside the moderator is different. The time structure caused by this process affects the energy resolution of the neutron beam, as explained in Chapter 4.

The true energy distribution of neutrons measured at a given TOF value can be calculated using Eqs. (4.2) and (4.3). The true neutron energies are necessarily higher than energies calculated from their TOF values. Therefore, the cross section convoluted with the Ikeda-Carpenter function, $\tilde{\sigma}(E_{\rm n}^{\rm m})$, can be described as

$$\begin{aligned} \tilde{\sigma}(E_{\rm n}^{\rm m}) &= \int dE_{\rm n}\psi(E_{\rm n}, t^{\rm m})\sigma(E_{\rm n})E_{\rm n}^{-\frac{3}{2}} \\ &= \int d\tilde{E}\psi(E_{\rm n}^{\rm m}+\tilde{E}, t^{\rm m})(E_{\rm n}^{\rm m}+\tilde{E})^{-\frac{3}{2}} \quad (\tilde{E}\geq 0), \end{aligned} \tag{6.9}$$

where $\tilde{E}$ is the difference between the true neutron energy and the observed one.

The cross section convoluted with the Doppler broadening effect and the Ikeda-

Carpenter function, $\sigma'(E_{\rm n}^{\rm m})$, can be described as follows;

$$\begin{aligned}
\sigma'(E_{\rm n}^{\rm m}) &= \int d\tilde{E}\psi(E_{\rm n}^{\rm m}+\tilde{E},t^{\rm m})(E_{\rm n}^{\rm m}+\tilde{E})^{-\frac{3}{2}}\frac{1}{\Delta\sqrt{\pi}} \\
&\times \int dE_{\rm cm}\exp\left[-\left(\frac{E_{\rm cm}-(E_{\rm n}^{\rm m}+\tilde{E})}{\Delta}\right)^2\right]\sqrt{\frac{E_{\rm cm}}{E_{\rm n}^{\rm m}+\tilde{E}}}\sigma(E_{\rm cm}), \\
\Delta &= \sqrt{\frac{4(E_{\rm n}^{\rm m}+\tilde{E})k_{\rm B}T}{M/m_{\rm n}}}. \qquad (6.10)
\end{aligned}$$

Figure 6.11 shows an example of a calculation result using Eq. (6.10) for the cross section of the p-wave resonance of ^{117}Sn. The center of the resonance shifts to lower energy by convoluting the Ikeda-Carpenter function.

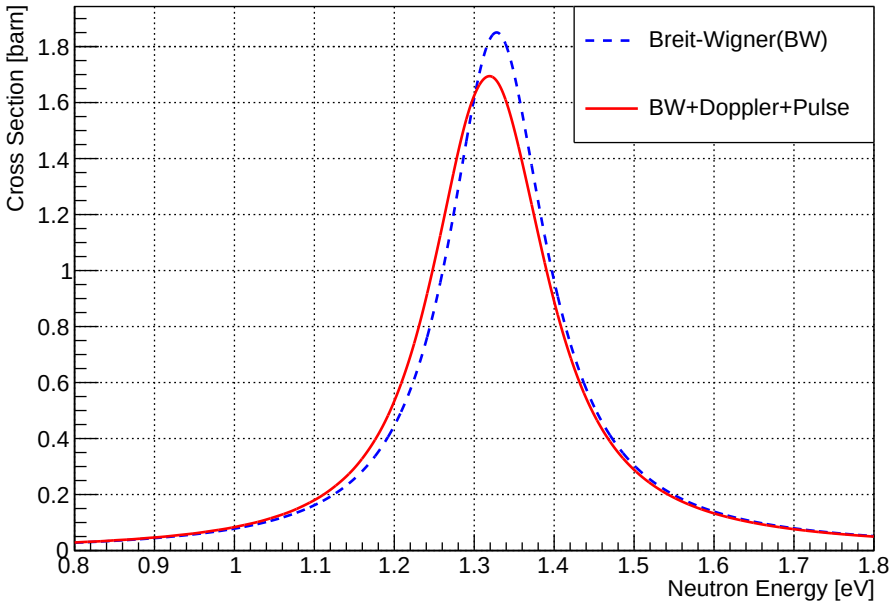

Figure 6.11: Breit-Wigner function convoluted the Doppler broadening effect and neutron energy resolution. The center of the resonance shifts to lower energy by convoluting the Ikeda-Carpenter function.

6.4.3 Self-shielding effect

When the cross section is very large such as an s-wave resonance, the neutron beam cannot reach deeply inside the target. Figure 6.12 shows the distribution of neutron flux inside the target. The horizontal axis is the target thickness and the vertical axis is the energy of incident neutrons. This is a calculation result of the number of neutrons which can pass through a ^{117}Sn target without interactions when 10^5 neutrons with energies around the s-wave resonance are injected. In this calculation, the resonance parameters of the s-wave resonance were used the values

described in Table. 2.3 and the number density of the target as 3.79×10^{23} n/cm^3. The neutron flux inside the target is very small at the resonance energy due to the small transmission. Figure 6.13 shows the distribution of the number of (n,γ) reactions inside the target. The horizontal axis is the target thickness and the vertical axis is the energy of incident neutrons. At the resonance energy, the front surface (target thickness $\sim$ 0.1 mm) is the dominant location where the reaction occurred. On the other hand, the number of reactions is constant entirely inside the target at far energies from the resonance. This indicates that the effective thickness is different between at the center and at the tail of the resonance, which can cause a wider resonance width than the original resonance width as shown in Fig. 6.14.

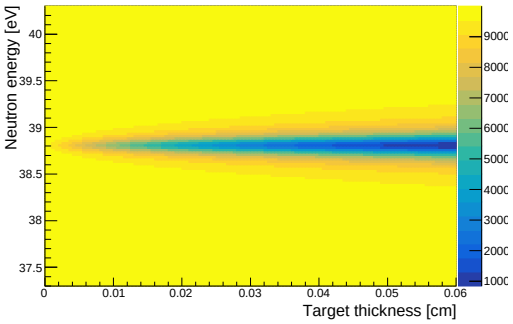

Figure 6.12: Distribution of neutron flux inside the target. The horizontal axis is the target thickness and the vertical axis is the energy of incident neutrons.

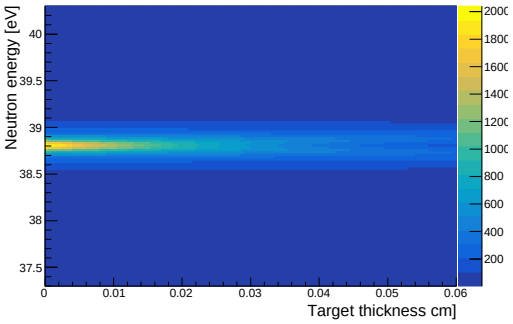

Figure 6.13: Distribution of (n,γ) reactions inside the target. The horizontal axis is the target thickness and the vertical axis is the energy of incident neutrons.

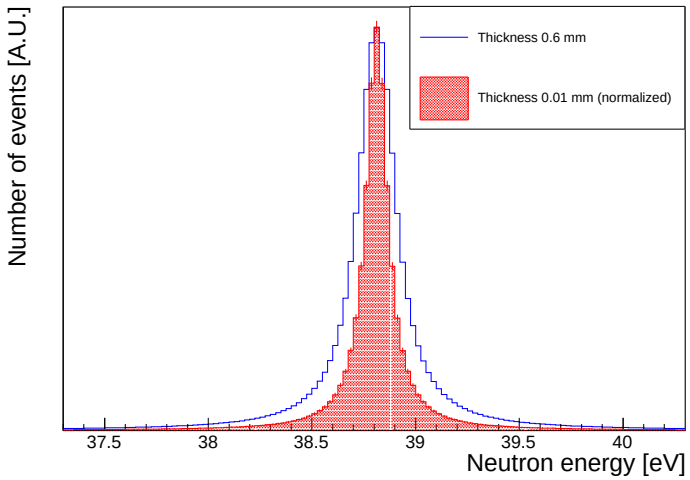

Figure 6.14: Self-shielding effect for the s-wave resonance. The blue-open histogram is the projection as a function of neutron energy of distribution in Fig. 6.13 with the range of the target thickness from 0 to 0.6 mm. The red-shaded histogram is the projection with the range of the target thickness from 0 to 0.01 mm. This red-shaded histogram was scaled so that the maximum heights of both histograms matched. The observed resonance which corresponds to the blue-open histogram has a wider resonance width than the true resonance width due to the self-shielding effect.

The cross-section dependence of the shielding power for the target nucleus must be known. Here, a self-shielding factor $f(\sigma)$ is defined as a function of the cross section σ as

$$f(\sigma) \equiv \frac{N_{\rm entire}}{N_{\rm front}(d/\delta d)} = \frac{N_{\rm incident}\{1-\exp(-n\sigma d)\}}{N_{\rm incident}\{1-\exp(-n\sigma\delta d)\}(d/\delta d)}, \tag{6.11}$$

where $N_{\rm entire}$ and $N_{\rm front}$ are the numbers of reactions occurring in the entire target with a thickness of d and on its front surface with a thickness of δd, respectively. The $N_{\rm incident}$ is the number of incident neutrons and n is the number density of the target. Figure 6.15 shows the self-shielding factor $f(\sigma)$ calculated using the following parameters: $N_{\rm incident} = 10^5$, $n = 3.79 \times 10^{23}$ n/cm^3, $d = 0.6$ mm, and $\delta d = 0.006$ mm. Equation (6.10) is modified as

$$\begin{aligned}\sigma_{\rm obs}(E_{\rm n}^{\rm m}) &= \int d\tilde{E}\psi(E_{\rm n}^{\rm m}+\tilde{E},t^{\rm m})(E_{\rm n}^{\rm m}+\tilde{E})^{-\frac{3}{2}}\frac{1}{\Delta\sqrt{\pi}} \\ &\times \int dE_{\rm cm}\exp\left[-\left(\frac{E_{\rm cm}-(E_{\rm n}^{\rm m}+\tilde{E})}{\Delta}\right)^2\right]\sqrt{\frac{E_{\rm cm}}{E_{\rm n}^{\rm m}+\tilde{E}}}\sigma(E_{\rm cm})f(\sigma(E_{\rm cm})).\end{aligned} \tag{6.12}$$

In the next section, Eq. (6.12) is used as the fitting function.

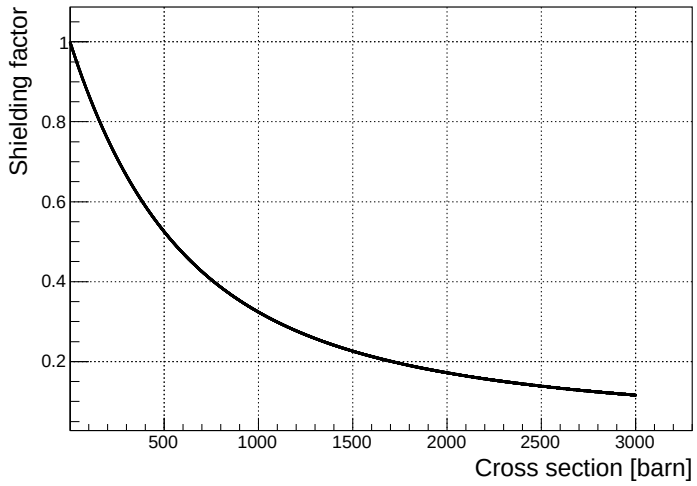

Figure 6.15: Cross-section dependence of self-shielding factor with a ^{117}Sn target thickness as 0.6 mm.

6.4.4 Determination of resonance parameters

The resonance parameters can be determined by fitting the neutron energy spectrum measured with the ^{117}Sn-enriched target. The neutron energy spectrum was gated with $E_\gamma^{\rm m} \geq 2$ MeV in order to exclude γ rays emitted by the transitions from the low-excited state and low-energy background events such as an electric noise. There are background events for $E_\gamma^{\rm m} \geq 2$ MeV, which are caused by the cosmic rays and prompt γ rays emitted by the materials consisting of the detector assembly: aluminum, iron, lithium, and so on. Therefore, the spectrum caused by purely ^{117}Sn(n, γ) reactions can be obtained by subtracting the spectrum measured without the target from one measured with the target. The neutron-energy spectrum after subtraction was corrected and normalized with the methods described in Section 6.3.

The resonance parameters can be obtained by fitting the neutron-energy spectrum which is merged for all detectors using Eq. (6.12). In the vicinity of the p-wave resonance, the cross section $\sigma(E_{\rm cm})$ can be described as

$$\begin{aligned}\sigma(E_{\rm cm}) &= C(\sigma_{s0}(E_{\rm cm}) + \sigma_{\rm p}(E_{\rm cm})) \\ &= C\left(\sqrt{\left|\frac{E_{\rm s0}}{E_{\rm cm}}\right|}\frac{g\Gamma^{\rm n}_{\rm s0}\Gamma^{\gamma}_{\rm s0}}{(E_{\rm cm}-E_{\rm s0})^2+(\Gamma_{\rm s0}/2)^2} + \sqrt{\frac{E_{\rm cm}}{E_{\rm p}}}\frac{g\Gamma^{\rm n}_{\rm p}\Gamma^{\gamma}_{\rm p}}{(E_{\rm cm}-E_{\rm p})^2+(\Gamma_{\rm p}/2)^2}\right),\end{aligned} \tag{6.13}$$

where the index of s0 indicates the negative s-wave resonance and C is a scaling factor. The resonance parameters for the negative s-wave and p-wave resonances were obtained as

$$\Gamma^{\gamma}_{\rm s0} = 77.0 \pm 2.0 \text{ meV}, E_{\rm p} = 1.331 \pm 0.002 \text{ eV}, \text{ and } \Gamma^{\gamma}_{\rm p} = 133 \pm 5 \text{ meV}, \tag{6.14}$$

as shown in Fig. 6.16. Here the negative s-wave resonance energy and both neutron widths were fixed as the central values of previous studies described in Table 2.3.

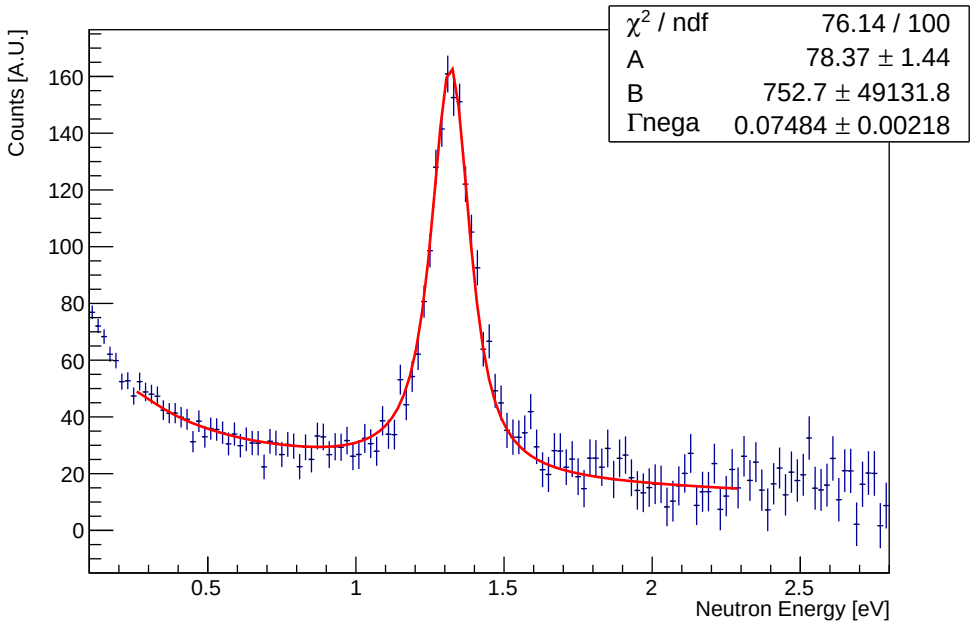

Figure 6.16: Fitting result of the p-wave resonance for determining resonance parameters.

On the other hand, the cross section $\sigma(E_{\rm cm})$ in the vicinity of the s-wave resonance can be described as

$$\begin{aligned} \sigma(E_{\rm cm}) &= C\sigma_{\rm s1}(E_{\rm cm}) \\ &= C\sqrt{\frac{E_{\rm s1}}{E_{\rm cm}}}\frac{g\Gamma^{\rm n}_{\rm s1}\Gamma^{\gamma}_{\rm s1}}{(E_{\rm cm}-E_{\rm s1})^2+(\Gamma_{\rm s1}/2)^2}, \end{aligned} \tag{6.15}$$

where the index of s1 indicates the s-wave resonance. The resonance parameters for the s-wave and p-wave resonances were obtained as

$$E_{\rm s1} = 39.054 \pm 0.005 \text{ eV} \quad \text{and} \quad \Gamma^{\gamma}_{\rm s1} = 31.5 \pm 2.5 \text{ meV}, \tag{6.16}$$

as shown in Fig. 6.17. Here the neutron width $\Gamma^{\rm n}_{\rm s1}$ was fixed as the central value of previous studies described in Table 2.3.

6.5 Determination of relative transition ratios

The transition ratio from the compound state to the ground state is different for each resonance. This implies that the relative intensities of the s-wave resonances to the p-wave resonance are different for the neutron energy spectrum of the single transition by the 9327 keV γ-ray emission and the spectrum of all transitions. The relative transition ratios for the single transition can be determined by fitting the neutron-energy spectrum of the single transition The neutron-energy spectrum measured with the self-filter was gated with the signal regions (the 9327 keV γ-ray peaks and its single- and double-escape peaks). The spectrum was corrected

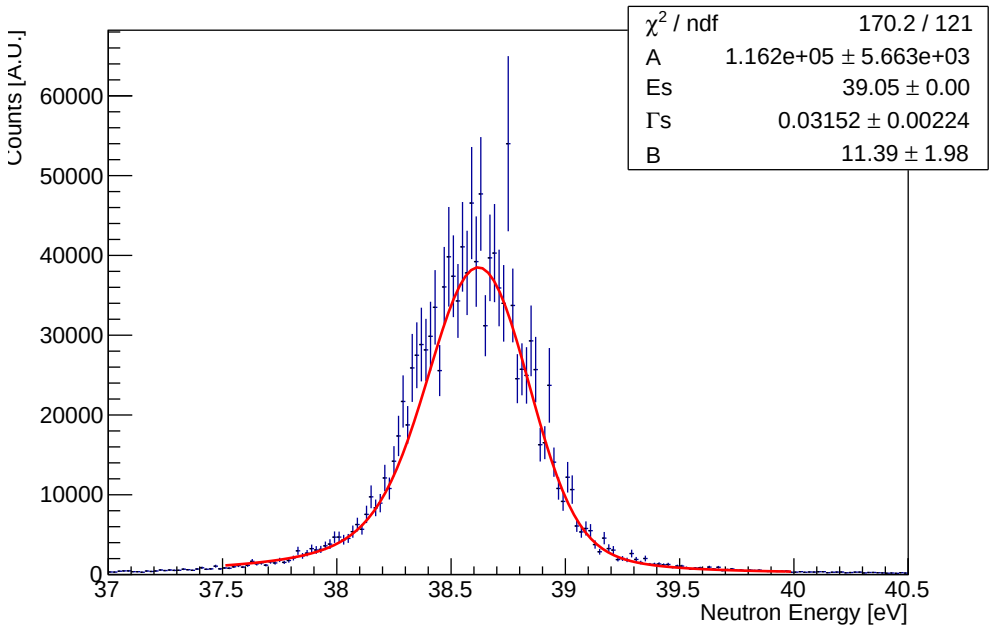

Figure 6.17: Fitting result of the s-wave resonance for determining resonance parameters.

and normalized with the methods described in Section 6.3. The relative transition ratios can be obtained by fitting the neutron-energy spectrum which is merged for all detectors. The cross section with the single transition of the 9327 keV γ-ray emission can be written using the cross section with all transitions as

$$\sigma(E_{\rm cm}) = B_{\rm s0}\sigma_{\rm s0}(E_{\rm cm}) + B_{\rm p}\sigma_{\rm p}(E_{\rm cm}) + B_{\rm s1}\sigma_{\rm s1}(E_{\rm cm}), \tag{6.17}$$

where $B_{\rm s0}$, $B_{\rm p}$, and $B_{\rm s1}$ are the transition ratios of the negative s-wave, the p-wave, and the s-wave resonances, respectively. Cross sections $\sigma_{\rm s0}(E_{\rm cm})$, $\sigma_{\rm p}(E_{\rm cm})$, and $\sigma_{\rm s1}(E_{\rm cm})$ are calculated using the resonance parameters which were determined in Section 6.4.4. The relative transition ratios were obtained by fitting using Eq. (6.12). Here, the cross section $\sigma(E_{\rm cm})$ is calculated using Eq. (6.17). Figures 6.18 and 6.19 show the fitting results around the p-wave and the s-wave resonances, respectively. The relative transition ratios were obtained as

$$\begin{aligned} B_{\rm s0} : B_{\rm p} : B_{\rm s1} &= 2.0 \pm 0.1 : (5.1 \pm 0.2) \times 10^{-1} : (2.6 \pm 0.1) \times 10^{-2} \\ &= 4.0 \pm 0.2 : 1 : (5.1 \pm 0.3) \times 10^{-2}. \end{aligned} \tag{6.18}$$

Table 6.1 summarizes the resonance parameters and relative transition ratios of ^{117}Sn in this work.

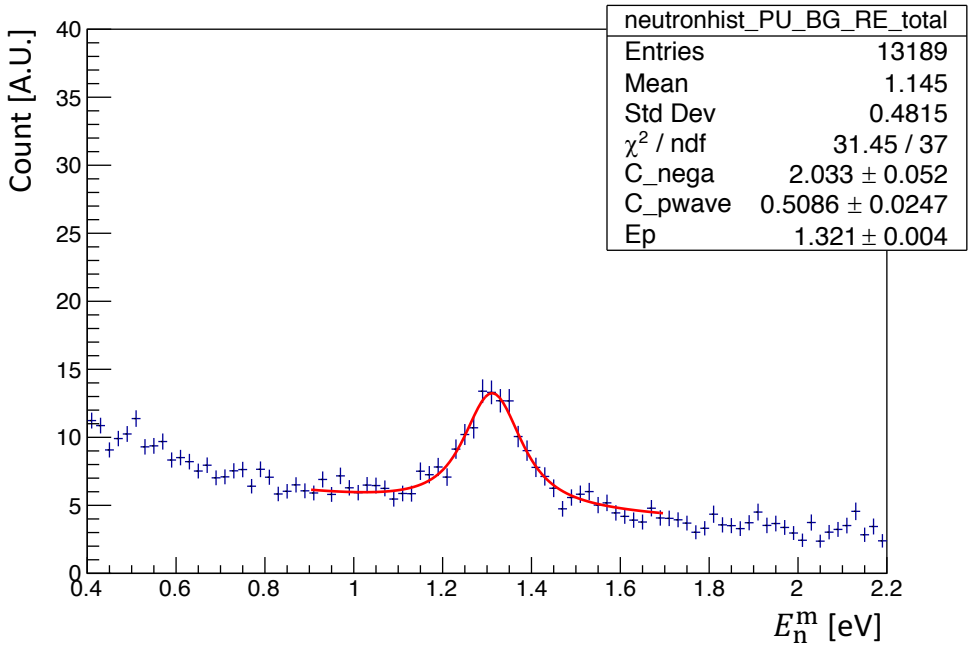

Figure 6.18: Fitting result for determining the relative transition ratios of the negative and the p-wave resonances.

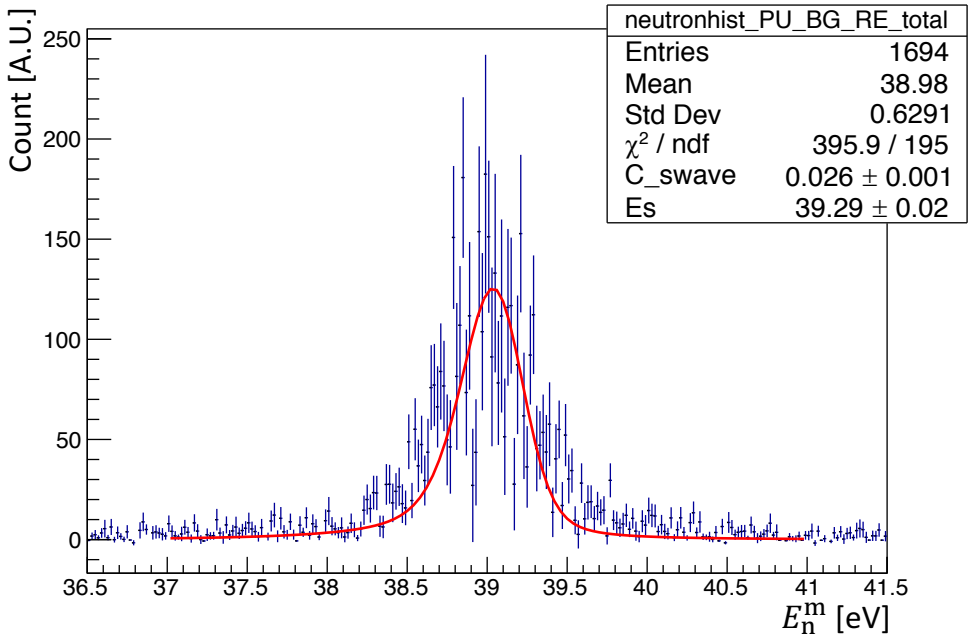

Figure 6.19: Fitting result for determining the relative transition ratio of the s-wave resonance.

Table 6.1: Resonance parameters and relative transition ratios of ^{117}Sn in this work.

E_0 [eV]	J	l	Γ^γ [meV]	$g\Gamma^n$ [meV]	Relative transition ratio
-29.2	1	0	77.0 ± 2.0	29.9	4.0 ± 0.2
1.331 ± 0.002	1	1	133 ± 5	1.38×10^{-4}	1 (unity)
39.054 ± 0.005	1	0	31.5 ± 2.5	3.10	$(5.1 \pm 0.3) \times 10^{-2}$

6.6 Angular dependence of p-wave resonance shape

After the correction and the normalization described in Section 6.3, the neutron energy spectra were summed up at the same polar angle θ_γ. Figure 6.20 shows the neutron energy spectra at the vicinity of the p-wave resonance. The angular dependence of the shape of the p-wave resonance was observed clearly.

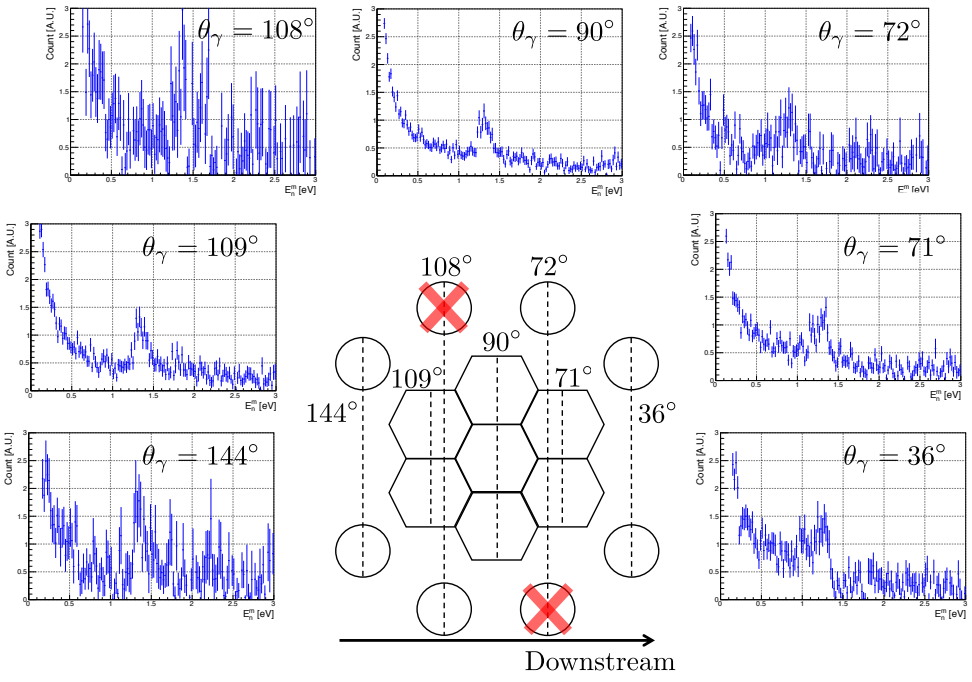

Figure 6.20: Neutron-energy spectrum at the vicinity p-wave resonance of each angle. The central figure represents the setting polar angle θ of each detector. The cross sign indicates the detectors which were not used in this measurement. The angular dependence of the shape of the p-wave resonance was observed clearly.

The asymmetry A_{LH} is calculated based on the definition of Eq. (3.18). The

asymmetry $A_{\rm LH}$ for measurement data is defined as

$$\begin{aligned} A_{\rm LH} &= \frac{N_{\rm L} - N_{\rm H}}{N_{\rm L} + N_{\rm H}}, \\ N_{\rm L} &\equiv \int_{E_{\rm p}-2\Gamma_{\rm p}}^{E_{\rm p}} dE_{\rm n}^{\rm m} N(E_{\rm n}^{\rm m}), \\ N_{\rm H} &\equiv \int_{E_{\rm p}}^{E_{\rm p}+2\Gamma_{\rm p}} dE_{\rm n}^{\rm m} N(E_{\rm n}^{\rm m}), \end{aligned} \tag{6.19}$$

where $N(E_{\rm n}^{\rm m})$ is the number of events at a given neutron energy $E_{\rm n}^{\rm m}$ in the measured spectrum. Figure 6.21 shows the integral ranges for $N_{\rm L}$ and $N_{\rm H}$, respectively. Here the resonance parameters described in Table. 6.1 were used. The angular

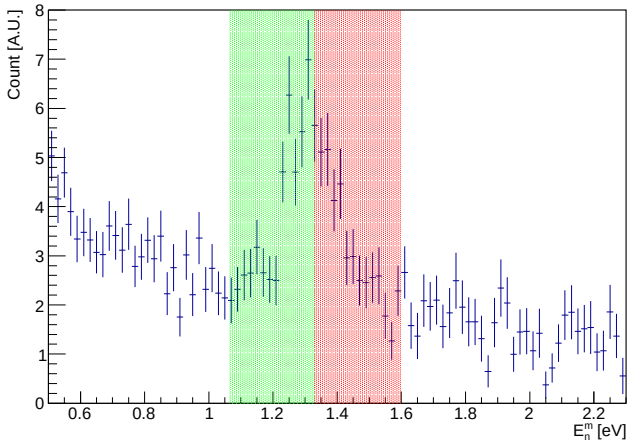

Figure 6.21: Definition of the integral ranges for the asymmetry $A_{\rm LH}$. The green and red bands represent the integral ranges for lower and higher energy regions, respectively.

dependence of $A_{\rm LH}$ is shown in Fig. 6.22. The asymmetry of $A_{\rm LH}$ has a correlation with $\cos\theta_\gamma$ as

$$A_{\rm LH} = A\cos\theta_\gamma + B, \tag{6.20}$$

where

$$A = 0.473 \pm 0.051 \quad \text{and} \quad B = 0.091 \pm 0.019, \tag{6.21}$$

which is a fitting result as shown in Fig. 6.22 and the statistical error of A is 10.8%. According to Eq. (3.21), the angular dependence cannot be fit by a linear function when the contribution of the a_3 term is large. Therefore this fitting result implies the a_3 term is negligible.

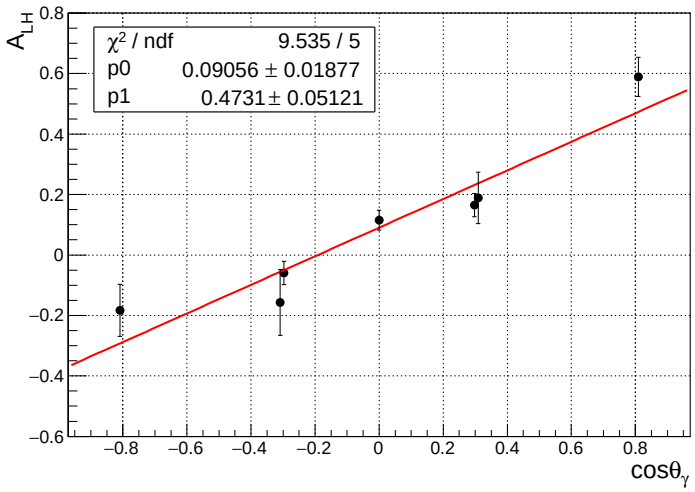

Figure 6.22: Angular dependence of the A_{LH} value. The red solid line is the fitting result with the linear function.

6.7 Estimation of systematic errors

In this section, the origins of systematic errors and estimation of their values are explained.

6.7.1 Range of signal region

Firstly, the uncertainty of the angular dependence of A_{LH} for the ranges of the signal regions was estimated. The range of the signal regions was defined as FWQM which satisfies Eq. (6.1). However, this is arbitrary, and there is no basis for absolute correctness. Therefore, it is confirmed that the uncertainty of the angular dependence of A_{LH} for various ranges of signal regions is defined as

$$h' \geq \frac{1}{N}\left(h_{\mathrm{pk}} - h_{\mathrm{bg}}\right), \tag{6.22}$$

where N is an integer from 2 to 7. Figure 6.23 shows the value of the slope of A_{LH} for each signal region. The systematic error is estimated to be 0.02 (4.3%) which is the difference between the slopes at $N = 4$ and $N = 6$.

6.7.2 Neutron scattering effect inside the nuclear target

The momentum of neutrons captured by the target nuclei is not necessarily parallel to the beam direction because some of them are captured after scattering inside the target. Therefore, the amount of neutrons captured after scattering needs to be estimated. The amount of neutrons captured after backscattering needs to be only estimated because the amounts of neutrons scattered between to φ and to $\varphi + \pi$ directions are the same, and the effect is canceled out when the beam direction is the z direction.

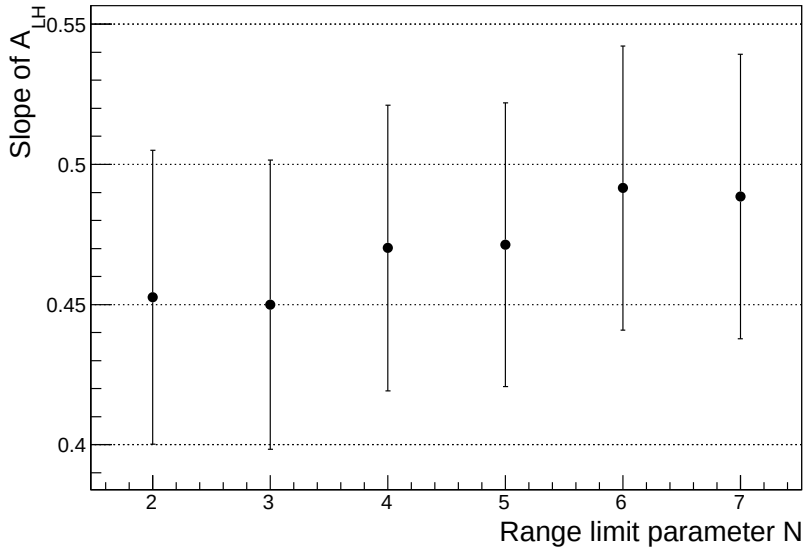

Figure 6.23: Change of angular dependence for ranges of signal regions. The vertical axis is the range limit parameter N. The vertical axis is the slope of $A_{\rm LH}$.

The amount of neutrons captured after backscattering is estimated using a Monte-Carlo simulation. In this simulation, the scattering cross section for $^{\rm nat}$Sn in the epithermal energy region was set to be 4.6 barn which was the sum of the cross sections listed in the JENDL database [48], weighted by the natural abundance of each isotope. The blue-striped histogram in Fig. 6.24 shows the neutron-energy dependence of the ratio of the amount of the capture events after backscattering to all capture events. This asymmetric shape is caused that the relative value of the capture cross section to the scattering cross section changes due to the scattering. Even if the neutron energy changes by the scattering, the change of the TOF value will be negligibly small because the time, until the neutron is captured after backscattering, is at most 2.5 μs. The averaged values of the backscattering ratio in the integral regions for $N_{\rm L}$ and $N_{\rm H}$ are 2.7% and 3.8%, respectively. Thus, the asymmetry $A'_{\rm LH}$ considereing the backscattering is calculated as

$$\begin{aligned} A'_{\rm LH} &= \frac{N'_{\rm L} - N'_{\rm H}}{N'_{\rm L} + N'_{\rm H}} \\ &= \frac{(1-0.027)N_{\rm L} - (1-0.038)N_{\rm H}}{(1-0.027)N_{\rm L} + (1-0.038)N_{\rm H}}. \end{aligned} \tag{6.23}$$

The difference between slopes of $A_{\rm LH}$ and $A'_{\rm LH}$ is estimated to be 0.001 (0.2%), which is much smaller than the statistical error.

6.7.3 Precision of the nuclear target position

The precision of the nuclear target position affects directly the polar angle θ_γ. Figure 6.25 shows the side view of the target and its holder. The maximum

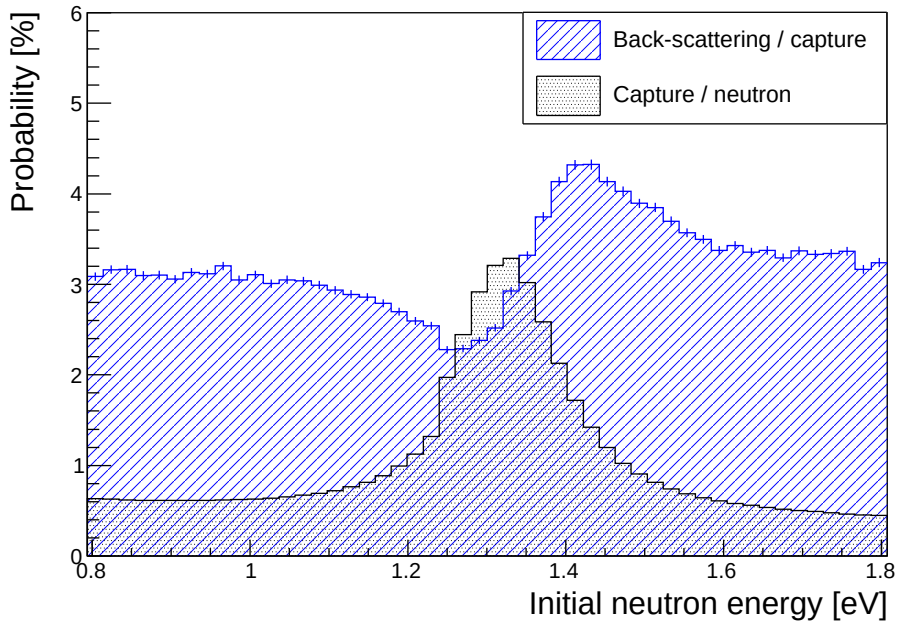

Figure 6.24: Neutron-energy dependence of backscattering ratio. The horizontal axis is the initial neutron energy. The black-hatched histogram is the possibility that a neutron capture reaction occurs. The blue-striped histogram is the ratio of the amount of the capture events after backscattering to all capture events.

deviation of the target position from the center of the detector assembly is $\Delta z = \pm 1$ mm under the assumption that the target is set inside the holder. The deviation of $\Delta z = \pm 1$ mm causes the deviation of polar angle $\Delta\theta_\gamma = \mp 0.3^\circ$ for $\theta_\gamma = 72.7^\circ$. The difference of $A_{\rm LH}$ between with and without the deviation is estimated to be 0.003 (0.6%), which is also much smaller than the statistical error. Table 6.2 summarizes the statistical error and systematic errors for the slope of $A_{\rm LH}$. Finally, the slope of $A_{\rm LH}$ was obtained as

$$A = 0.473 \pm 0.051(\text{stat.}) \pm 0.025(\text{sys.}). \tag{6.24}$$

Table 6.2: Summary of errors for the slope of $A_{\rm LH}$.

	Error	Error [%]
Statistics	0.051	10.8
Range of signal region	0.025	5.3
Back-scattering events	0.001	0.2
Precision of target position	0.003	0.6
Systematic error	0.025	5.3
Total	0.057	12.1

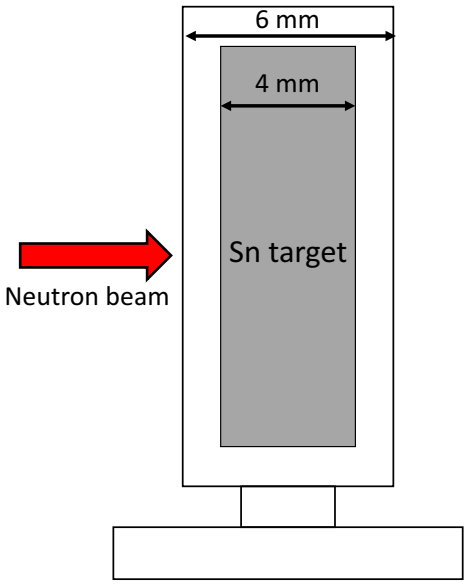

Figure 6.25: Side view of the target and holder.

6.8 Determination of the mixing angle ϕ and the $\kappa(J)$

The slope of the asymmetry $A_{\rm LH}$ can be described as a function of the mixing angle ϕ from Eq. (3.22) using the resonance parameters and the relative transition ratios listed in Table 6.1. The calculated slope $A_{\rm cal}$ is given as

$$\begin{aligned} A_{\rm cal} &= (0.548 \pm 0.003)x - (0.387 \pm 0.002)y \\ &= (0.548 \pm 0.003)\cos\phi - (0.387 \pm 0.002)\sin\phi. \end{aligned} \tag{6.25}$$

Two solutions were obtained from Eqs. (6.24) and (6.25) as

$$\phi = (10.3^{+6.4}_{-7.2})^\circ \ \text{ and } \ \phi = (-80.8^{+7.1}_{-6.4})^\circ. \tag{6.26}$$

Figure 6.26 shows the visualization of these solutions on the xy-plane. The values of x can be obtained as

$$x = 0.98^{+0.01}_{-0.02} \ \text{ and } \ x = 0.16^{+0.12}_{-0.11}. \tag{6.27}$$

The value of W is also obtained from Eq. (2.8) as

$$W = -0.57^{+0.01}_{-0.01}\ \text{meV} \ \text{ and } \ W = -3.5^{+1.5}_{-7.7}\ \text{meV}. \tag{6.28}$$

In this calculation, the value of $A_{\rm L} = 0.79 \times 10^{-2}$ and other parameters in Table 6.1 were used. The absolute value of $\kappa(J)$ was obtained with the error of 1σ as

$$|\kappa(J)| = 0.42^{+0.05}_{-0.06} \ \text{ and } \ |\kappa(J)| = 2.6^{+6.8}_{-1.3}, \tag{6.29}$$

and these are shown in Fig. 6.27.

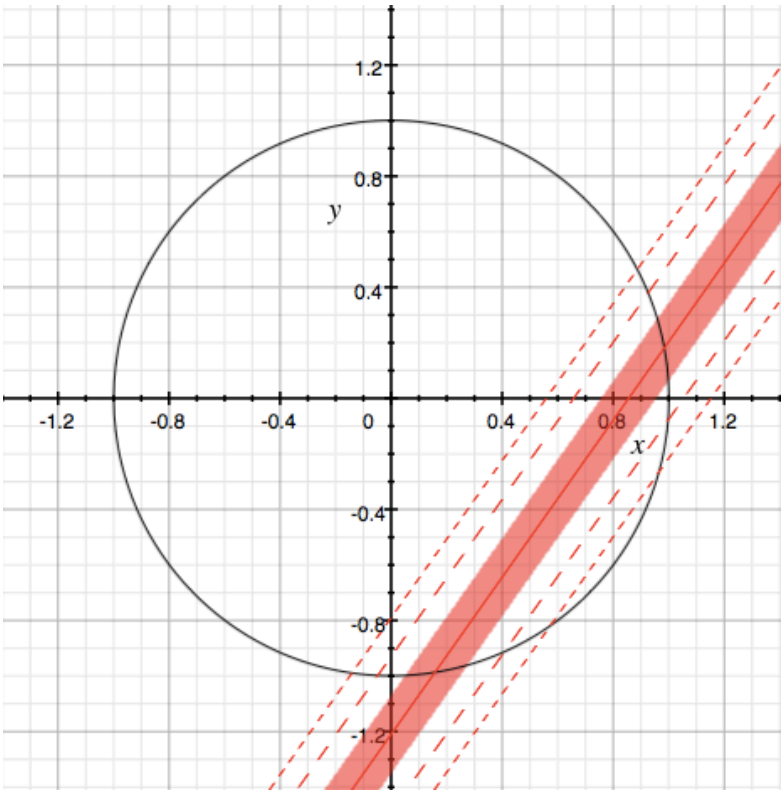

Figure 6.26: Visualization of the ϕ on the xy-plane. The solid line, shaded area, dashed line, and dotted line represents the cental value, 1σ error, 2σ error, and 3σ error, respectively.

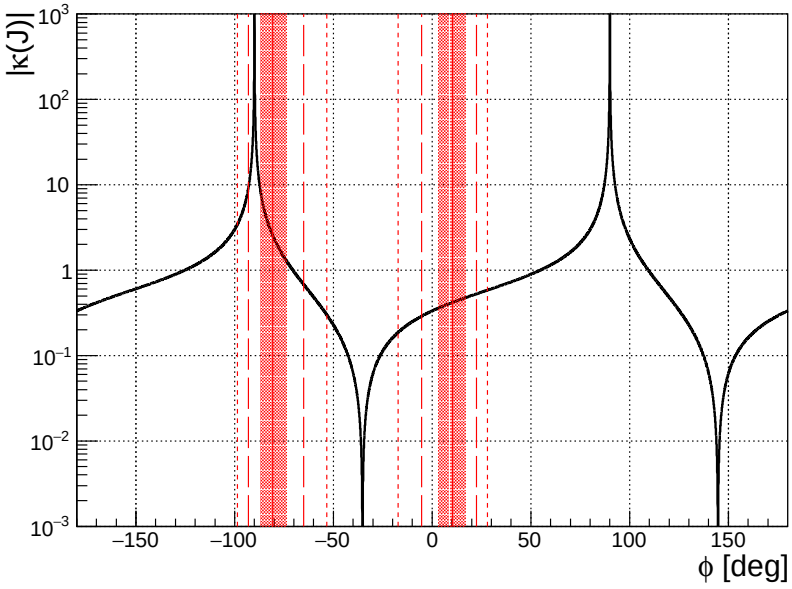

Figure 6.27: The absolute value of $\kappa(J)$ for ^{117}Sn. The solid line, shaded area, dashed line, and dotted line represents the cental value, 1σ error, 2σ error, and 3σ error, respectively.

Chapter 7

Discussion

The value of the mixing angle ϕ was determined in the previous chapter. In this chapter, this result is compared with the previous study. The measurement time to improve the current upper limit for T-violation by the nEDM search is estimated using the result obtained in this study. In addition, future prospects is introduced.

7.1 Comparison with previous study

The angular dependence of the asymmetry A_{LH} is dominated by the contribution of the a_1 term. This result can be compared with the forward-backward asymmetry $\epsilon^{F.B.}$ in the previous study. Figure 7.1 is a drawing of the result of this study (Fig. 6.26) superimposed on the previous result (Fig. 3.5). If $\epsilon^{F.B.}$ was measured with the same precision as this study, they are consistent with each other within 2σ error. These results imply the $\kappa(J)$ is a non-zero value obtained from the a_1 term. In this study, the a_3 term was considered to be negligible. The precise measurement of the a_3 term will allow for a more detailed discussion.

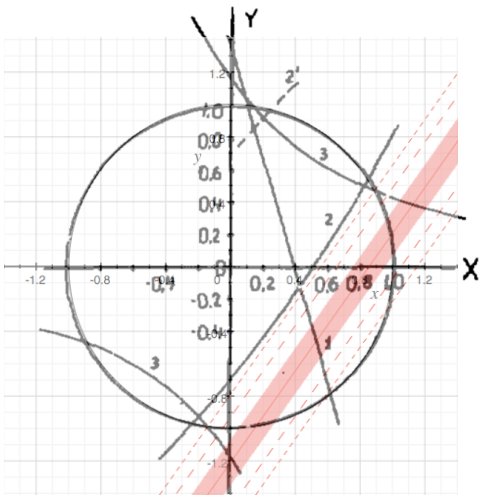

Figure 7.1: Comparison of the value of ϕ with the previous study.

7.2 Estimation of the sensitivity for the T-violation search

The sensitivity of T-violating interaction with ^{117}Sn can be estimated using the formalism described in Chapter 2 because the value of $\kappa(J)$ was determined.

7.2.1 Estimation of the upper limit of $W_{\rm T}/W$

The upper limit of the ratio of the T-violating matrix element ($W_{\rm T}$) to P-violating weak matrix element (W) in the compound nuclear interaction can be estimated using the current upper limit of the nEDM. The ratio of the T-violating cross section ($\Delta\sigma_{\rm T}$) to the P-violating cross section ($\Delta\sigma_{\rm P}$) in the compound nuclear reaction was calculated using the meson-exchange model of EFT by Y. H. Song *et al.* [30]. Assume that the ratio $W_{\rm T}/W$ is equal to $\Delta\sigma_{\rm T}/\Delta\sigma_{\rm P}$ as

$$\frac{W_{\rm T}}{W} = \frac{\Delta\sigma_{\rm T}}{\Delta\sigma_{\rm P}} \simeq (-0.47)\left(\frac{\bar{g}_\pi^{(0)}}{h_\pi^1} + (0.26)\frac{\bar{g}_\pi^{(1)}}{h_\pi^1}\right), \tag{7.1}$$

where h_π^1 is a P-violating coupling constant of meson exchange interaction. The upper limits of $\bar{g}_\pi^{(0)}$ and $\bar{g}_\pi^{(1)}$ are estimated from the current upper limits of nEDM [28] and ^{199}Hg-EDM [72] as

$$\bar{g}_\pi^{(0)} < 1.6\times10^{-10} \quad \text{and} \quad \bar{g}_\pi^{(1)} < 1.7\times10^{-13}. \tag{7.2}$$

The value of h_π^1 was obtained from the measurement of the P-violation in $\mathrm{n}+\mathrm{p}\to\mathrm{d}+\gamma$ reactions [73] as

$$h_\pi^1 = [2.6\pm1.2(\mathrm{stat})\pm0.2(\mathrm{syst})]\times10^{-7}. \tag{7.3}$$

Therefore, the value of $W_{\rm T}/W$ is calculated using Eqs. (7.1), (7.2), and (7.3) as

$$\left|\frac{W_{\rm T}}{W}\right| < 2.9\times10^{-4}. \tag{7.4}$$

The value of $W_{\rm T}$ in Eq. (2.27d) is calculated using Eqs. (6.28) and (7.4).

7.2.2 Estimation of the measurement time using polarized neutrons and polarized target

The most sensitive observable for T-odd observable using polarized neutrons and polarized target can be estimated using Eq. (2.33). The pseudo-magnetic effect caused by the B term in Eq. (2.30) decreases the experimental sensitivity to T-violation. Therefore, it is assumed that this spin rotation is canceled out by applying an external magnetic field, which means $\mathrm{Re}B = 0$. In order to improve the current upper limit of the T-violation by the nEDM search, the errors of A_x and P_x should satisfy the following condition.

$$\sqrt{(\Delta A_x)^2+(\Delta P_x)^2} < \frac{8\mathrm{Re}A^*D}{|A|^2} = \frac{8\mathrm{Re}A^*D}{e^{-n\sigma_{\rm tar}d}}, \tag{7.5}$$

where n, $\sigma_{\rm tar}$, and d are the number density, the total cross section, and the thickness of the target, respectively. The number of incident neutrons is defined as N. The numbers of the transmitted neutrons for plus (minus) polarized neutron-spin polarizer and for plus (minus) polarized analyzer are defined as N_{A+} (N_{A-}) and N_{P+} (N_{P-}), respectively. Then, A_x and ΔA_x can be written as

$$\begin{aligned} A_x &= \frac{N_{A+} - N_{A-}}{N_{A+} + N_{A-}}, \\ \Delta A_x &= \frac{2\sqrt{N_{A+}^2 N_{A-} + N_{A+} N_{A-}^2}}{(N_{A+} + N_{A-})^2}, \end{aligned} \tag{7.6}$$

and P_x and ΔP_x can be written as

$$\begin{aligned} P_x &= \frac{N_{P+} - N_{P-}}{N_{P+} + N_{P-}} \frac{T_{\rm n}}{\sqrt{T_{\rm n}^2 - T_{00}^2}}, \\ \Delta P_x &= \frac{2\sqrt{N_{P+}^2 N_{P-} + N_{P+} N_{P-}^2}}{(N_{P+} + N_{P-})^2} \frac{T_{\rm n}}{\sqrt{T_{\rm n}^2 - T_{00}^2}}, \end{aligned} \tag{7.7}$$

where T_{00} and $T_{\rm n}$ are transmission for the unpolarized and polarized analyzer, respectively. When the neutron polarization is 100%, the value of $T_{\rm n}$ is equal to 1/2. In the case of $N_{A+} = N_{A-} = N_{P+} = N_{P-} = NT_{\rm n}\exp(-n\sigma_{\rm tar}d)$, the error of $A_x + P_x$ is given as

$$\sqrt{(\Delta A_x)^2 + (\Delta P_x)^2} = \sqrt{\frac{2}{Ne^{-n\sigma_{\rm tar}d}}}. \tag{7.8}$$

The number of incident neutrons to improve the upper limit for T-violation can be described using Eqs. (7.5) and (7.8) as

$$N > 4 \times \frac{e^{-n\sigma_{\rm tar}d}}{32{\rm Re}A^* D}. \tag{7.9}$$

For $\phi = 10.3°$ and $-80.8°$, N was obtained under the assumption that the thickness of a 100% ^{117}Sn-enriched target is 5 cm as

$$N = 1.3 \times 10^{13} \ \text{ and } \ N = 1.9 \times 10^{11}. \tag{7.10}$$

NOPTREX collaboration plans to construct a new beamline at BL07 in J-PARC MLF. The intensity of the neutron beam at BL07 with a proton beam power of 1 MW was estimated using Monte-Carlo simulation as 1.7×10^{11} [n/s/cm^2/sr/eV] at 1.26 eV [55]. Assume the following conditions. The distance from the moderator surface to the target position is 15 m. Neutrons emitted from the surface with dimensions of 10×10 cm^2 can reach the target position, which means that the solid angle is about 4.4×10^{-5} sr. The target size is 4×4 cm^2, and the neutron beam at 1.33 ± 0.05 eV is used. The intensity of the neutron beam at 1.33 eV is equal to at 1.26 eV. Therefore, the neutron flux is calculated as 1.2×10^7 n/s.

The measurement time to improve the current upper limit is estimated to be approximately 13 days for $\phi = 10.3°$ and 4.4 hours for $\phi = -80.8°$, respectively.

The above estimation of the measurement time does not consider the polarization of the neutron beam and the target nuclei. The neutron beam is polarized by a neutron-spin polarizer that is a device to polarize the spin of the neutron beam. A ^{3}He spin filter and proton spin filter can polarize epithermal neutrons. Both spin filters make use of a spin-dependent cross section with neutrons. Therefore, an unpolarized neutron beam is polarized as it passes through these spin filters.

The ^{3}He spin filter is composed of ^{3}He gas enclosed into a special glass cell which is made from GE180 or quartz. These materials do not include boron. The ^{3}He nucleus has a very large absorption cross section (10666 barn) when the spin of the neutron is antiparallel to that of ^{3}He nucleus. On the other hand, the cross section for neutrons whose spin is parallel to the spin of ^{3}He nucleus is approximately zero. High-energy neutrons are difficult to polarize because the absorption cross section decreases according to the $1/v$ law. The ^{3}He spin is polarized by Spin-Exchange-Optical-Pumping (SEOP) technique. The electrons of Rb atoms, which are enclosed into the cell, are polarized by the circular polarized light, and the polarization of electrons is transferred into ^{3}He nuclei by the hyperfine interaction. The performance level of the ^{3}He spin filter is evaluated by the polarization and the quantity of ^{3}He gas. The quantity is described by the product of length and pressure. The transmission is written as

$$T_{\rm n} = e^{-\rho\sigma(E_{\rm n})PL}\cosh(\sigma(E_{\rm n})\rho PLP_{\rm He}), \tag{7.11}$$

where ρ is the number density of ^{3}He gas at the standard temperature and pressure, $\sigma(E_{\rm n})$ is the absorption cross section of ^{3}He gas, P is the pressure, L is the length, and $P_{\rm He}$ is the polarization of ^{3}He gas. The polarization of the transmitted neutrons is written as

$$P_{\rm n} = \tanh(\sigma(E_{\rm n})\rho PLP_{\rm He}). \tag{7.12}$$

The figure of merit (FOM) can be defined to optimize the quantity of ^{3}He gas as

$$\mathrm{FOM} \equiv P_{\rm n}^2 T_{\rm n}. \tag{7.13}$$

Figure 7.2 shows the FOM value of the ^{3}He spin filter at 1.33 eV. The FOM value is at the maximum at the quantity of ^{3}He gas of 100 atm $\cdot$ cm for any polarization.

The best performance of ^{3}He spin filter at present was achieved by Z. Salhi *et al.* [74]. In their study, the polarization of 78.5% at the quantity of 41 atm $\cdot$ cm was obtained. Figure 7.3 shows the gas-quantity dependence of $P_{\rm n}$, $T_{\rm n}$, and FOM at 1.33 eV with the polarization of ^{3}He gas of 78.5%. The FOM value can be almost maximized if the quantity of ^{3}He gas of 82 atm $\cdot$ cm is achieved by placing two spin filters developed by Z. Salhi *et al.* in the direction of the neutron beam.

When the polarizations of the neutron beam and the target are not 100%, Eq. (7.5) is modified as

$$\sqrt{(\Delta A_x)^2 + (\Delta P_x)^2} < \frac{8P_{\rm n}P_{\rm l}\mathrm{Re}A^*D}{|A|^2} = \frac{8P_{\rm n}P_{\rm l}\mathrm{Re}A^*D}{e^{-n\sigma_{\rm tar}d}}, \tag{7.14}$$

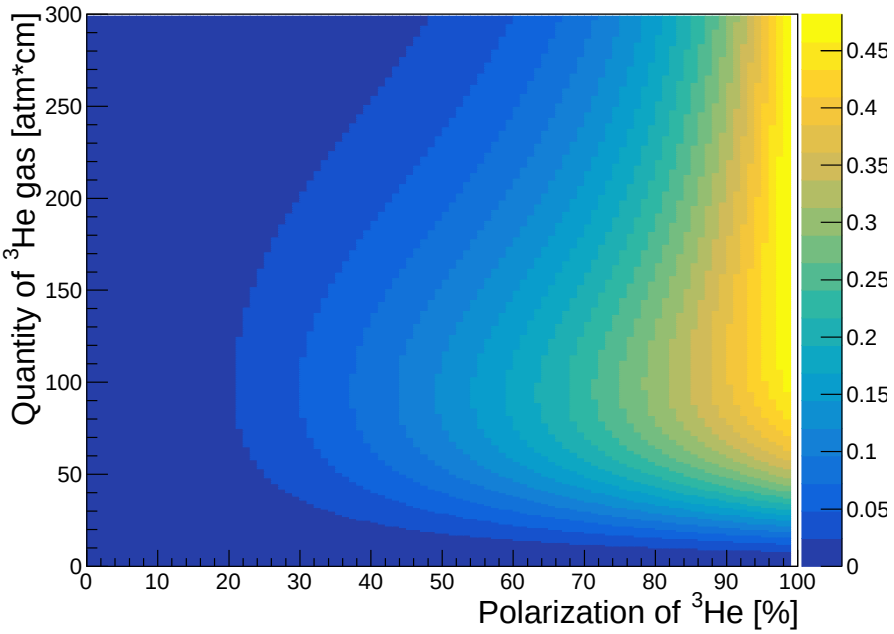

Figure 7.2: FOM of ^{3}He spin filter at neutron energy of 1.33 eV.

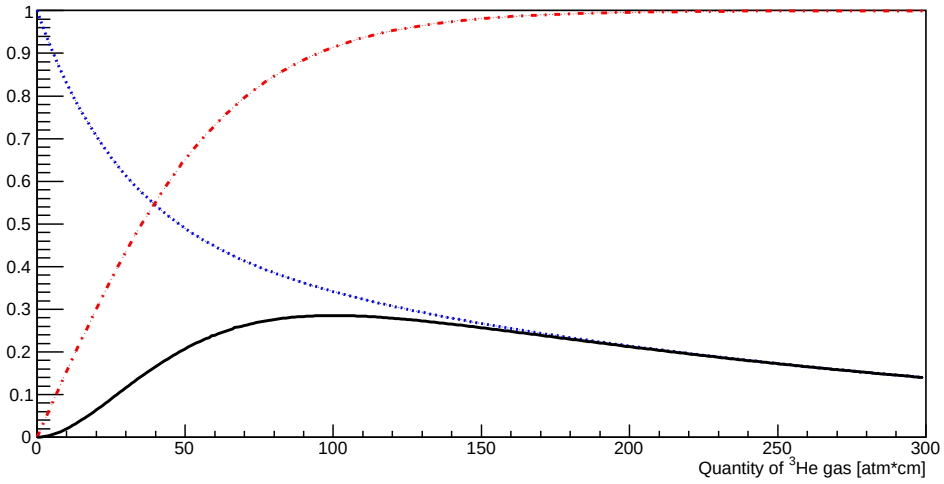

Figure 7.3: Polarization, Transmission, and FOM of ^{3}He spin filter at 78.5% polarization of ^{3}He for neutrons with the energy of 1.33 eV. The red-dashed line corresponds to the polarization. The blue-dotted line corresponds to the transmission. The black-solid line corresponds to FOM.

where $P_{\rm I}$ is the polarization of the target nuclei. In addition, ΔA_x and ΔP_x are modified under the assumption of $N_{A+} = N_{A-} = N_{P+} = N_{P-} = N' T_{\rm n} \exp(-n\sigma_{\rm tar} d)$ as

$$\Delta A_x = \frac{1}{\sqrt{2N' e^{-n\sigma_{\rm tar} d} T_{\rm n}}} \text{ and } \Delta P_x = \frac{1}{\sqrt{2N' e^{-n\sigma_{\rm tar} d} T_{\rm n}}} \frac{T_{\rm n}}{\sqrt{T_{\rm n}^2 - T_{00}^2}}. \tag{7.15}$$

The relationship between N and N' can be written using Eqs. (7.9), (7.14), and (7.15) as

$$\begin{aligned} \frac{N'}{N} &= \frac{f}{P_{\rm I}^2}, \\ f &= \frac{1}{4T_{\rm n} P_{\rm n}^2} \left(1 + \frac{T_{\rm n}^2}{T_{\rm n}^2 - T_{00}^2} \right), \end{aligned} \tag{7.16}$$

where f is a factor which depends on the performance of the spin filter. The value of f is about 2.1 for the quantity of 82 atm $\cdot$ cm at the polarization of ^{3}He gas of 78.5%. This indicates that the measurement time doubles due to the performance of the spin filter. Figure 7.4 shows the measurement time to improve the current upper limit for T-violation. The polarization of ^{117}Sn nuclei is expected to be achieved approximately 20% with the Brute-Force method. This is a method of forcefully polarizing spins in an ultra-high magnetic field ($\sim$ 10 T) and cryogenic environment ($\sim$mK). For $P_{\rm I} = 20\%$, the measurement time is approximately 10 days if $\phi = -80.8°$. From the point of view of statistics, the T-violation search using compound nuclear reactions is feasible.

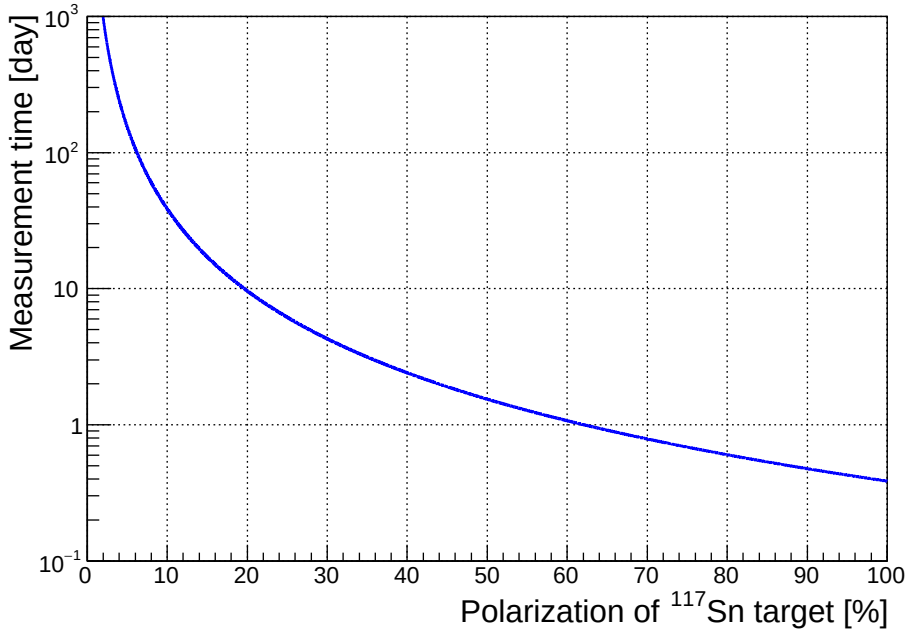

Figure 7.4: Measurement time for polarization of ^{117}Sn target with $\phi = -80.8°$.

7.3 Future prospects

In this study, two values of ϕ were obtained by measuring the angular dependence of the p-wave resonance shape using the unpolarized neutron beam. Since the measurement time to improve the upper limit for T-violation is very different between for the two values, the ϕ value must be uniquely determined. There is a possibility that the measurement of the a_2 term leads to the determination of the unique solution of ϕ. Figure 7.5 shows a calculation result of the a_2 term for both ϕ values which were obtained in this study. The sign of cross section of the a_2 term is different between them. This indicates that the sign of the left-right asymmetry $\epsilon^{L.R.}$ can be determined using the ϕ value.

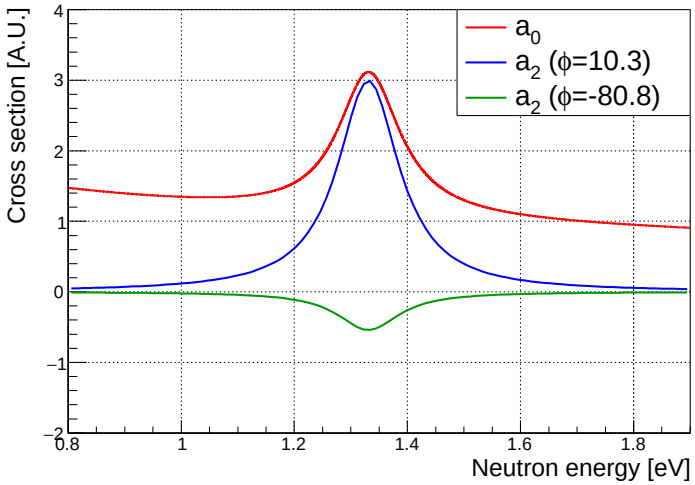

Figure 7.5: Difference of a_2 term between the values of ϕ.

In the previous study, the common solution was not obtained from the measurements of $\epsilon^{L.R.}$ and $\epsilon^{F.B.}$. One of the reasons is considered that the polarization of the neutron beam was not evaluated. Therefore, the $\epsilon^{L.R.}$ must be measured with monitoring the polarization of the neutron beam. For ^{139}La, the measurement of $\epsilon^{L.R.}$ was performed at BL04 in J-PARC MLF by T. Yamamoto *et al.* [75]. The ϕ value can be uniquely determined by measuring the $\epsilon^{L.R.}$ at BL04.

Chapter 8

Conclusion

There is a theoretical prediction that neutron-induced compound nuclei are highly sensitive to T-violation due to the enhancement mechanism. However, the mixing angle ϕ, which is necessary to estimate the sensitivity to T-violation, has not yet been determined in most nuclei. In order to determine the ϕ value for ^{117}Sn, which is a candidate nucleus for T-violation search, the experiment was performed to measure the angular distribution of prompt γ rays from the 1.33 eV p-wave resonance at BL04 in J-PARC MLF with the pulsed neutron beam and the germanium detector assembly. For the transition from the compound state of $^{117}\mathrm{Sn} + \mathrm{n}$ to the ground state of ^{118}Sn, the angular distribution was observed as the angular dependence of the p-wave resonance shape. The angular dependence of the asymmetry A_{LH} was obtained to be $A = 0.473 \pm 0.051(\mathrm{stat.}) \pm 0.025(\mathrm{sys.})$. In addition, the relative transition ratios of the s-wave resonances to the p-wave resonance were determined by the measurement with the self-filter.

The angular dependence of the p-wave resonance shape was analyzed using the theoretical formalism based on interference between the s-wave and the p-wave resonance taken into account the Doppler broadening effect and the energy resolution of the neutron beam. Consequently, the two results were obtained as $|\kappa(J)| = 0.42^{+0.05}_{-0.06}$ for $\phi = (10.3^{+6.4}_{-7.2})^\circ$, $2.6^{+6.8}_{-1.3}$ for $\phi = (-80.8^{+7.1}_{-6.4})^\circ$. The measurement time to improve the current upper limit by the nEDM search was estimated to be approximately 10 days with the 20% polarization of ^{117}Sn in the case of $\phi = -80.8^\circ$. We thus concluded that the nucleus ^{117}Sn is expected to be highly sensitive to T-violation in the compound nuclear reaction.

Appendix A

Spin-dependent scattering length of nucleus

In this appendix, the potential scattering length described in Section 2.3.1 is expressed.

The cross sections of coherent scattering (σ_{coh}) and incoherent scattering (σ_{inc}) can be described using a scattering length b as

$$\sigma_{\mathrm{coh}} = 4\pi \left(\bar{b}\right)^2 \quad \text{and} \quad \sigma_{\mathrm{inc}} = 4\pi\{\bar{b^2} - \left(\bar{b}\right)^2\}, \tag{A.1}$$

where $\bar{b}$ and $\bar{b^2}$ is the average values of b and b^2, respectively. Suppose the system consists of a single isotope with nuclear spin I. The spin of the nucleus-neutron system has the values of $I + 1/2$ or $I - 1/2$. The scattering lengths for the two spin states are denoted by b^+ and b^-. The values of $\bar{b}$ and $\bar{b^2}$ can be described using b^+ and b^- as

$$\bar{b} = \frac{1}{2I+1}\left\{(I+1)b^+ + Ib^-\right\} \quad \text{and} \quad \bar{b^2} = \frac{1}{2I+1}\left\{(I+1)\left(b^+\right)^2 + I\left(b^-\right)^2\right\}. \tag{A.2}$$

The spin-dependent scattering lengths (b^+ and b^-) can be calculated using Eqs. (A.1) and (A.2) as

$$\left(b^+, b^-\right) = \left(\sqrt{\frac{\sigma_{\mathrm{coh}}}{4\pi}} \pm \sqrt{\frac{I}{I+1}\frac{\sigma_{\mathrm{inc}}}{4\pi}}, \sqrt{\frac{\sigma_{\mathrm{coh}}}{4\pi}} \mp \sqrt{\frac{I}{I+1}\frac{\sigma_{\mathrm{inc}}}{4\pi}}\right). \tag{A.3}$$

In the case of ^{117}Sn, the values of σ_{coh} and σ_{inc} are 5.28 barn and 0.3 barn, respectively [76]. Therefore, the values of b^+ and b^- can be obtained using Eq. (A.4) as

$$\left(b^+, b^-\right) = (7.37 \text{ fm}, 3.81 \text{ fm}) \quad \text{or} \quad (5.59 \text{ fm}, 9.16 \text{ fm}). \tag{A.4}$$

The value of potential scattering length a_{s} in Eqs. (2.27a) and (2.27b) corresponds to that of b^+ in Eq. (A.4).

Appendix B

Differential cross section in (n,γ) reaction

According to the Flambaum formalism, the differential cross section of (n,γ) reaction for polarized and unpolarized neutrons can be written as

$$\begin{aligned}
\frac{d\sigma}{d\Omega} &= \frac{1}{2}\Bigg[a_0 + a_1\boldsymbol{k}_\mathrm{n}\cdot\boldsymbol{k}_\gamma + a_2\boldsymbol{\sigma}_\mathrm{n}\cdot(\boldsymbol{k}_\mathrm{n}\times\boldsymbol{k}_\gamma) + a_3\left((\boldsymbol{k}_\mathrm{n}\cdot\boldsymbol{k}_\gamma)^2 - \frac{1}{3}\right) \\
&+ a_4(\boldsymbol{k}_\mathrm{n}\cdot\boldsymbol{k}_\gamma)(\boldsymbol{\sigma}_\mathrm{n}\cdot(\boldsymbol{k}_\mathrm{n}\times\boldsymbol{k}_\gamma)) + a_5(\boldsymbol{\sigma}_\gamma\cdot\boldsymbol{k}_\gamma)(\boldsymbol{\sigma}_\mathrm{n}\cdot\boldsymbol{k}_\gamma) \\
&+ a_6(\boldsymbol{\sigma}_\gamma\cdot\boldsymbol{k}_\gamma)(\boldsymbol{\sigma}_\mathrm{n}\cdot\boldsymbol{k}_\mathrm{n}) + a_7(\boldsymbol{\sigma}_\gamma\cdot\boldsymbol{k}_\gamma)\left((\boldsymbol{\sigma}_\mathrm{n}\cdot\boldsymbol{k}_\gamma)(\boldsymbol{k}_\gamma\cdot\boldsymbol{k}_\mathrm{n}) - \frac{1}{3}(\boldsymbol{\sigma}_\mathrm{n}\cdot\boldsymbol{k}_\mathrm{n})\right) \\
&+ a_8(\boldsymbol{\sigma}_\gamma\cdot\boldsymbol{k}_\gamma)\left((\boldsymbol{\sigma}_\mathrm{n}\cdot\boldsymbol{k}_\mathrm{n})(\boldsymbol{k}_\mathrm{n}\cdot\boldsymbol{k}_\gamma) - \frac{1}{3}(\boldsymbol{\sigma}_\mathrm{n}\cdot\boldsymbol{k}_\gamma)\right) \\
&+ a_9\boldsymbol{\sigma}_\mathrm{n}\cdot\boldsymbol{k}_\gamma + a_{10}\boldsymbol{\sigma}_\mathrm{n}\cdot\boldsymbol{k}_\mathrm{n} + a_{11}\left((\boldsymbol{\sigma}_\mathrm{n}\cdot\boldsymbol{k}_\gamma)(\boldsymbol{k}_\gamma\cdot\boldsymbol{k}_\mathrm{n}) - \frac{1}{3}(\boldsymbol{\sigma}_\mathrm{n}\cdot\boldsymbol{k}_\mathrm{n})\right) \\
&+ a_{12}(\boldsymbol{\sigma}_\mathrm{n}\cdot\boldsymbol{k}_\mathrm{n})\left((\boldsymbol{k}_\mathrm{n}\cdot\boldsymbol{k}_\gamma) - \frac{1}{3}(\boldsymbol{\sigma}_\mathrm{n}\cdot\boldsymbol{k}_\gamma)\right) \\
&+ a_{13}\boldsymbol{\sigma}_\gamma\cdot\boldsymbol{k}_\gamma + a_{14}(\boldsymbol{\sigma}_\gamma\cdot\boldsymbol{k}_\gamma)(\boldsymbol{k}_\mathrm{n}\cdot\boldsymbol{k}_\gamma) \\
&+ a_{15}(\boldsymbol{\sigma}_\gamma\cdot\boldsymbol{k}_\gamma)\boldsymbol{\sigma}_\mathrm{n}\cdot(\boldsymbol{k}_\mathrm{n}\times\boldsymbol{k}_\gamma) + a_{16}(\boldsymbol{\sigma}_\gamma\cdot\boldsymbol{k}_\gamma)\left((\boldsymbol{k}_\mathrm{n}\cdot\boldsymbol{k}_\gamma)^2 - \frac{1}{3}\right) \\
&+ a_{17}(\boldsymbol{\sigma}_\gamma\cdot\boldsymbol{k}_\gamma)(\boldsymbol{k}_\mathrm{n}\cdot\boldsymbol{k}_\gamma)(\boldsymbol{k}_\mathrm{n}\cdot(\boldsymbol{k}_\mathrm{n}\times\boldsymbol{k}_\gamma))\Bigg], \qquad \text{(B.1)}
\end{aligned}$$

where $\boldsymbol{k}_\mathrm{n}$ is a unit vector parallel to the incident neutron momentum, $\boldsymbol{k}_\gamma$ is a unit vector parallel to the emitted γ-ray momentum, $\boldsymbol{\sigma}_\mathrm{n}$ is a unit vector parallel to the incident neutron spin, and $\boldsymbol{\sigma}_\gamma$ is a unit vector parallel to the emitted γ-ray spin.

The angular correlation terms (a_0 to a_{17}) can be described using amplitudes of (n,γ) reaction (V_1 to V_4) as

$$\begin{aligned}
a_0 &= \sum_{J_\mathrm{s}}|V_1(E_\mathrm{n},J_\mathrm{s})|^2 + \sum_{J_{\mathrm{p},j}}|V_2(E_\mathrm{n},J_\mathrm{p})|^2, \\
a_1 &= 2\,\mathrm{Re}\sum_{J_\mathrm{s},J_\mathrm{p},j} V_1(E_\mathrm{n},J_\mathrm{s})V_2^*(E_\mathrm{n},J_\mathrm{p})P(J_\mathrm{s}J_\mathrm{p}\frac{1}{2}j1IF)z_j,
\end{aligned}$$

$$
\begin{aligned}
a_2 &= -2\,\mathrm{Im}\sum_{J_\mathrm{s},J_\mathrm{p},j} V_1(E_\mathrm{n},J_\mathrm{s})V_2^*(E_\mathrm{n},J_\mathrm{p})\beta_j P(J_\mathrm{s}J_\mathrm{p}\frac{1}{2}j1IF)z_j,\\
a_3 &= 3\sqrt{10}\,\mathrm{Re}\sum_{J_\mathrm{p},j,J'_\mathrm{p},j'} V_2(E_\mathrm{n},J_\mathrm{p})V_2^*(E_\mathrm{n},J'_\mathrm{p})P(J_\mathrm{p}J'_\mathrm{p}jj'2IF)z_jz_{j'}\begin{Bmatrix}2&1&1\\0&\frac{1}{2}&\frac{1}{2}\\2&j&j'\end{Bmatrix},\\
a_4 &= -6\sqrt{5}\,\mathrm{Im}\sum_{J_\mathrm{p},j,J'_\mathrm{p},j'} V_2(E_\mathrm{n},J_\mathrm{p})V_2^*(E_\mathrm{n},J'_\mathrm{p})P(J_\mathrm{p}J'_\mathrm{p}jj'2IF)z_jz_{j'}\begin{Bmatrix}2&1&1\\1&\frac{1}{2}&\frac{1}{2}\\2&j&j'\end{Bmatrix},\\
a_5 &= -\mathrm{Re}\sum_{J_\mathrm{s},J'_\mathrm{s}} V_1(E_\mathrm{n},J_\mathrm{s})V_1^*(E_\mathrm{n},J'_\mathrm{s})P(J_\mathrm{s}J'_\mathrm{s}\frac{1}{2}\frac{1}{2}1IF)\\
&\quad -6\,\mathrm{Re}\sum_{J_\mathrm{p},j,J'_\mathrm{p},j'} V_2(E_\mathrm{n},J_\mathrm{p})V_2^*(E_\mathrm{n},J'_\mathrm{p})P(J_\mathrm{p}J'_\mathrm{p}jj'1IF)z_jz_{j'}\begin{Bmatrix}0&1&1\\1&\frac{1}{2}&\frac{1}{2}\\1&j&j'\end{Bmatrix},\\
a_6 &= -2\,\mathrm{Re}\sum_{J_\mathrm{s},J_\mathrm{p}} V_1(E_\mathrm{n},J_\mathrm{s})V_2^*(E_\mathrm{n},J_\mathrm{p},\frac{1}{2})\delta_{J_\mathrm{s}J_\mathrm{p}},\\
a_7 &= \sqrt{3}\,\mathrm{Re}\sum_{J_\mathrm{s},J_\mathrm{p}} V_1(E_\mathrm{n},J_\mathrm{s})V_2^*(E_\mathrm{n},J_\mathrm{p},\frac{3}{2})P(J_\mathrm{s}J_\mathrm{p}\frac{1}{2}\frac{3}{2}2IF),\\
a_8 &= -18\,\mathrm{Re}\sum_{J_\mathrm{p},j,J'_\mathrm{p},j'} V_2(E_\mathrm{n},J_\mathrm{p})V_2^*(E_\mathrm{n},J'_\mathrm{p})P(J_\mathrm{p}J'_\mathrm{p}jj'1IF)z_jz_{j'}\begin{Bmatrix}2&1&1\\1&\frac{1}{2}&\frac{1}{2}\\2&j&j'\end{Bmatrix},\\
a_9 &= -2\,\mathrm{Re}\sum_{J_\mathrm{s},J'_\mathrm{s}} V_1(E_\mathrm{n},J_\mathrm{s})V_3^*(E_\mathrm{n},J'_\mathrm{s})P(J_\mathrm{s}J'_\mathrm{s}\frac{1}{2}\frac{1}{2}1IF)\\
&\quad -12\,\mathrm{Re}\sum_{J_\mathrm{p},j,J'_\mathrm{p},j'} V_2(E_\mathrm{n},J_\mathrm{p})V_4^*(E_\mathrm{n},J'_\mathrm{p})P(J_\mathrm{p}J'_\mathrm{p}jj'1IF)z_jz_{j'}\begin{Bmatrix}0&1&1\\1&\frac{1}{2}&\frac{1}{2}\\1&j&j'\end{Bmatrix},\\
a_{10} &= -2\,\mathrm{Re}\sum_{J_\mathrm{s}}[V_2(E_\mathrm{n},J_\mathrm{p},\frac{1}{2})V_3^*(E_\mathrm{n},J_\mathrm{s})+V_1(E_\mathrm{n},J_\mathrm{s})V_4^*(E_\mathrm{n},J_\mathrm{p},\frac{1}{2})]\delta_{J_\mathrm{s}J_\mathrm{p}},\\
a_{11} &= \sqrt{3}\,\mathrm{Re}\sum_{J_\mathrm{s},J_\mathrm{p}}[V_2(E_\mathrm{n},J_\mathrm{p},\frac{3}{2})V_3^*(E_\mathrm{n},J_\mathrm{s})+V_1(E_\mathrm{n},J_\mathrm{s})V_4^*(E_\mathrm{n},J_\mathrm{p},\frac{3}{2})]P(J_\mathrm{s}J_\mathrm{p}\frac{1}{2}\frac{3}{2}2IF),\\
a_{12} &= -36\,\mathrm{Im}\sum_{J_\mathrm{p},J'_\mathrm{p},j,j'} V_2(E_\mathrm{n},J_\mathrm{p})V_4^*(E_\mathrm{n},J'_\mathrm{p})P(J_\mathrm{p}J'_\mathrm{p}jj'1IF)z_jz_{j'}\begin{Bmatrix}2&1&1\\1&\frac{1}{2}&\frac{1}{2}\\1&j&j'\end{Bmatrix},\\
a_{13} &= 2\,\mathrm{Re}\sum_{J_\mathrm{s}} V_1(E_\mathrm{n},J_\mathrm{s})V_3^*(E_\mathrm{n},J_\mathrm{s})+2\,\mathrm{Re}\sum_{J_\mathrm{p}} V_2(E_\mathrm{n},J_\mathrm{p})V_4^*(E_\mathrm{n},J_\mathrm{p})z_jz_j,\\
a_{14} &= 2\,\mathrm{Re}\sum_{J_\mathrm{s},J_\mathrm{p},j}[V_2(E_\mathrm{n},J_\mathrm{p})V_3^*(E_\mathrm{n},J_\mathrm{s})z_j+V_1(E_\mathrm{n},J_\mathrm{s})V_4^*(E_\mathrm{n},J_\mathrm{p})z_j]P(J_\mathrm{s}J_\mathrm{p}\frac{1}{2}j1IF),\\
a_{15} &= 2\,\mathrm{Im}\sum_{J_\mathrm{s},J_\mathrm{p},j} V_2(E_\mathrm{n},J_\mathrm{p})V_3^*(E_\mathrm{n},J_\mathrm{s})z_j-V_1(E_\mathrm{n},J_\mathrm{s})V_4^*(E_\mathrm{n},J_\mathrm{p})z_j]\beta_jP(J_\mathrm{s}J_\mathrm{p}\frac{1}{2}j1IF),
\end{aligned}
$$

$$
\begin{aligned}
a_{16} &= 6\sqrt{10}\,\mathrm{Re}\sum_{J_\mathrm{p},j,J'_\mathrm{p},j'} V_2(E_\mathrm{n},J_\mathrm{p})V_4^*(E_\mathrm{n},J'_\mathrm{p})P(J_\mathrm{p}J'_\mathrm{p}jj'2IF)z_jz_{j'}\begin{Bmatrix}2&1&1\\0&\frac{1}{2}&\frac{1}{2}\\1&j&j'\end{Bmatrix},\\
a_{17} &= -12\sqrt{5}\,\mathrm{Im}\sum_{J_\mathrm{p},j,J'_\mathrm{p},j'} V_2(E_\mathrm{n},J_\mathrm{p})V_4^*(E_\mathrm{n},J'_\mathrm{p})P(J_\mathrm{p}J'_\mathrm{p}jj'2IF)z_jz_{j'}\begin{Bmatrix}2&1&1\\1&\frac{1}{2}&\frac{1}{2}\\1&j&j'\end{Bmatrix}.
\end{aligned}
\tag{B.2}
$$

Here the amplitudes V_1 to V_4 are given as

$$
\begin{aligned}
V_1(E_\mathrm{n},J_\mathrm{s}) &= -\frac{1}{2k}\sum_\mathrm{s}\frac{\sqrt{g_\mathrm{s}\Gamma^\mathrm{n}_\mathrm{s}\Gamma^\gamma_{\mathrm{s},f}}}{E_\mathrm{n}-E_\mathrm{s}+i\Gamma_\mathrm{s}/2},\\
V_2(E_\mathrm{n},J_\mathrm{p}) &= -\frac{1}{2k}\sum_\mathrm{p}\frac{\sqrt{g_\mathrm{p}\Gamma^\mathrm{n}_\mathrm{p}\Gamma^\gamma_{\mathrm{p},f}}}{E_\mathrm{n}-E_\mathrm{p}+i\Gamma_\mathrm{p}/2},\\
V_3(E_\mathrm{n},J_\mathrm{s}=J_\mathrm{p}) &= -\frac{1}{2k}\sum_{\mathrm{s,p}}\frac{\sqrt{g_\mathrm{s}\Gamma^\mathrm{n}_\mathrm{s}}W\sqrt{\Gamma^\gamma_{\mathrm{p},f}}}{(E_\mathrm{n}-E_\mathrm{p}+i\Gamma_\mathrm{p}/2)(E_\mathrm{n}-E_\mathrm{s}+i\Gamma_\mathrm{s}/2)},\\
V_4(E_\mathrm{n},J_\mathrm{p}=J_\mathrm{s}) &= -\frac{1}{2k}\sum_{\mathrm{s,p}}\frac{\sqrt{g_\mathrm{p}\Gamma^\mathrm{n}_\mathrm{p}}W\sqrt{\Gamma^\gamma_{\mathrm{s},f}}}{(E_\mathrm{n}-E_\mathrm{s}+i\Gamma_\mathrm{s}/2)(E_\mathrm{n}-E_\mathrm{p}+i\Gamma_\mathrm{p}/2)},
\end{aligned}
\tag{B.3}
$$

where k is the momentum of the neutron, E_n is the kinetic energy of the neutron, E_r is the resonance energy of a neutron resonance r, Γ^n_r is the neutron width, $\Gamma^\gamma_{r,f}$ is the partial γ width of the transition to a final state f, and W is the weak matrix element. Here, the statistical factor g_r is described as

$$
g_r = \frac{2J_r+1}{2(2I+1)},
\tag{B.4}
$$

where I is the nuclear spin and J_r is the total spin of the compound state of the resonance r. The factor P is given as

$$
\begin{aligned}
P(JJ'jj'kIF) &= (-1)^{J+J'+j'+I+F}\frac{3}{2}\sqrt{(2J+1)(2J'+1)(2j+1)(2j'+1)}\\
&\times \begin{Bmatrix}k&j&j'\\I&J'&J\end{Bmatrix}\begin{Bmatrix}k&1&1\\F&J&J'\end{Bmatrix},
\end{aligned}
\tag{B.5}
$$

where J, j, I, and F are the spin of the compound state, the total angular momentum of the neutron, the spin of target nuclei, and the spin of a final state, respectively. The coefficient z_j is given as

$$
z_j = \begin{cases} x=\cos\phi & (j=\frac{1}{2})\\ y=\sin\phi & (j=\frac{3}{2}).\end{cases}
\tag{B.6}
$$

The a_{10} term in Eq. (B.2) corresponds to the helicity dependence of the neutron-capture cross section, and the longitudinal asymmetry $A_{\rm L}$ of Eq. (2.5) is derived from the a_{10} term. When the interference between an s-wave and a p-wave amplitudes is considered, the ratio of the P-violating cross section a_{10} to the p-wave cross section $a_{0,\rm p}$ is given as

$$\begin{aligned}\frac{a_{10}}{a_{0,\rm p}} &= \frac{-2x{\rm Re}(V_2(E_{\rm n},J_{\rm p})V_3^*(E_{\rm n},J_{\rm s}=J_{\rm p})+V_1(E_{\rm n},J_{\rm s})V_4^*(E_{\rm n},J_{\rm p}=J_{\rm s}))}{|V_2(E_{\rm n},J_{\rm p})|^2} \\ &= \frac{-2xW}{(E_{\rm n}-E_{\rm s})^2+(\Gamma_{\rm s}/2)^2}\sqrt{\frac{\Gamma_{\rm s}^{\rm n}}{\Gamma_{\rm p}^{\rm n}}}\left\{(E_{\rm n}-E_{\rm s})+\frac{\Gamma_{{\rm s},f}^{\gamma}}{\Gamma_{{\rm p},f}^{\gamma}}\right\}. \qquad \text{(B.7)}\end{aligned}$$

For $E_{\rm n}=E_{\rm p}$ and $E_{\rm p}-E_{\rm s}\gg\Gamma_{\rm s}$, Eq. (B.7) can be written as

$$\frac{a_{10}}{a_{0,\rm p}}\simeq-\frac{2xW}{E_{\rm p}-E_{\rm s}}\sqrt{\frac{\Gamma_{\rm s}^{\rm n}}{\Gamma_{\rm p}^{\rm n}}}=A_{\rm L}. \qquad \text{(B.8)}$$

References

[1] T. D. Lee and C. N. Yang, Question of Parity Conservation in Weak Interactions, Phys. Rev. **104**, 254 (1956).

[2] C. S. Wu, E. Ambler, R. W. Hayward, D. D. Hoppes, and R. P. Hudson, Experimental Test of Parity Conservation in Beta Decay, Phys. Rev. **105**, 1413 (1957).

[3] J. H. Christenson, J. W. Cronin, V. L. Fitch, and R. Turlay, EVIDENCE FOR THE 2π DECAY OF THE K_2^0 MESON, Phys. Rev. Lett. **13**, 138 (1964).

[4] **Belle Collaboration**, K. Abe *et al.*, Observation of Large *CP* Violation in the Neutral B Meson System, Phys. Rev. Lett. **87**, 091802 (2001).

[5] **BABAR Collaboration**, B. Aubert *et al.*, Observation of *CP* Violation in the B^0 Meson System, Phys. Rev. Lett. **87**, 091801 (2001).

[6] M. Kobayashi and T. Maskawa, CP-Violation in the Renormalizable Theory of Weak Interaction, Progress of Theoretical Physics **49**, 652 (1973).

[7] P. D. Group *et al.*, Review of Particle Physics, Progress of Theoretical and Experimental Physics **2020** (2020), 083C01.

[8] G. R. Farrar and M. E. Shaposhnikov, Baryon asymmetry of the Universe in the standard model, Phys. Rev. D **50**, 774 (1994).

[9] A. Sakharov, Violation of CP invariance, C asymmetry, and baryon asymmetry of the universe, JETP **5**, 24 (1967).

[10] J. Schwinger, On Gauge Invariance and Vacuum Polarization, Phys. Rev. **82**, 664 (1951).

[11] J. Schwinger, The Theory of Quantized Fields. II, Phys. Rev. **91**, 713 (1953).

[12] M. Pospelov and A. Ritz, Electric dipole moments as probes of new physics, Annals of Physics **318**, 119 (2005), Special Issue.

[13] M. J. Ramsey-Musolf, Nuclear Science and the New Standard Model, Nuclear Physics A **805**, 137c (2008), INPC 2007.

[14] J. H. Smith, E. M. Purcell, and N. F. Ramsey, Experimental Limit to the Electric Dipole Moment of the Neutron, Phys. Rev. **108**, 120 (1957).

[15] P. D. Miller, W. B. Dress, J. K. Baird, and N. F. Ramsey, Limit to the Electric Dipole Moment of the Neutron, Phys. Rev. Lett. **19**, 381 (1967).

[16] W. B. Dress, J. K. Baird, P. D. Miller, and N. F. Ramsey, Upper Limit for the Electric Dipole Moment of the Neutron, Phys. Rev. **170**, 1200 (1968).

[17] J. K. Baird, P. D. Miller, W. B. Dress, and N. F. Ramsey, Improved Upper Limit to the Electric Dipole Moment of the Neutron, Phys. Rev. **179**, 1285 (1969).

[18] W. B. Dress, P. D. Miller, and N. F. Ramsey, Improved Upper Limit for the Electric Dipole Moment of the Neutron, Phys. Rev. D **7**, 3147 (1973).

[19] W. B. Dress, P. D. Miller, J. M. Pendlebury, P. Perrin, and N. F. Ramsey, Search for an electric dipole moment of the neutron, Phys. Rev. D **15**, 9 (1977).

[20] I. Altarev *et al.*, A search for the electric dipole moment of the neutron using ultracold neutrons, Nuclear Physics A **341**, 269 (1980).

[21] I. Altarev *et al.*, A new upper limit on the electric dipole moment of the neutron, Physics Letters B **102**, 13 (1981).

[22] J. Pendlebury *et al.*, Search for a neutron electric dipole moment, Physics Letters B **136**, 327 (1984).

[23] K. Smith *et al.*, A search for the electric dipole moment of the neutron, Physics Letters B **234**, 191 (1990).

[24] I. Altarev *et al.*, New measurement of the electric dipole moment of the neutron, Physics Letters B **276**, 242 (1992).

[25] P. G. Harris *et al.*, New Experimental Limit on the Electric Dipole Moment of the Neutron, Phys. Rev. Lett. **82**, 904 (1999).

[26] C. A. Baker *et al.*, Improved Experimental Limit on the Electric Dipole Moment of the Neutron, Phys. Rev. Lett. **97**, 131801 (2006).

[27] A. P. Serebrov *et al.*, New search for the neutron electric dipole moment with ultracold neutrons at ILL, Phys. Rev. C **92**, 055501 (2015).

[28] C. Abel *et al.*, Measurement of the Permanent Electric Dipole Moment of the Neutron, Phys. Rev. Lett. **124**, 081803 (2020).

[29] N. Bohr, Neutron Capture and Nuclear Constitution, 1936.

[30] Y.-H. Song, R. Lazauskas, and V. Gudkov, Time reversal invariance violation in neutron-deuteron scattering, Phys. Rev. C **83**, 065503 (2011).

[31] C.-P. Liu and R. G. E. Timmermans, P- and T-odd two-nucleon interaction and the deuteron electric dipole moment, Phys. Rev. C **70**, 055501 (2004).

[32] D. Nagle *et al.*, High-Energy Physics with Polarized Beams and Polarized Targets, in *AIP Conference Proceedings*, 1978.

[33] R. Balzer *et al.*, Parity violation in proton-proton scattering at 45 MeV, Phys. Rev. C **30**, 1409 (1984).

[34] P. von Rossen, U. von Rossen, and H. E. Conzett, Test of parity conservation in pp scattering at 46 MeV, in *AIP Conference Proceedings*, volume 69, pp. 1442–1445, 1984.

[35] **TRIUMF E497 Collaboration**, A. R. Berdoz *et al.*, Parity Violation in Proton-Proton Scattering at 221 MeV, Phys. Rev. Lett. **87**, 272301 (2001).

[36] V. Yuan *et al.*, Measurement of Parity Nonconservation in the Proton-Proton Total Cross Section at 800 MeV, Phys. Rev. Lett. **57**, 1680 (1986).

[37] D. P. Grosnick *et al.*, Measurement of the differences in the total cross section for antiparallel and parallel longitudinal spins and a measurement of parity nonconservation with incident polarized protons and antiprotons at 200 GeV/c, Phys. Rev. D **55**, 1159 (1997).

[38] G. Nardulli and G. Preparata, Parity violation and strong interactions: Spin asymmetries in high energy nucleon-nucleon scattering, Physics Letters B **117**, 445 (1982).

[39] G. Nardulli, E. Scrimieri, and J. Soffer, Parity violations in pp and $\bar{p}$ p scattering at $P_{\rm Lab} \geq 1.5$ GeV/c, Zeitschrift für Physik C Particles and Fields **16**, 259 (1983).

[40] G. Mitchell, J. Bowman, S. Penttilä, and E. Sharapov, PARITY VIOLATION IN COMPOUND NUCLEI: EXPERIMENTAL METHODS AND RECENT RESULTS, Physics Reports **354**, 157 (2001).

[41] V. Gudkov, On CP violation in nuclear reactions, Physics Reports **212**, 77 (1992).

[42] V. Gudkov and H. M. Shimizu, Nuclear spin dependence of time reversal invariance violating effects in neutron scattering, Phys. Rev. C **97**, 065502 (2018).

[43] V. Gudkov and H. M. Shimizu, Neutron spin dynamics in polarized targets, Phys. Rev. C **102**, 015503 (2020).

[44] L. Stodolsky, Novel time-reversal tests in low-energy neutron propagation, Physics Letters B **172**, 5 (1986).

[45] T. Okudaira *et al.*, Angular distribution of γ rays from neutron-induced compound states of ^{140}La, Phys. Rev. C **97**, 034622 (2018).

[46] P. Hautle and M. Iinuma, Dynamic nuclear polarization in crystals of Nd^{3+}:$LaAlO_3$, a polarized ^{139}La target for a test of time-reversal invariance, Nuclear Instruments and Methods in Physics Research Section A: Accelerators, Spectrometers, Detectors and Associated Equipment **440**, 638 (2000).

[47] B. Gotschy, G. Denninger, H. Obloh, W. Wilkening, and J. Schneider, OVERHAUSER SHIFT AND DYNAMIC NUCLEAR POLARIZATION IN InP, Solid state communications **71**, 629 (1989).

[48] Website of JENDL-4.0, http://wwwndc.jaea.go.jp/jendl/j40/J40_J.html, Accessed: 2021-01-20.

[49] D. A. Smith *et al.*, Neutron resonance spectroscopy of ^{117}Sn from 1 eV to 1.5 keV, Phys. Rev. C **59**, 2836 (1999).

[50] S. F. Mughabghab, *Atlas of Neutron Resonances 5th edition* (Elsevier Science, 2006).

[51] V. Alfimenkov *et al.*, Left-right asymmetry in the γ emission at a P-parity-breaking neutron resonance of ^{117}Sn, JETP Letters **39**, 416 (1984).

[52] V. P. Alfimenkov, Y. D. Mareev, L. B. Pikelner, A. S. Khrykin, and E. I. Sharapov, Correlations in Gamma-Quanta Angular Distribution at Neutron Capture in ^{117}Sn p-Resonance Region, in *JINR Rapid Communications No. 10-85*, 1985.

[53] Website of J-PARC, https://j-parc.jp/, Accessed: 2021-01-20.

[54] Website of MLF, http://mlfuser.cross-tokai.jp/ja/blmap.html, Accessed: 2021-01-20.

[55] Website of J-PARC, https://j-parc.jp/researcher/MatLife/ja/instrumentation/index.html, Accessed: 2021-01-20.

[56] K. Kino *et al.*, Measurement of energy spectra and spatial distributions of neutron beams provided by the ANNRI beamline for capture cross-section measurements at the J-PARC/MLF, Nuclear Instruments and Methods in Physics Research Section A: Accelerators, Spectrometers, Detectors and Associated Equipment **626-627**, 58 (2011).

[57] S. Ikeda and J. M. Carpenter, Wide-energy-range, high-resolution measurements of neutron pulse shapes of polyethylene moderators, Nuclear Instruments and Methods in Physics Research Section A: Accelerators, Spectrometers, Detectors and Associated Equipment **239**, 536 (1985).

[58] I. Cole and C. Windsor, The lineshapes in pulsed neutron powder diffraction, Nuclear Instruments and Methods **171**, 107 (1980).

[59] M. Moxon, T. Ware, and C. Dean, REFIT-2009 A Least-Square Fitting Program for Resonance Analysis of Neutron Transmission, Capture, Fission and Scattering Data Users' Guide for REFIT-2009-10 (UKNSFP243, 2010) (2010).

[60] H. Stone *et al.*, Remote determination of sample temperature by neutron resonance spectroscopy, Nuclear Instruments and Methods in Physics Research Section A: Accelerators, Spectrometers, Detectors and Associated Equipment **547**, 601 (2005).

[61] H. J. Stone *et al.*, Temperature measurement in a Paris-Edinburgh cell by neutron resonance spectroscopy, Journal of Applied Physics **98**, 064905 (2005), https://doi.org/10.1063/1.2060934.

[62] K. Kino *et al.*, Energy resolution of pulsed neutron beam provided by the ANNRI beamline at the J-PARC/MLF, Nuclear Instruments and Methods in Physics Research Section A: Accelerators, Spectrometers, Detectors and Associated Equipment **736**, 66 (2014).

[63] Website of Geant4, https://geant4.web.cern.ch/geant4/, Accessed: 2021-01-20.

[64] S. Takada *et al.*, Characterization of germanium detectors for the measurement of the angular distribution of prompt γ-rays at the ANNRI in the MLF of the J-PARC, Journal of Instrumentation **13**, P02018 (2018).

[65] Website of CAEN, https://www.caen.it/, Accessed: 2021-01-20.

[66] *User Manual UM5960 CoMPASS Multiparametric DAQ Software for Physics Applications*.

[67] Website of IAEA, https://www-nds.iaea.org/pgaa/pgaa7/index.html, Accessed: 2021-01-20.

[68] H. A. Bethe and G. Placzek, Resonance Effects in Nuclear Processes, Phys. Rev. **51**, 450 (1937).

[69] W. E. Lamb, Capture of Neutrons by Atoms in a Crystal, Phys. Rev. **55**, 190 (1939).

[70] H. A. Bethe, Nuclear Physics B. Nuclear Dynamics, Theoretical, Rev. Mod. Phys. **9**, 69 (1937).

[71] F. H. Fröhner, *Evaluation and Analysis of Nuclear Resonance Data* (NEA/OECD, 2000), JEFF Report 18.

[72] B. Graner, Y. Chen, E. G. Lindahl, and B. R. Heckel, Reduced Limit on the Permanent Electric Dipole Moment of ^{199}Hg, Phys. Rev. Lett. **116**, 161601 (2016).

[73] **NPDGamma Collaboration**, D. Blyth *et al.*, First Observation of P-odd γ Asymmetry in Polarized Neutron Capture on Hydrogen, Phys. Rev. Lett. **121**, 242002 (2018).

[74] Z. Salhi *et al.*, in-situ ^{3}He SEOP polarizer for Thermal neutrons, Journal of Physics: Conference Series **1316**, 012009 (2019).

[75] T. Yamamoto *et al.*, Transverse asymmetry of γ rays from neutron-induced compound states of ^{140}La, Phys. Rev. C **101**, 064624 (2020).

[76] Website of NIST, https://www.ncnr.nist.gov/resources/n-lengths/, Accessed: 2021-01-20.